INTERFACIAL EFFECTS ON THE CHIRAL DOMAIN WALLS IN ULTRATHIN PT/CO/ALO$_X$ HETEROSTRUCTURE FOR THE FUTURISTIC SPINTRONICS DEVICES

By

BABU RAM SANKHI

Bachelor of Science
Tribhuvan University
Kathmandu, Nepal
2007

Master of Science
Tribhuvan University
Kathmandu, Nepal
2011

Master of Science
Oklahoma State University
Stillwater, OK
2022

Submitted to the Faculty of the
Graduate College of the
Oklahoma State University
in partial fulfillment of
the requirements for
the Degree of
DOCTOR OF PHILOSOPHY
May 2023

INTERFACIAL EFFECTS ON THE CHIRAL DOMAIN WALLS IN ULTRATHIN PT/CO/ALO_X HETEROSTRUCTURES FOR THE FUTURISTIC SPINTRONICS DEVICES

Dissertation Approved:

Dr. Derek Meyers

Dissertation Adviser

Dr. Emrah Turgut

Dr. Mario Borunda

Dr. Ritesh Sachan

ACKNOWLEDGEMENTS

I am deeply grateful to my Ph.D. Advisors Dr. Derek Meyers and Dr. Emrah Tugut, for their unwavering support, guidance and inspiration throughout my Ph.D. degree. Without their invaluable advice and assistance, I would not be the independent and curious researcher I am today. I would like to thank my graduate committee members, Dr. Mario Borunda and Dr. Ritesh Sachan for generously giving their important time and providing insightful suggestions and valuable feedback on my research project.

Special thanks go to Mr. Soumya Mandal for the TEM images and Dr. Elena Echeveria and Dr. Dave Mcllory for conducting the XPS measurement on our magnetic thin films. Similarly, I am grateful to Dr. Justin Shaw and Dr. Nembach Hans from the National Institute of Standards and Technology (NIST) for their immense effort in providing the BLS measurement results of our PMA magnetic heterostructure. Lastly, I want to acknowledge my research group members, Muhammet Annaorazov, Ujjal Lamichhane and Nikita Kundu for their advice and help with the experimental setup and measurements.

Finally, I am grateful for my family's continuous support, love and encouragement, including my wife Sangita, son Sambodh, and daughter Shreeja who kept me motivated to achieve this important accomplishment. Also, I am indebted to my parents Krishna, and Madhu, for their warm blessings and altruistic dedication to bolstering my higher education in my country which opened the door to this opportunity. Lastly, I would like to thank my brothers, father-in-law and mother-in-law, other relatives, and friends for their kind love and support.

Name: BABU RAM SANKHI

Date of Degree: May, 2023

Title of Study: INTERFACIAL EFFECTS ON THE CHIRAL DOMAIN WALLS IN ULTRATHIN PT/CO/ALO$_X$ HETEROSTRUCTURES FOR THE FUTURISTIC SPINTRONICS DEVICES

Major Field: PHYSICS

Abstract: Heavy metal /ferromagnet/metal oxide heterostructures are important due to their immense prospects for establishing spin textures such as chiral domain walls which are the basic ingredient of low power and capacious next-generation spintronics devices. The in-depth study of several spin interactions and magnetic parameters within those material systems is essential for the realization of such textures in the material stack. For that purpose, as detailed in this thesis, we constructed a cost-effective and sensitive vibration sample magnetometer (VSM) for magnetization measurement and explored crucial magnetic interactions that are important for future spintronics devices. Our work mainly concentrates on exploring the interfacial effects on the Dzyaloshinskii-Moria interaction (DMI), depinning fields, and other magnetic parameters for efficient DW motion in thin films made of Pt/Co/AlO$_x$ trilayers.

In the first part of this thesis, we develop a low-cost magnetization characterization instrument using a sound card and compared its sensitivity with a commercial lock-in amplifier. Secondly, we report the dependence of the domain wall depinning field, domain wall velocity including anisotropy direction, and magnetic properties on the oxidized aluminum thickness of perpendicularly magnetized asymmetric Pt/Co/AlO$_x$ trilayers. The low-temperature magneto-transport measurement technique is also adopted to investigate the amount of oxygen at the Co/AlO$_x$ interface. It is found that the tendency of variation of cobalt oxidation at the interface is also consistent with the modification of the depinning fields, coercive fields and surface roughness measured at room temperature. At the end, we adopt the methodology to study the impact of cobalt oxidation at the Co/AlO$_x$ interface in Pt/Co/AlO$_x$ trilayer structures on the DMI by varying the post-growth annealing time, Al thickness and substrate. To quantify DMI magneto-optical imaging of the asymmetric domain wall expansion, hysteresis loop shift, and spin-wave spectroscopy techniques are employed. We further correlated the Co oxidation with low-temperature Hall effect measurements and X-ray photoelectron spectroscopy. Our results emphasize the importance of full characterization of the magnetic films that could be used for MRAM technologies when subjected to the semiconductor temperature processing conditions, as the magnetic interactions are critical for device performance and can be highly sensitive to oxidation and other effects.

TABLE OF CONTENTS

Chapter Page

LIST OF FIGURES

Figure Page

Figure Page

Figure Page

CHAPTER I

GENERAL INTRODUCTION AND MOTIVATION

In this contemporary world, mushrooming technological applications such as computers and other electronic devices appeal for better performance, high storage capacity and efficiency as well. Over the last 6 decades, the semiconductor industry has manufactured powerful chips that are available in tiny sizes and at a competitive price to serve current needs. However, decrement in device sizes is approaching the atomic size limit and Moore's law comes to termination. Reduction in the feature sizes of electronic devices also results in several detrimental impacts. For example, the semiconducting transistor shows a lot of heating and quantum effects when its feature size goes below 10 nm which depreciates its working efficiency[1]. In addition to Moore's, there are other multiple other routes to improve microelectronic device performances. Such inventions incorporate the discovery of tunneling magnetoresistance (TMR) by Michel Julliere[2] in 1975 and giant magnetoresistance (GMR) by Peter Grunberg [3,4] and Albert Fert[5], who received the noble prize for uncovering this important concept in 1988[6,7]. GMR established the correspondence between resistance alteration and switching of magnetization orientation from a parallel (low resistance) to an antiparallel (high resistance) state on two magnetic layers in a stack design (figure 1). These critical breakthroughs in magnetic material systems unlocked the door for a new area of research i.e spin-electronics, in which the spin degree of freedom is comprised along with the charge in microelectronic devices for the enrichment of their performances [6,8,9].

The realm of Spintronics has numerous superiorities over the traditional silicon-based semiconductor industry. Unlike charge, which requires an external agent for its movement, spin flipping does not necessitate any auxiliary means so it holds the extensive potential for nonvolatile, low power data storing devices compared to the existing volatile memory systems and brings improved alternatives for logic devices[9,10]. Hence, spintronics can delve into a broad range of capabilities to suffice the demand for highly efficient microelectronic devices for the public welfare in near future.

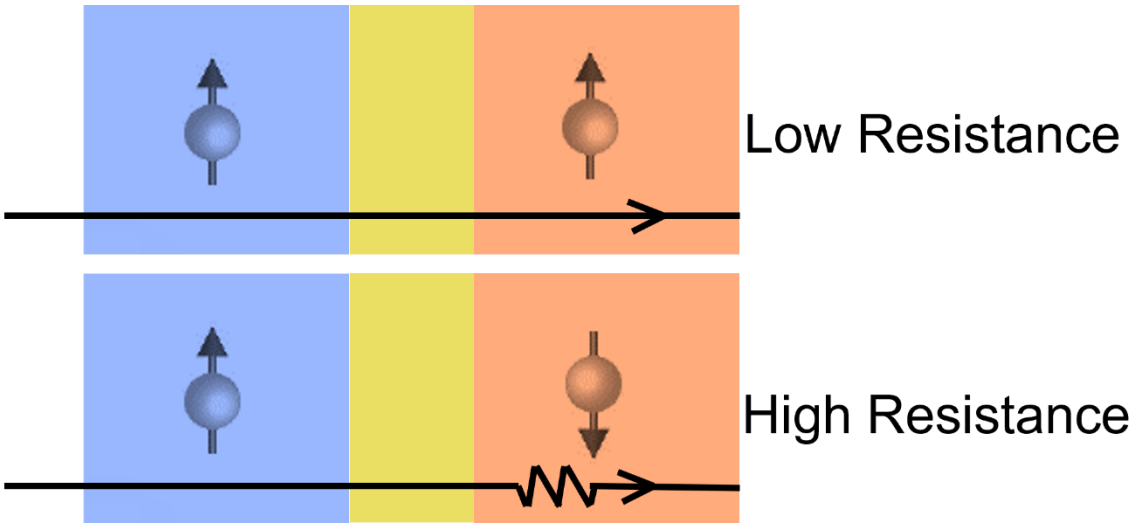

Figure 1.1. Schematic of GMR effect [11].

Magnetic random-access memories (MRAM) and racetrack memories are prospective energy-efficient spintronics devices for low-power future data storage applications in the field of spintronics. The working mechanism of MRAM is based on the magnetic tunnel junction (MTJ)[12], which is the basic component of its architecture and incorporates a thin insulating layer sandwiched between reference and free magnetic layers as shown in figure 1.2 (a). The MRAM stores data in the form of memory bits 1(0) based on the tunneling magnetoresistance (TMR) values (high or low) during the current flows through the MTJ. The TMR is determined by the direction of spin alignment on the magnetic layers. It's maximum and minimum values can be obtained when the magnetization in both (the reference and free layer) are parallel and antiparallel respectively.

MRAM uses two distinct approaches for the transfer of angular momentum during the read and write processes. In spin transfer torque (STT)- MRAM, for example, angular momentum is transferred from the reference magnetic layer to the free magnetic layer with the auxiliary STT and both reading and writing current use the same path (figure 1.2 (a)). On the contrary, in spin-orbit torque (SOT) MRAM, the writing and reading channels are different (Figure 1.2(b)) and a high spin-orbit coupling heavy metal layer acts as a source of SOT for the angular momentum transfer. This makes the SOT MRAMs fast switching and highly durable compared to STT-MRAMs[7].

Another distinct class of memory systems are racetrack memories, which were proposed by Parkin et. al in 2008 and a schematic is shown in figure 1.2 (c). It encodes the data using current-driven domain walls (DWs) in the magnetic nanowires[13,14]. The DWs motion determines the writing and reading speed of the racetrack memory system. DWs can be driven by using several external means, such as extrinsic magnetic field, STT, current-generated spin Hall effect (SHE), electric field, spin waves, polarized light[15], and thermal gradient[11,15–19]. However, the current-induced SHE can only be applied for the Néel DWs and the Néel DWs move much quicker than the Bloch type in the presence of the equivalent applied field in perpendicular magnetic anisotropy (PMA) ferromagnetic thin film system[17]. Hence, auxiliary SOT originating due to SHE plays an important role in magnetization switching in MRAM and in the dynamics of chiral DWs for racetrack memories, which are crucial components of future spintronics devices.

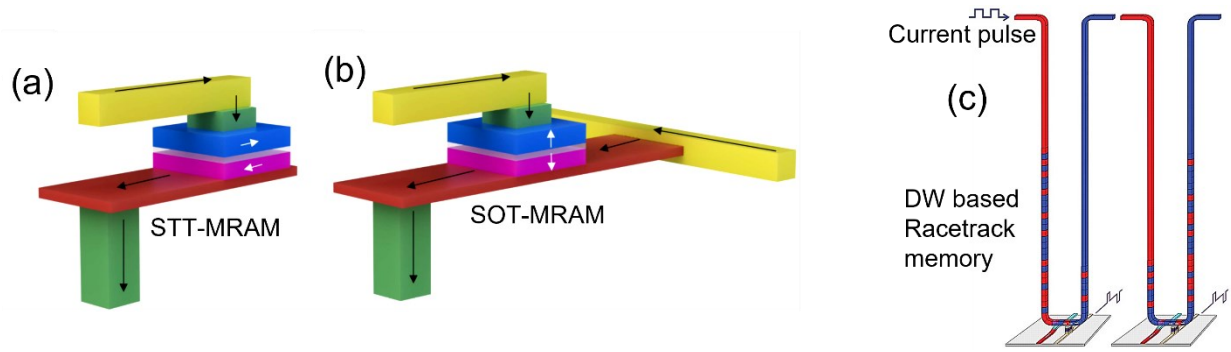

Figure 1.2. Schematic of (a) STT based (b) SOT-based magnetic random access memories (c) Domain wall-based racetrack memory [7,13].

In figure 1.2 (a) the pink and blue layers are free and reference layers respectively separated by the white (insulating layer). The white arrows represent the direction of magnetizations and the black arrows represent the current direction. Figures are adapted from refs. [7] and [13].

Many studies have shown that structurally asymmetric ferromagnets i.e. HM/FM/ MO_x multilayers have a strong potential for holding such chiral DWs and are also important for producing current enhanced SOT for magnetization switching. The heterostructures, such as Ta/CoFeB/MgO and Pt/Co/ AlO_x stacks, show strong PMA and large curie temperature[11,20–23] which makes them an appealing candidate for future spin-electronics devices. Several former efforts have explored their immense possibility of the development of high-capacity and low-power storage devices [11,13,14,20–23]. Despite those great endeavors on that material system, the systematic study of interfacial impacts on the basic intrinsic phenomena occurring within them such as saturation magnetization, Dzyaloshinskii Moria interaction (DMI), magnetic anisotropies and depinning fields are not complete yet. This thesis demonstrates the experimental study on perpendicularly magnetized magnetic heterostructures to investigate the role of interfacial effects on those crucial phenomena for the exploration of magnetization switching and the dynamics of the chiral domain wall [24].

This thesis work is organized as follows: The second chapter introduces some of the crucial magnetic interactions, distinct magnetic anisotropies, and chiral domain walls and the importance of the study

of current and field-driven DW dynamics. The procedure of sample fabrication, and the principle and methods of a few major characterization techniques are discussed in chapter three. The fourth chapter incorporates our experimental work for the designation and development of a magnetic characterization tool, i.e. an audiocard-based low-cost vibration sample magnetometer. Similarly, the fifth chapter explains the interfacial and surface effects in Pt/Co/AlO_x trilayers systems on the DW dynamics, depinning fields and other magnetic properties. Moreover, detailed experimental work to delve into the influence of its interfacial oxidation on DMI by engineering Pt/Co/AlO_x is presented in chapter six. Chapter 7 of the thesis summarizes all of our experimental findings and lists some of the potential future works that can be proceeded based on our experiments.

CHAPTER II

BACKGROUND

2.1 Fundamental magnetic interactions

This section focuses on the role of spin orbit (SO) interaction in magnetic materials along with other basic magnetic interactions existing in ferromagnetic materials that are helpful to comprehend the different interface effects explored in this thesis work.

2.1.1 Spin orbit interaction

Spin orbit (SO) interaction, also called spin-orbit coupling (SOC), describes the relativistic interplay between particle's intrinsic spin angular momentum (**S**) and its orbital angular momentum (**L**). The basic magnetic moment associated with the electronic spin is constant and called the Bohr magnetron ($\boldsymbol{\mu_B}$), which is given by the relation[1,25]:

$$\boldsymbol{\mu_B} = g\frac{-e}{2\,m}\,\boldsymbol{S}, \tag{2.1}$$

where g=2, e, m are the g-factor, charge, and mass of an electron respectively. **S**= $\frac{\hbar}{2}$ [25] is the quantized spin angular momentum of an electron, $\hbar$ is the reduced planks constant. The coupling of these intrinsic magnetic moments with the orbital angular momentum of the electron gives rise to the effective magnetic field that results in interesting physical phenomena in the material world.

The magnitude of SOC is predominately determined by the strength of **L-S** coupling and the atomic number of the corresponding element. The Hamiltonian energy H_{so} associated with SOC is given by the following expression [25,26]:

$$H_{SO}=\lambda(\mathbf{S}\cdot\mathbf{L}) \tag{2.2}$$

where $\lambda\propto Z^4$ gives the strength of spin orbit interaction, Z is the atomic number. It shows heavy metal elements are more preferrable for the enhancement of SOC. This coupling is trivial to get a detailed understanding of magnetic anisotropy direction, DMI and domain walls depinning fields in magnetic thin films. This thesis emphasizes the study of those crucial phenomena in our Pt/Co/AlO_x heterostructures.

2.1.2 Exchange interaction

The Heisenberg exchange interaction is the symmetric interaction existing between two neighboring spins in magnetic materials, which is given by the Hamiltonian equation as expressed [1]:

$$H_{ex} = -\sum_{i\neq j} J_{ij}(\boldsymbol{S}_i \times \boldsymbol{S}_j) \tag{2.3}$$

Where J_{ij} is the Heisenberg exchange constant which measures the interaction strength between neighboring i^{th} spin ($\mathbf{S_i}$) and j^{th} spin ($\mathbf{S_j}$).

In 3d transition metals (for example, Fe, Mn, Co, etc.), the distribution of conduction electrons is not localized, and atomic orbitals overlap following the Pauli exclusion principle which influences the exchange interaction. For the relatively large interatomic distances, J_{ij} is the positive and parallel alignment of adjacent spins is energetically preferred which gives rise to the ferromagnetic state of some magnetic materials. However, the shorter interatomic distances

favors minimal energy for the antiparallel configurations of spins and J_{ij} becomes negative leaving the material in an antiferromagnetic state [1,27].

2.1.3 Dzyaloshinskii-Moria interaction

Contrary to the Heisenberg exchange interaction as discussed above, which favors (anti)parallel alignment of neighboring spins, the Dzyaloshinskii-Moria interaction (DMI) favors the spins to align perpendicular to each other to minimize the energy of the system. More specifically, DMI is an antisymmetric interaction and the mathematical equation for the Hamiltonian energy due to DMI is expressed below[1,7,28]:

$$H_{DMI} = -\sum_{i \neq j} \boldsymbol{D}_{ij}.(\boldsymbol{S}_i \times \boldsymbol{S}_j) \tag{2.4}$$

Where $\mathbf{D}_{ij}=D(\mathbf{r}_{ij}\times\mathbf{z})$ represents the D-Moria vector[29]. $\mathbf{r}_{ij}$ is the displacement vector of separation between two adjacent spins and $\mathbf{z}$ is the unit vector perpendicular to the film plane. D is the D-moria constant, which is determined by the intrinsic properties of the material.

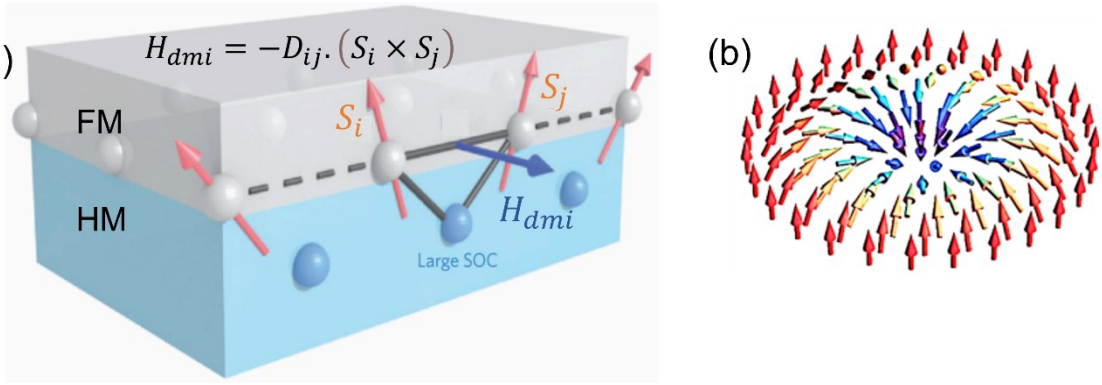

Figure 2.1. (a) Schematic of the thin film of heavy metal (HM)/ferromagnetic (FM) system inducing the DMI at their interface adapted from Ref.[30] (b)Neel-type skyrmion [31]

Primarily, the DMI originates due to spin orbit coupling, as mentioned in an earlier discussion so the magnetic material systems heavy metal layers enhance the DMI value. However, it is important to note that DMI strength is relatively weak (by the order of 10 mT for the Pt-based and

100 mT for Ta-based heterostructures) compared to that of the symmetric exchange interaction[17]. Another important circumstance that boosts the DMI is broken inversion symmetry. The non-centrosymmetric crystal structures are responsible for increasing the bulk DMI in crystals[32]. The interfacial DMI, on the other hand, appears from the structural inversion symmetry breaking at the interfaces as shown in figure 2.1(a). Refs.[33–37] have made strong efforts to boost up the DMI by the symmetry breaking at the interfaces and by inserting heavy metals, such as Pt and Ta, as a strong source of SOC. Engineering of such heterostructures for manipulating DMI is critical for the stabilization of exquisite magnetic spin textures such as chiral domain walls, vortices and skyrmions (figure 2.1 (b)), which are the essential ingredients for the next generation high capacity spintronics applications.

2.1.4 Zeeman interaction

Zeeman interaction involves the interplay between the external magnetic field and the magnetization of magnetic materials. The energy of Zeeman interaction can be explained by the following equation [26]:

$$E_{zeeman} = - \mathbf{M} \cdot \mathbf{H_{ext}} \quad (2.5)$$

Where M is the net magnetization and H_{ext} is the external magnetization field. It indicates that H_{ext} prefers to align magnetic moments along its direction to minimize the total energy of the system.

2.2 Magnetic anisotropies in magnetic material

Magnetic anisotropy is the preferred direction of magnetization for the specific magnetic material [38]. It is determined by the nature of crystallinity, the magnetic sample's shape and the interfaces of magnetic thin films. Also, the magnetic interactions which are explained in section 2.1 are responsible for the origin of different kinds of magnetic anisotropy. Some of the basic

anisotropies which are helpful to understand magnetic characteristics presented in our work are listed below.

2.2.1 Magneto crystalline anisotropy

Magnetic materials tend to have a different proclivity of magnetization along a different directions. The amount of energy difference required to magnetize the material along the hard and easy crystallographic axes gives the magnitude of anisotropy energy. Easy and hard axes of magnetization are defined based on the strength of the external magnetic field required to magnetize the material along specific crystallographic axes. The direction along which relatively less external field is sufficient to reach the saturation magnetization is referred to as the easy axis. More energy is needed to align all the magnetic moments along hard axis direction. For example, crystallographic directions [100] and [111] are the hard and easy axis respectively for the base-centered cubic structure of Fe [7]. The amount of energy required to rotate the magnetization direction from [100] to [111] is the quantitative measurement of magneto crystalline anisotropy. It also provides the estimation of locking strength between crystal lattices and spin due to SO coupling[26]. For the uniaxial system, the anisotropy energy can be expressed as following[1,26]:

$$E_K = \sum_n K_n \, sin^{2n}\theta \qquad (2.6)$$

K_n are the anisotropy constants and θ represents the angle between the easy axis and magnetization direction.

2.2.2 Interfacial anisotropy

In contrast to magnetocrystalline anisotropy which arises due to the crystal structure, interfacial anisotropy is the result of structural asymmetry at the interface. For the ultrathin magnetic films, the anisotropy constant of equation 2.6 can be expressed as[1,26]:

$$K = \frac{2K_i}{\mathrm{t}} + K_v \qquad (2.7)$$

where K_i is the interfacial anisotropy and K_v is the volume anisotropy constants. When the film thickness is extremely thin, interfacial anisotropy dominates giving rise to anisotropy along the direction perpendicular to the film plane termed perpendicular magnetic anisotropy (PMA). However, for a relatively thicker film, the volume anisotropy governs the magnetic anisotropy along the film's surface called in-plane anisotropy. The easy axis of magnetization depends on the magnetic material's thickness in a multilayer system. The film is easily magnetized along the direction normal to the film plane up to a certain critical thickness but is switched to the in-plane direction on further increasing the magnetic material's thickness as observed in many magnetic multilayer systems comprising ferromagnetic cobalt [1,39,40].

In most of our Pt/Co/AlO_x ultrathin films, because of the polycrystalline structure of cobalt, they do not show any net magnetocrystalline anisotropy. However, PMA is observed as an interfacial effect of extremely thin films. Both bottom Pt-Co and top Co-AlO_x interfaces are responsible for promoting the PMA of our trilayers. Regarding the bottom interface, the hybridization of d orbitals of Pt and Co makes the OOP magnetic moment dominant over an in-plane component. Similarly, the oxidation of cobalt at the top interface augments the PMA contribution as it decreases the d orbital states energy yielding the OOP magnetic moment[7].

2.2.3 Shape anisotropy

The magnetization direction depends on the physical shape of the material system which is called shape anisotropy. The origin of such anisotropy is mainly due to the interaction between neighboring dipoles. In a magnetic system, dipoles behave as point charges so that there exist either attractive or repulsive forces between dipoles. The dipolar interactions are long-range interactions that affect the magnetization energy of material systems [1]. Due to this, the easy axis

of magnetization lies along the long axis of the asymmetric shape of the material system. For the given anisotropy constant K_s, the anisotropy energy E_s can be generalized from eq. 2.5 as[1]:

$$E_s = K_s \sin^2 \theta \tag{2.8}$$

Where θ is the angle between the magnetization direction and the easy axis of magnetization.

2.2.4 Effective anisotropy

The effective anisotropy is the net anisotropy coming from all static anisotropies (shape, dipolar and interfacial). The total effective anisotropy energy E_T comprising those anisotropies can be expressed as[1,7]:

$$E_T = K_{eff} sin^{2n} \theta - \mathrm{M} H_{ext} \cos \theta \tag{2.9}$$

The latter term comes from Zeeman interaction as an effect of demagnetization energy due to the application of external fields. θ is the angle between the magnetization direction and the easy axis. K_{eff} is the effective anisotropy constant and is directly related to the anisotropy field H_k by the relation[41]:

$$K_{eff} = \frac{\mu_o H_k M_s}{2} \tag{2.10}$$

Where H_k is the minimum external applied field required to align the magnetic moments along the hard axis. M_S is the saturation magnetization. This equation is widely used in this experimental work to explain the complicated behaviors of chiral DWs existing in our magnetic multilayer system.

2.3 Magnetic domain walls

Domain walls (DWs) are the boundaries between neighboring domains where the magnetic dipoles change their orientation abruptly. Magnetic moments always prefer to align along the

easy axis due to magnetic anisotropy energy. At the same time, however, the demagnetization energy is very high for this alignment state. Both energies tend to be as low as possible to exist in the form of energetically more favorable configurations. When the total equilibrium energy is minimized, the magnetic material stays in a multidomain state creating a boundary between them termed DW which facilitates the spin orientation from one direction to the next. There are different types of DWs structures under study. For example, vortex, antivortex and transverse type DWs were investigated in permalloy nanowires[42]. In this subsection, primarily the importance of DWs i.e. Bloch and Néel DWs on PMA ferromagnetic ultrathin films will be discussed in detail. Finally, the basics of the field and current induced DW dynamics incorporating the importance of DMI and depinning fields on their motion will be elucidated in brief.

2.3.1 Bloch and Néel domain walls

In magnetic thin films with PMA, DW can exist either in Bloch or Néel forms depending on the physical nature of the material system. Their difference comes from how the spin transition takes place from one domain to the next. In Bloch-type DW, the spins rotate in such a way that they are perpendicular to the plane of the sample lying along the DWs as shown in figure 2.2 (a). However, In Néel-type DWs, the intermediate spins rotate in the plane and align perpendicular to the DWs as displayed in the figure.2.2 (b). In figure 2.2, the magnetizations of domains on the left and right side of domain wall's are pointing into and out of the plane respectively. The z-axis is normal to the sample surface[11].

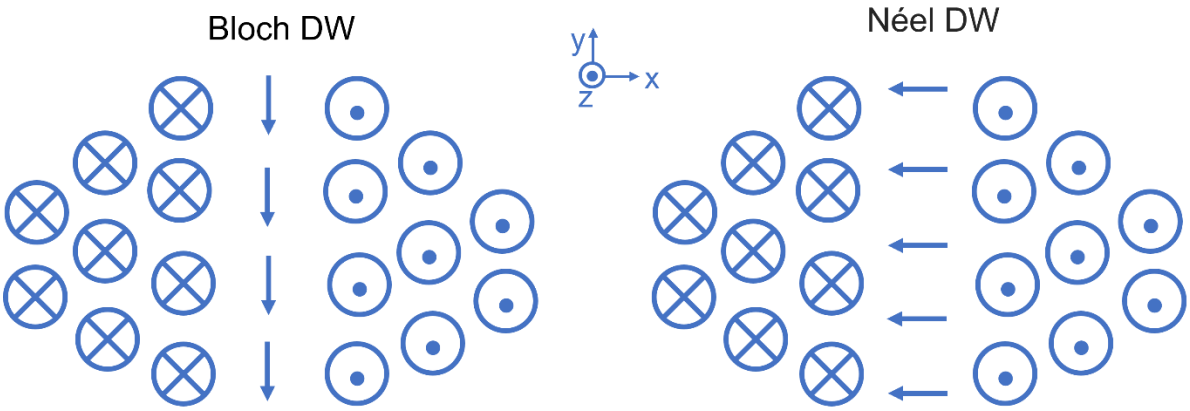

Figure 2.2 Schematic of the top view of Néel and Bloch DWs in the PMA sample [11].

During the formation of Néel and Bloch DWs, the spins tend to be disordered and rotate away from their easy axis of magnetization which costs both exchange interaction and anisotropy energy respectively. The equilibrium state of those energies determines the DW width. The relation of DW width Δ with the exchange constant A and effective anisotropy K_{eff} is given by the equation[43]:

$$\Delta = \left(\frac{A}{K_{eff}}\right)^{1/2} \tag{2.11}$$

This equation shows that a weak K_{eff} and a strong A increase the width of DWs and vice versa.

In a magnetic thin film system, Bloch DWs are preferred in the absence of DMI. However, for ultrathin films where DMI is dominant Néel DWs are more favorable than Bloch walls. For instance, in $[Co/Ni]_i/Pt$ and $[Co/Ni]_i/Ir$ multilayer, both types of DWs are present depending on the repetition number i of Co/Ni bilayer[44]. For the specific values of i, Ni/Pt and Ni/Ir interface are responsible for the formation of right-handed and left-handed Néel DWs respectively. Moreover, in $Pt/Co/AlO_x$ trilayers system, left-handed Néel DWs can be formed[45–47]. This chirality (left-handedness or right-handedness) of magnetic DWs is determined by the DMI,

though the DW width remains constant for the specific A and K_{eff} [7,48,49]. The DMI-induced chiral DW energy is given by the relation[1,50,51]:

$$\sigma(H_x) = \sigma_0 + 2K_D\ \Lambda - \Pi\Lambda M_s\mu_0|H_x + H_{DMI}| \tag{2.12}$$

Where σ_0 is Bloch-type domain wall energy density and $K_D = N\ \mu_0 M_s^2/2$ is the anisotropy constant [51,52]. N is the demagnetizing factor that depends on the thickness of the ferromagnetic thin film and domain wall width. H_x and H_{DMI} are the applied inplane field and DMI-induced field respectively. Domain wall energy is determined by the polarity and magnitude of both DMI and inplane field which ultimately influences the domain wall velocity. This approach will be used extensively for the quantification of DMI in our magnetic thin films by using polar MOKE.

2.3.2 Field-driven domain wall motion

For the perfect film, which has no imperfections and thermal variations, the DW motion can be explained in two separate regimes: steady-state and processional regimes as shown in figure 2.3(a). For the particular region where the field is less than it's definite value, walker breakdown field H_w, the velocity-field plot is linear in the steady region. However, the velocity drops just after H_w as the damping torque is not sufficient to balance the torque due to the applied field (i.e Zeeman torque) before it resumes its linearity[7,53,54] in the precession region.

In the practical PMA magnetic films, in addition to the applied OOP applied magnetic field Hz, both atomic defects and thermal effects also influence the DW movement so that the velocity curve is nonlinear for the lower fields (figure 2.3 (b)). The domain wall study for such films can be sorted into 3 separate regions: creep, depinning and flow[55]. In the creep regime, the velocity of DW is slow and depends exponentially on the OOP field H_z [1,56–58]. The depinning regime starts at a critical value of H_z at which DWs motions exceed the interactions due to defects and become independent of any disorder in the films. The depinning field in (figure 2.3 (b)) at

absolute zero is greater than that at T > 0 K as the thermal activation energy assists in initiating DW motion at finite temperatures. The velocity in this regime is driven by the difference between the instantaneous Hz and depinning field i.e $(H_z - H_{dep})^{\delta}$ [57]where $^{\delta}$ is the power corresponding to the depinning field . Lastly, in the flow regime the H_z is much greater than depinning field and dominates all the intrinsic properties of the films. The velocity in this region has a linear relation with the H_z called the walker breakdown field [55].

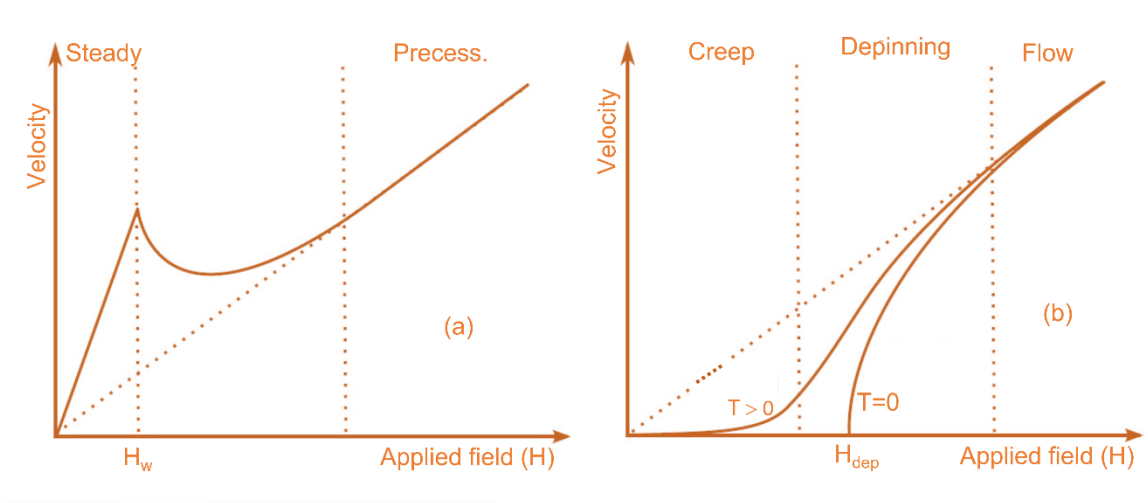

Figure 2.3. The dependence DW on the external magnetic field applied along the easy axis of magnetization for (a) the perfect films and (b) the films with defects at absolute zero and nonzero temperatures[7,55].

The steady and precessional region in figure 2.3 (a) is partitioned by the Walker field (H_w). In figure 2.3 (b) at zero temperature, there are only two regions (depinning and flow) and H_{dep} is the minimum field required to drive the domain walls. However, at finite temperatures, domain wall motion is observable in the creep region in addition to the depinning and flow regimes. These figures are adapted from Refs [7,55].

2.3.3 Domain wall motion in the creep regime

The velocity of domain walls in the creep regime is defined by the exponential relation [1,57,58]:

$$v = v_0 \exp(\alpha {H_z}^{-1/4}), \tag{2.13}$$

Where v_0 is the fitting parameter and α is the material parameter. For instance, the exponential rise of DW velocity in the creep regime for Pt/Co/AlO_x samples for different thicknesses of AlO_x is illustrated in figure 2.4. The study and analysis of DW motion in the creep regime are paramount to characterizing DMI and depinning fields in our perpendicularly magnetized thin films where the chiral behaviors of magnetic bubbles are dominant [1].

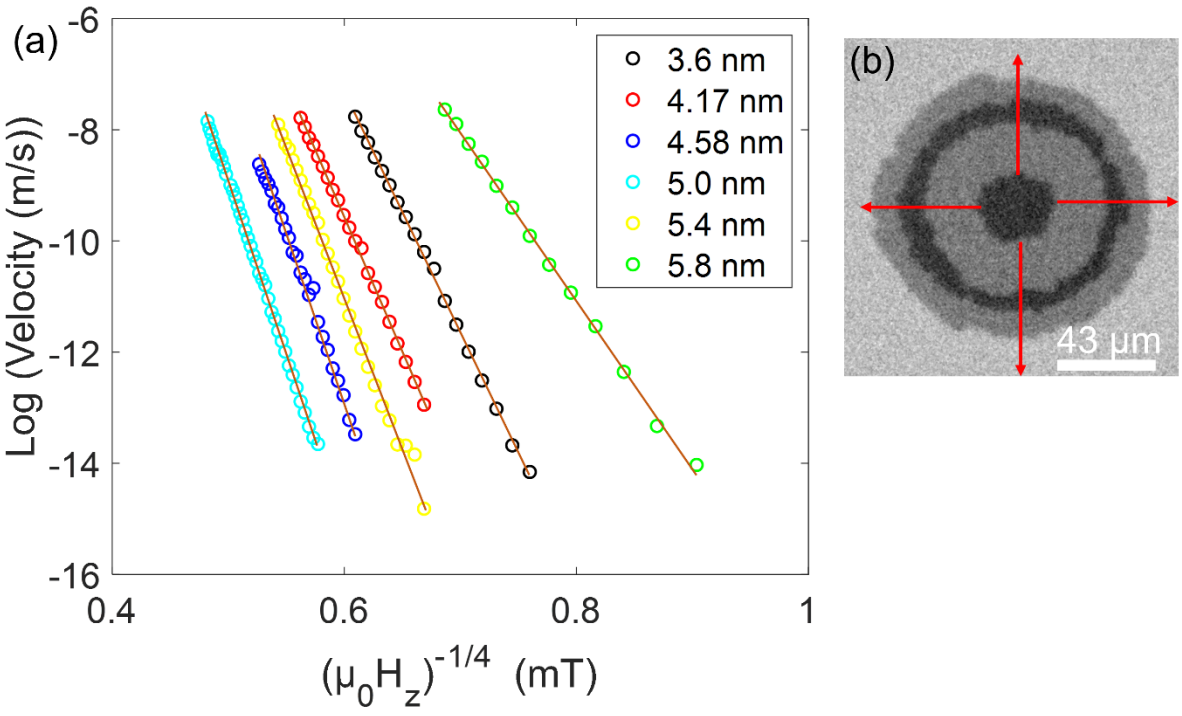

Figure 2.4. (a)Domain wall velocities as a function of out-of-plane (easy axis) magnetic fields for the ultrathin magnetic film Pt (4 nm)/Co 1.1 nm)/AlO_x (t) with different AlO_x thickness (t). (b) Kerr image of the symmetrically expanded magnetic domain wall.

In the creep regime, the magnetic bubble expands symmetrically in all directions in absence of an inplane field H_x (figure 2.5(a)). In contrast, when we apply H_x, it acts parallel to one side magnetic bubbles and antiparallel to another side, creating an anisotropic energy for the domain walls (figure 2.5(b)). As explained in the domain wall energy equation 2.11, chiral domain walls

(DW) depend on the H_x+H_{DMI} factor [50,59]. When both H_x and H_{DMI} are equal in magnitude but in the opposite direction, the DW energy is at a maximum, resulting in the minimum velocity of DWs. However, if both Hx and H_{DMI} are equal in magnitude and acting in the same direction, the energy is at a minimum, yielding the lowest value of DW velocity. Hence, the asymmetric behavior of magnetic bubbles is more pronounced when the H_{DMI} is combined with H_x[1]. Our experiment used the point of the minimum velocity of asymmetric DW velocity vs H_x curve for the estimation of magnitude and direction DMI caused magnetic field as explained in chapter 5 in detail.

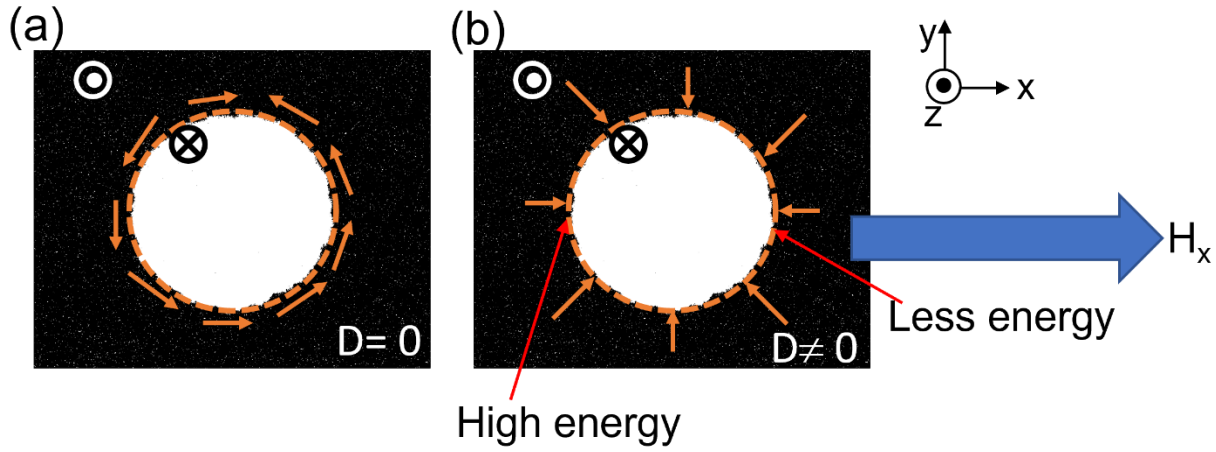

Figure 2.5 Domain walls with (a) DMI constant=0 and (b) DMI constant≠0 [1].

The blue arrow in figure 2.5 (b) represents the direction of the inplane plane field (H_x). Under the application of H_x along the positive x direction, the spins on its left are parallel to H_x and the spin on the right is opposite to that of an applied field. This makes less energy on the right side compared to the left side of chiral domain walls leading to the asymmetric expansion of magnetic bubbles where the growth of the right side takes place much faster than the left[1].

2.3.4 Current generated spin-orbit torque-induced domain wall motion

In heavy metal /ferromagnet heterostructures, the spin hall effect (SHE) [60,61]and the Rashba effect[21] are the two essential phenomena for the enhancement of spin-orbit torque (SOT) [17]. The SHE arises due to the charge current-induced spin-dependent scattering of electrons on the two opposite sides of heavy metal. However, the Rashba effect is solely an interfacial effect, which happens due to the structural non-symmetry at the interface. Recently, the SOT mechanism is extensively applied to realize the systematic switching of magnetization [20,22,62,63] and to accomplish the ultrafast DWs motion [40,45,64] for the data storage applications in the field of high density, low power spintronics[17].

In the PMA magnetic heterostructure, when the charge current I_c flows through the heavy metal, the electrons having mutually obverse spin orientation accumulate into the metal's two opposite edges[61,65], which engenders the transverse spin current I_s due to SHE as shown in figure 2.6. The piled-up spins are injected at the interface and absorbed by the adjacent ferromagnetic layer which produces the torque on the magnetization in the direction of spin polarization called Slonczewski-like torque. This torque engenders the effective field, with the component along the OOP direction which influences the switching field of magnetization and drives the chiral DWs if the component of magnetization is aligned with the current direction[17] as illustrated in figure 2.6. In our work, the approach of SOT-assisted DW movement, which causes the hysteresis loop shift in presence of H_x, is substantial for the manipulation of DMI in chapter 5.

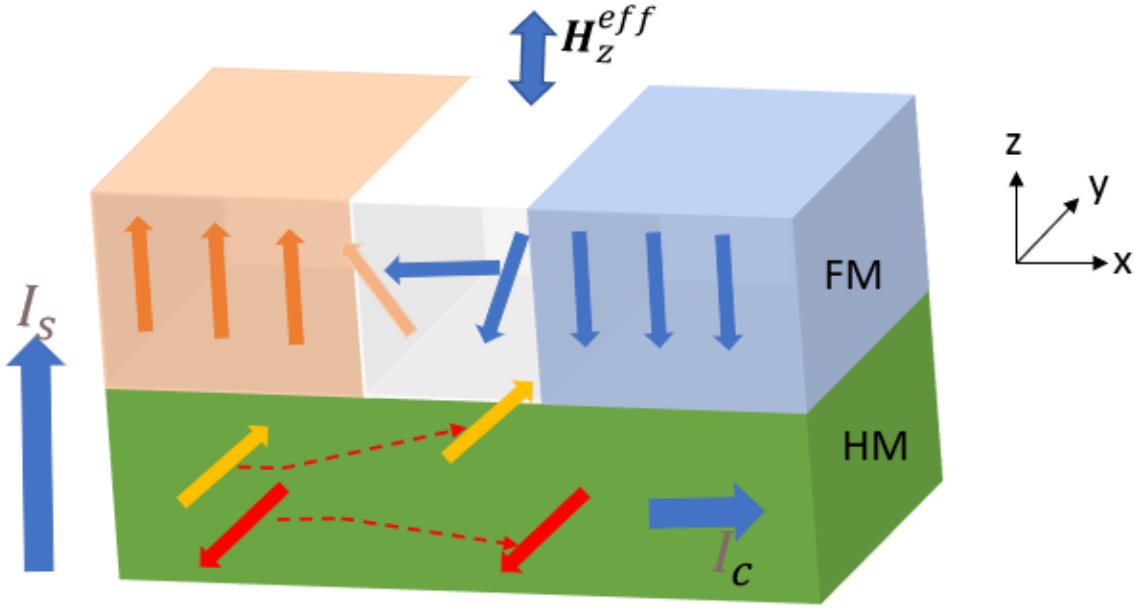

Figure 2.6 Schematic for the spin Hall effect and the effective field along the z-direction H_z^{eff} on chiral (Néel type) domain walls**.**

CHAPTER III

SAMPLE PREPARATION AND THE MAJOR TECHNIQUES OF CHARACTERIZATION

3.1 Magnetron sputtering system

Magnetic thin films are prepared by using a magnetron sputtering system which is based on the physical vapor deposition (PVD) technique. Figure 3.1 shows the AJA magnetron sputtering system used for the growth of magnetic heterostructure. This system comprises two main parts: a load lock and main chamber. The main chamber can accommodate a total of 5 guns. To begin, the sample is placed in the load lock and pumped down to less than 10^{-6} Torr. Then, it is transferred to the main chamber via using a magnetic transfer arm. The base pressure of the main chamber is always maintained at less than 10^{-8} Torr.

During the thin film growth procedure, the main chamber is filled with inert (argon) gas. The cathode (target) is connected to a high negative potential and emits free electrons. Those high-speed free electrons collide with the argon gas atoms. The atoms are ionized to form Ar^{+} plasma at very low pressure at around 2 mTorr in the main chamber. The ionized argon Ar^{+}impacts the target atoms that are directed towards the substrate placed on the sample holder where they ultimately adhere to form a standard thin film. The complete mechanism inside the main chamber is displayed in figure 3.1 (b). Two different power sources are used for different types of material's growth; a direct current (DC) source is for the conductive material however radio frequency (RF) power source is suitable for the insulating/metal oxide target. In a magnetron sputtering system, auxiliary magnets are used beneath the target which makes argon ion yield

highly efficient as it increases the distance traveled by the electron due to Lorentz force. This leads to the overall growth procedure possible even at very low pressure (~ 2 mTorr) and also prevents the collision between ejected target atoms allowing improvement of thin film quality. Those qualities make the magnetron sputtering superior to other sputtering techniques.

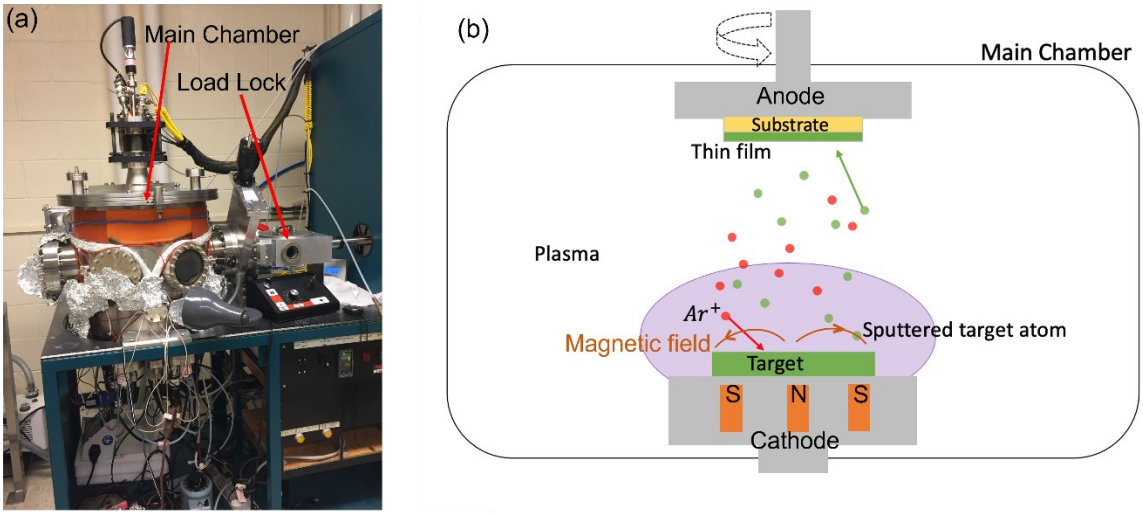

Figure 3.1. (a) Photography of the magnetron (DC/RF) sputtering system (b) Mechanism of thin film deposition inside the main chamber.

3.2 Patterning of samples

The samples were patterned in the form of Hall bar devices by using the photolithography procedure for electrical measurement purposes as presented in the figure. 3.2. First, we spin-coated KL5310 positive photoresist on the top of samples (figure.3.2 (a)) with the speed of 3000 rpm and baked it for 1 minute at 100 ^{o}C shown in figure 3.2 (b). Next, UV light of 30-watt power was exposed (figure.3.2 (c)) for 2 minutes 30 seconds passing through a glass mask that was partly covered with metals for the partial transmission of light into the photoresist. After exposure, the structure of the resist changes in such a way that the unexposed part become resistant to a developer and the exposed part dissolves when it is immersed in TMAH 0.26N

developer for about 40 seconds (figure.3.2 (d)). The film area without resist was etched by ion (Ar^+) sputtering/milling (figure 3.2 (e)), which was achieved in a high vacuum chamber maintained at 25mtorr Argon pressure and 45-watt RF power. In the end, the resist is etched out by using acetone (figure.3.2 (g)) and a Hall bar device was prepared in (figure.3.2 (h))[7].

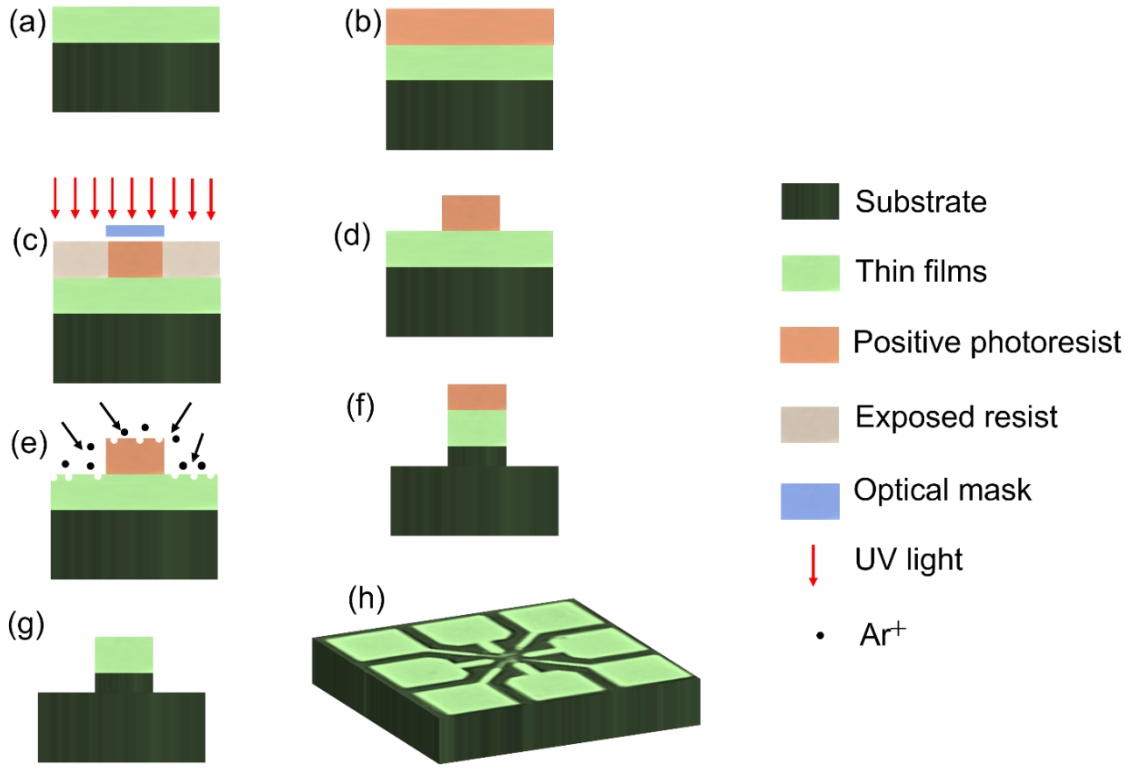

Figure 3.2 (a)-(h) Schematic of all the steps of photolithography fabrication process[7].

3.3 Vibration sample magnetometry

A vibration sample magnetometer (VSM) is a very sensitive instrument to measure the magnetization of a sample. The commercial VSM can measure the magnetic moment with a sensitivity order of 10^{-8} emu. It's main components comprise an electromagnet, pick-up coils, and a holder to attach the sample at its end that is connected to the motor capable of vibrating it at a particular frequency. VSM works on the principle of electromagnetic induction and our experiment uses a custom-built VSM for the magnetic characterization of the samples. By

vibrating the magnetized sample, the flux linked with the pickup coils changes and induces the voltage on the coils. This induced voltage is directly proportional to the magnetic moment (m), amplitude (A) and frequency (f) of the vibration of the sample i.e. V= KmAf, where K is the multiplication factor which is quantified based on the geometry of the coil and the configuration of the experimental set up. The induced voltage in the form of an AC signal is extracted using lock in (LI) amplifier and is compared it with a reference signal from LI to withdraw the information about the magnetization of the sample (figure 4.4) [11]. The schematic of our custom-built VSM is shown in figure 4.4 which is sensitive enough to measure the magnetic moment of our thin films. Both theoretical and experimental details for the quantification of magnetic moment can be found in chapter 4.

3.4 Magneto-optical Kerr effect and MOKE microscopy

Magneto-optical Kerr effect (MOKE) which was discovered by John Kerr in 1877 [38], explains the changes in polarization, phase, and amplitude of light radiation when it illuminates a magnetized object. It can be studied in three distinct modes: polar, transverse, and longitudinal modes as displayed in figure 3.3 (a). In polar mode, the direction of magnetization is parallel to the plane of incidence and perpendicular to the sample surface. Similarly, the transverse configuration corresponds to magnetization parallel to the sample surface and perpendicular to the direction of the incidence plane. For the longitudinal configuration, the magnetization acts parallel to the plane of incidence and the sample surface. In the polar configuration, the effects are easier to observe for our sample compared to the other two modes as the easy axis of magnetization for the ultrathin PMA samples lies along the direction of normal to the sample surface. This makes the polar configuration the most suitable method to visualize the DW motion in our films[11].

MOKE microscopy is a special technique that is used to visualize magnetic domain structure in magnetic materials. A study of DW dynamics using a Kerr microscope is an efficient way to extract important information regarding antisymmetric exchange interaction (DMI) in ultrathin films without damaging the sample. Figure 3.3 (b) is a picture of P-MOKE in our lab which is outfitted with horizontal and vertical electromagnets to generate the out-of-plane (OOP) and in-plane (IP) magnetic fields up to around 350 mT. It comprises a convex lens, polarizer, beam splitter, and analyzer as its internal parts. The light rays from the source are converged by the convex lens, then they go to the beam splitter and pass through the objective with a resolution of the order of 5 microns. This light illuminates the sample surface and reflects it to the analyzer as sketched in figure 3.4. The polarization plane of such reflected light is shifted by a certain amplitude called the Kerr amplitude (A_k). The total amplitude of the reflected light beam can be expressed as [1]; $A_{tot}=A_o+A_k$, where A_o is the optical reflection amplitude and A_k represents the Kerr amplitude. The ratio of A_k and A_o i.e $\Phi_k = A_k/A_o$ measures the total Kerr angle (Φ_k) [1]. During the experiment, the analyzer and polarizer are adjusted for the enhancement of reflected light amplitude. More particularly, the analyzer is set to align along the direction of Kerr rotation to enhance intensity contrast reflected from two oppositely oriented magnetic domains (figure 3.4). The contrast of the light intensities gives information about the different configurations of magnetic domain walls in the magnetic sample placed in the sample holder as shown in figure 3.3 (c).

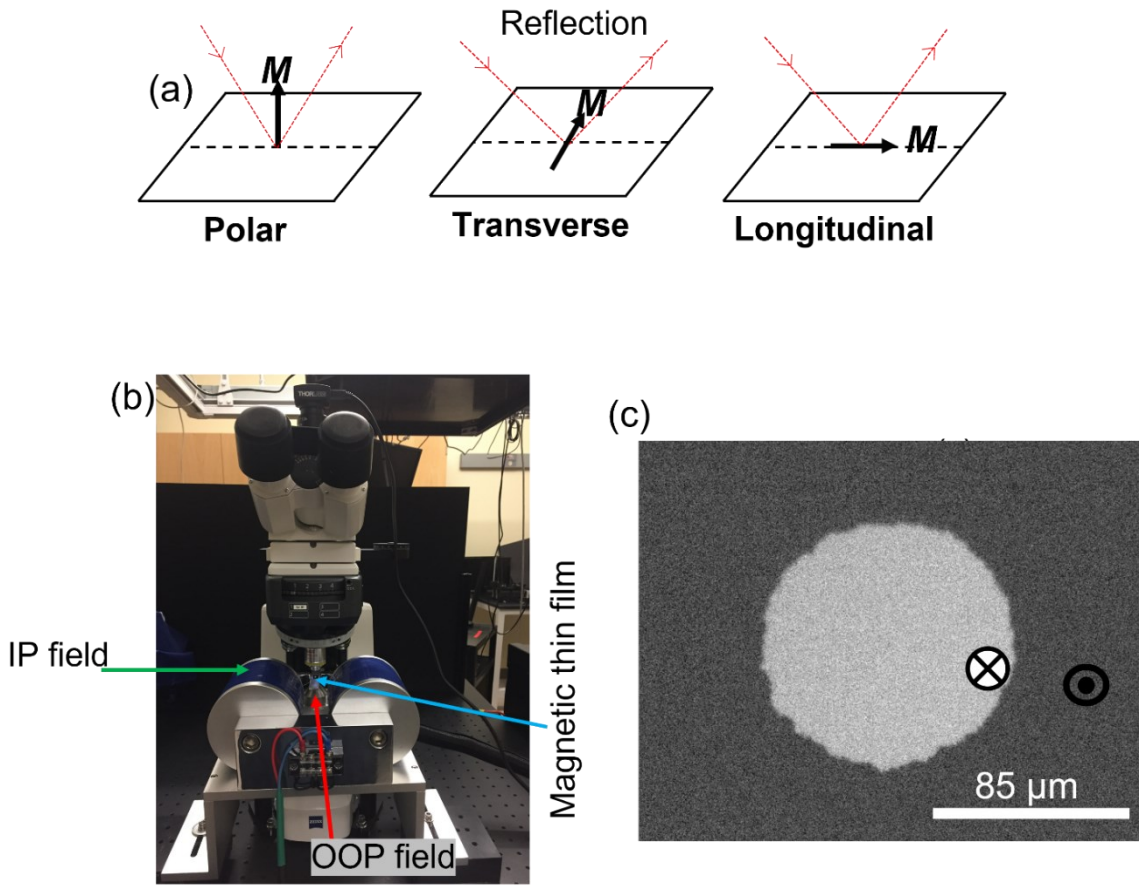

Figure 3.3. (a) Schematic of different modes of Kerr effect [38] (b) Photography of polar Kerr microscope configured with the electromagnets (c) A picture of magnetic contrast in presence of out of and in-plane magnetic field.

In figure 3.3 (a) Green and red arrows show in-plane and out-of-plane magnetic fields and the light blue arrow points to magnetic thin films placed on the smallholder.

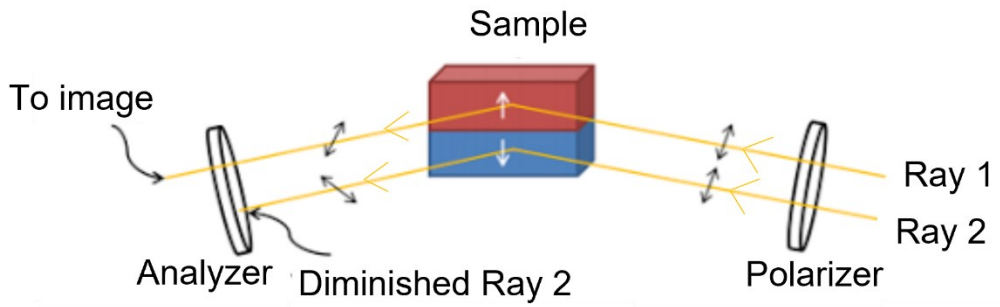

Figure 3.4 Schematic illustrating the operational mechanism of MOKE microscopy adapted from reference [1].

CHAPTER IV

A LOW-COST VIBRATING SAMPLE MAGNETOMETRY BASED ON AUDIO COMPONENTS

4.1 Introduction

Measurement of magnetization is an important characterization step for magnetic materials in the field of condensed matter physics to understand their fundamental properties and to utilize them in industrial applications [66]. To quantitatively define the magnetic state of the mater, the induction from the total magnetic moment is usually measured as a function of an external magnetic field, which is known as a magnetic hysteresis measurement [67]. In this method, a hysteresis measurement can provide information about magnetic properties such as retentivity, coercivity, and susceptibility, all of which play crucial roles in studies of magnetic materials [66,68–71]. The most common instruments employing the induction method are SQUID and vibrating samples or coil magnetometries. Although SQUID provides the highest sensitivity ($\sim 10^{-8}$ emu [72]) among the three, its operation is costly due to the usage of cryogenic liquids. On the other hand, vibrating samples or coil magnetometers are relatively cost-effective for magnetic hysteresis measurements, and they provide a sensitivity at the order of 10^{-7} emu [6]. Vibrating sample magnetometry (VSM) is more straightforward and sensitive compared to vibrating coil magnetometry; however, the later makes the measurements possible even at sub-Kelvin temperatures [73].

The VSM technique employs a vibrator (e.g. motor) to create a magnetic flux change around the magnetic sample, which induces an AC emf on pickup coils near the sample. This AC voltage is proportional to the magnetization of the sample, and its sensitive measurement can be performed by a dedicated circuit or a lock-in amplifier [74,75]. Although lock-in amplifiers are common in research laboratories for phase-sensitive measurement of modulated signals, they still cost around $5,000. On the other hand, commercially available sound cards can record modulating waveforms and provide an extremely high bit analog-to-digital conversion (ADC), similar noise levels to a lock-in amplifier, multiple inputs for synchronous measurements, and default computer interface [76], and these sound cards are widely available at a fifty-times lower price compared to a lock-in amplifier. These advantages make them an alternative for measurements within the frequency range of human hearing, which is between 20 Hz and 20,000 Hz frequencies. Indeed, this frequency range is suitable for many laboratory measurements, such as VSM [77].

In this chapter, we evaluated the performance of a 4-channel Behringer (Model UMC404HD) sound card with a 24-Bit ADC resolution and 192 kHz sampling rate as an alternative to a commercial lock-in amplifier (Signal Recovery 7230) with a 10-Bit ADC resolution. Although a computer directly acquired the lock-in amplifier measurements, we developed a LabView code to compute the in-phase and out-of-phase components of the measured waveform from the sound card. First, we constructed an RLC circuit and measured the frequency-dependent voltage on the resistance by both the sound card and the lock-in amplifier. This allows us to understand the internal mechanisms, limitations, and advantages of the sound card. Next, we constructed a vibrating sample magnetometer based on audio components, which makes magnetization characterization significantly economical and versatile. In our hysteresis tests, we used three distinct samples: a Nickel piece, a perm-alloy thin film with an easy-plane anisotropy, and a Co/Pt multilayer with perpendicular magnetic anisotropy. All the hysteresis curves of the samples have been successfully obtained, and the Anomalous Hall effect measurement confirms the Co/Pt

multilayer hysteresis as being the most challenging sample among three. We also varied vibration frequency to optimize the sensitivity, which is found at the order of $5.4 \times 10^{-6} emu$ at 34.7 Hz with the sound card and approximately seven times higher compared to the sensitivity of the lock-in amplifier.

This chapter is as organized as follows: The second section describes the RLC circuit and the LabView code for the phase-sensitive detection with the sound card. The third section details the VSM design, the theoretical calculation of the VSM sensitivity, and the hysteresis characterization of three samples. The fourth section summarizes our findings.

4.2 RLC circuit

An RLC circuit is a common method to evaluate a frequency response of a phase-sensitive measurement by analyzing the amplitude and the phase of an AC voltage from the components. One RLC circuit was already used to evaluate the frequency response of a sound card by comparing a commercial lock-in amplifier [78]. This characterization is a crucial step before using sound cards for scientific purposes, because each sound card may have a different filtering and frequency-dependent amplification, which determination for calibration purposes. In our RLC circuit, we connected the circuit components in series and attached the measurement units, as in figure 4.1. We employed the oscillator output of the lock-in amplifier as an AC voltage source for the circuit. We also connected this output to the Channel 2 input of the sound card to demodulate the signal, which is similar to the reference input in the lock-in amplifier. The voltage dropped across the resistor is first measured by the lock-in amplifier and then by the sound card, both of which are analyzed by a computer. We avoided simultaneous measurements by two instruments to prevent any cross-talk. Below we give a background about the phase-sensitive measurement of the modulated signal, which will be helpful to elaborate our home-made lock-in software in Labview software.

The voltage on the resistor R (V_R), can be written as [78];

$$V_R = V_0 R \left(R^2 + \left(2\pi f L - \frac{1}{2\pi f C}\right)^2\right)^{-1}, \tag{4.1}$$

where V_0, f, L, and C are the amplitude and frequency of the sinusoidal input, inductance, and capacitance of circuit elements, respectively. The resonance frequency is simply $f_0 = \{2\pi(LC)^{1/2}\}^{-1}$. The phase difference between the input signal and V_R is

$$\delta = Arctan\left[\left(2\pi f L - \frac{1}{2\pi f C}\right) R^{-1}\right]. \tag{4.2}$$

In a phase-sensitive detection, a signal $V_s = A_s \sin(2\pi f t + \delta)$ is mixed with both in-phase reference $\sin(2\pi f t)$ and out-of-phase reference $\cos(2\pi f t)$ signals. After mixing, the resulting voltages would be $X = \frac{A_s}{2}\cos\delta + AC$ for the in-phase reference and $Y = \frac{A_s}{2}\sin\delta + AC$ for the out-of-phase reference. By using a low-pass filter, we filter the AC components and only retain the DC components of X and Y signals, which can be directly read from our lock-in amplifier. Then, the amplitude and the phase on R are calculated by $A_s = |X + i\,Y|$ and δ =Angle$[X + i\,Y]$, where Angle is a function to find the angle of the complex number.

While commercial lock-in amplifiers can straightforwardly provide X and Y components of the signal, we implemented additional data processing after we acquire the signal V_s and the reference using the sound card. Fortunately, these processes are relatively fast and straightforward by today's personal computers and widely available software.

In figure 4.2, we show the block diagram of the phase-sensitive detection process, which is implemented by LabView software. The signal and the reference waveforms are measured by Channel 1 and Channel 2 inputs of the sound card, respectively, at 24-Bit ADC and 192 kHz sampling rate. Because the reference signal is strong enough (0.1 Volt), the first part of the code

called VI-1 accurately calculates the frequency, amplitude, and phase of the reference signal. To find the out-of-phase reference, we apply a 90-degree phase shift to the reference in the second part of the code called VI-2 using the sampling info from VI-1. Next, we mix the input signal with both in-phase and out-of-phase reference signals resulting in the two outputs, i.e. X and Y. By using Butterworth low-pass filter to reject the AC component, we finally obtain the DC components of X and Y. This filter function also uses the vibration frequency obtained from the VI-1 and valid high and low-frequency cut-offs [79].

In our RLC experiment, we first measure X and Y components with the lock-in amplifier and then repeat the measurement with the sound card by varying the frequency of the input signal between 5 Hz and 50 kHz. The circuit elements used in the circuit are resistance (R), inductance (L), and capacitance (C) with the values of 5.0 Ω, 116.8 mH, and 1.0 μF, respectively. The measured frequency-dependent amplitudes and phases from the sound card and lock-in amplifier are plotted in figures 3(a) and 3(b), respectively. Figure 4.3(a) shows a perfect agreement between the sound card and lock-in for the amplitude of the signal. However, in figure 4.3 (b) the sound card shows small discrepancies for the phases below 20 Hz and above 3 kHz frequencies. Our theoretical calculations obtained by Eq. 4.1 and Eq. 4.2 and shown by the black curves in Fig. 3 mostly agree with the experimental findings, yet the quality factor is different due to the non-ideal inductance and capacitance in the circuit.

Notably, the sound card shows a limitation for low frequencies, e.g. below 20 Hz. This originates from high-pass filters used in most of the sound cards due to human hearing being limited to below 20 Hz. Our sound card still can measure the amplitude correctly, but the phase has an approximately 10% error below 15 Hz. Secondly, other abnormalities at the high frequencies in figure 43(b) originate from the digitalization of the signal and the reference and relative delay between them, which becomes significant at high frequencies after 2 kHz. By using an RLC circuit, we conclude that the sound card has comparable specifications between 20 Hz and 2 kHz

and measurements below 20 Hz and above 2 kHz frequencies require additional precaution. Next, we implement our sound card as a magnetometry measurement instrument to characterize three specific magnetic materials.

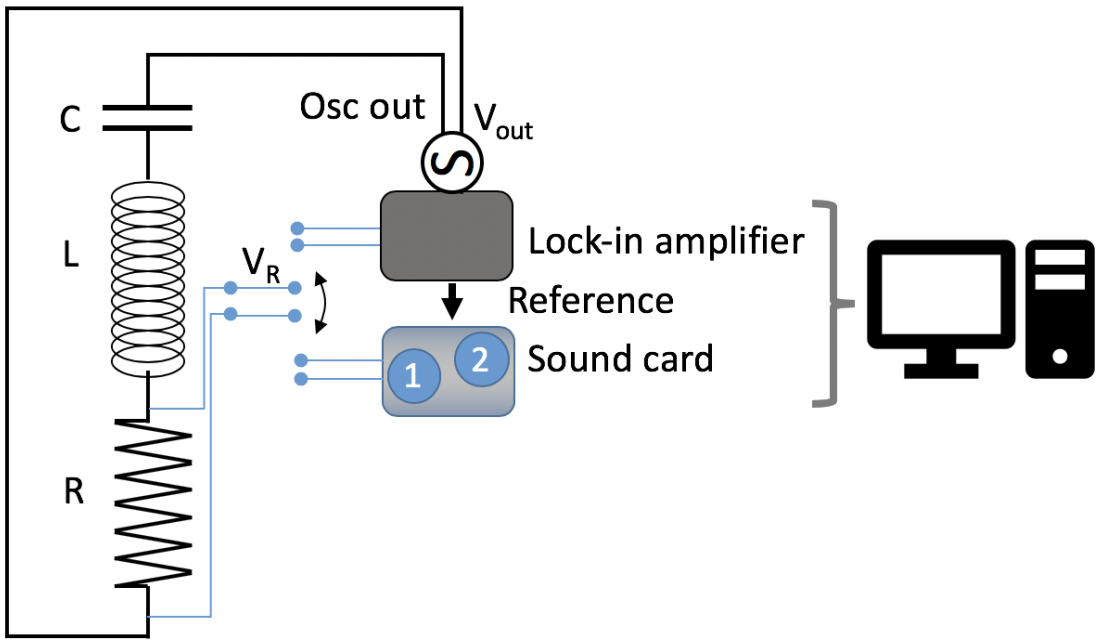

Figure 4.1. Schematic of the RLC-circuit and connections with the lock-in amplifier and the sound card.

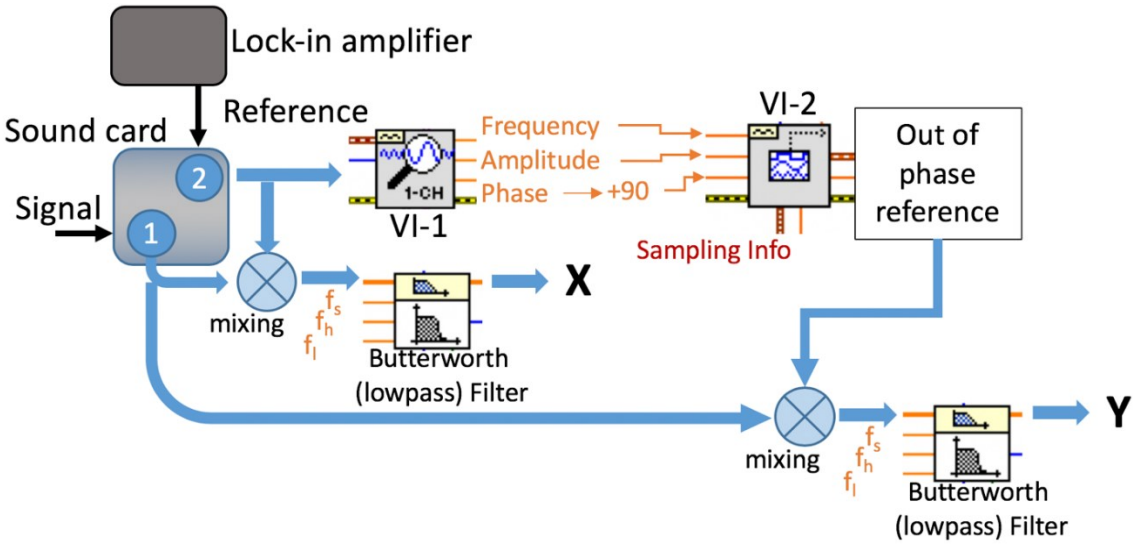

Figure 4.2. Diagram of the LabView code for the detection of phase-sensitive signals with the sound card.

In figure 4.2, the sound card acquires the signal (V_R) from the resistor and the reference from the lock-in amplifier. Next, VI-1 calculates the frequency, amplitude, and phase of the reference, and VI-2 produces the out-of-phase reference. These two in-phase and out-of-phase references are mixed with the signal and we apply a Butterworth filtering to find the DC components, which are referred to as X and Y signals.

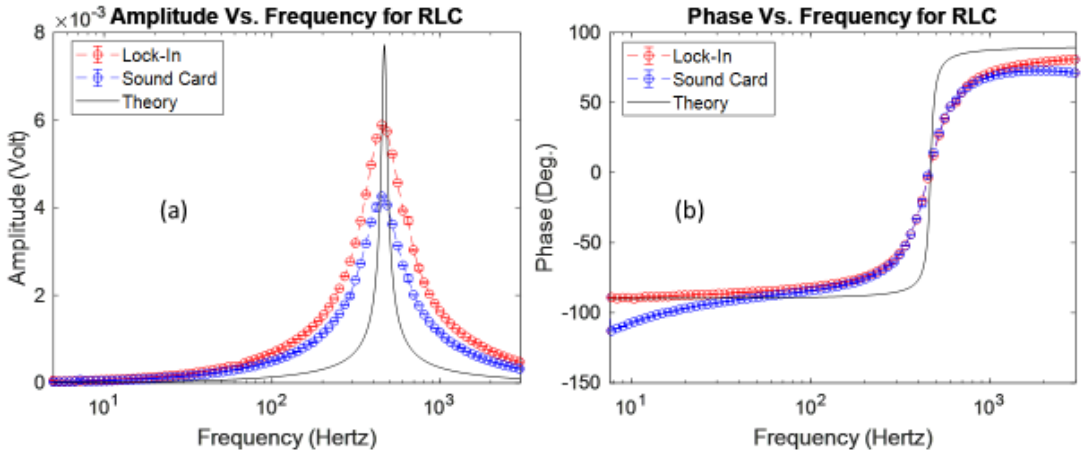

Figure 4.3. The potential on the resistor as a function of frequency (a) amplitude and b) phase with respect to the input reference.

In this figure, the blue circles (o) and red circles (o) correspond to the soundcard and the lock-in amplifier measurements, respectively. The black line is the theoretical calculation by assuming ideal circuit components.

4.3 Vibrating sample magnetometer

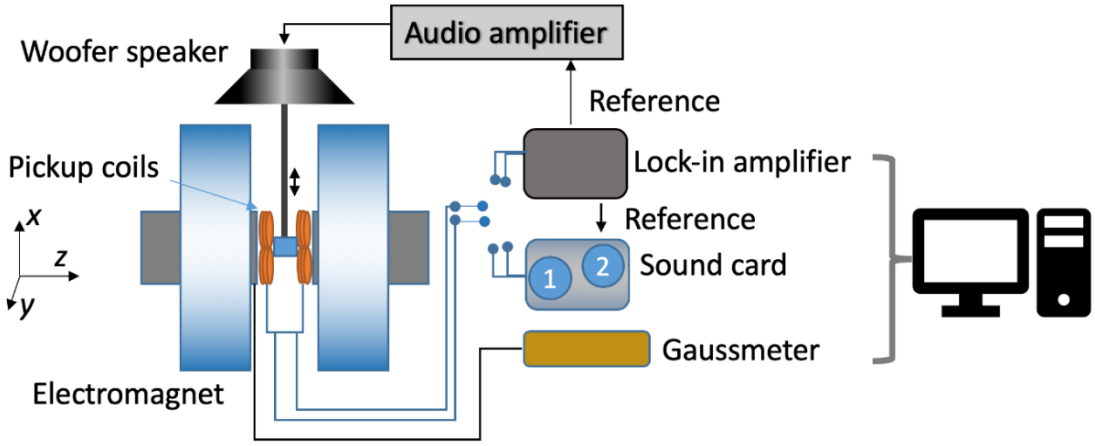

Figure 4.4. Schematic of homemade vibrating sample magnetometer.

In this figure, four pickup coils are located between the pole pieces of an electromagnet. The sound card and the lock-in amplifier are connected to the VSM turn by turn. A Laud woofer speaker and audio amplifier are used to vibrate magnetic samples.

In our VSM design (figure 4.4), we use a woofer speaker and an audio amplifier as the vibrator, exploiting the availability of commercial audio components. The speaker oscillates the sample and creates sinusoidal magnetic induction, which is then picked up by the pick-up coils. For the pick-up coils, choosing the most sensitive coil configuration is a tedious task, and there is already a significant amount of literature on this topic. Mallison et al. used a 4-coil configuration based on the reciprocity theorem [80], which employs a symmetric arrangement for simplicity. Besides,

Bernards [81] had studied 8-coil and 12-coil configurations and stated the superiority of the later one as the output signals were primarily affected by the image charges in the 8 coil configuration [81,82]. For complicated arrangements of the coils, Zieba et. al. presented an approximate solution of sensitivity function by using spherical harmonic expansion [83]. In addition to previous works, there are recent studies to improve sensitivity and the data acquisition and processing in the VSM technique as being an important characterization instrument [84–88].

In our VSM, we used the 4-coil configuration as Mallison et al. described [80] to have a high sensitivity while keeping the setup compact and simple. The axes of the coils are parallel to the applied magnetic field with an electromagnet, which is along the *z*-axis. Even though this configuration allows us to measure the magnetization in only one direction, using more coils and sensing magnetization in multiple directions is left as a future study. As illustrated in figure 4.4, along the *z*-axis, the electromagnet creates a uniform magnetic field that is recorded by a Gaussmeter, and the sample is vibrated along the *x*-axis. As the magnetic field is swept between two saturated states, serially connected pick-up coils pick up the periodic flux change. The resulting sinusoidal voltage is sensitively measured by the lock-in amplifier and the sound card turn by turn.

Next, we describe the experimental parameters, which are used to calculate the induced voltage on the pick-up coils. An individual coil has an outer radius r_2=8.93 mm, an inner radius r_1=4.22 mm, and a width of w= 8.74 mm. We use AWG 42 copper magnet wire with a diameter of D=0.07112 mm to wrap the pick-up coils. The number of turns of each coil is calculated by $n = \frac{(r_2 - r_1)w}{D^2}$ and found to be 8118. The external magnetic field acts along the *z*-direction and we take the sample as a point dipole *m*. The *z* component of the magnetic field (B_z) due to the magnetization (m) is

$$B_Z = \mu_0 m(3z^2 - x^2 - y^2 - z_0^2)\left(4\pi(x^2 + y^2 + z_0^2)^{\frac{5}{2}}\right)^{-1}, \quad (4.3)$$

where μ_0 is the magnetic permeability of a vacuum. The coils are fixed on a 3D-printed frame, which keeps z_0 constant at 13.24 mm. The coils are also 25 mm apart in the *x*-direction. The flux produced on a coil is found by $\phi_z = \iint B_Z \; dx \, dy$, where we change variables to the cylindrical coordinate of a coil by $x = x_0 + \rho sin\theta$ and $y = \rho cos\theta$. We then express the integral by $\theta = 0 \rightarrow 2\pi$ and $\rho = 0 \rightarrow r_i$ limits, where r_i is the radius of the *i*th wrap along the radius. There are approximately 66 layers $((r_2 - r_1)/D)$ along the radius and 123 layers (w/D) along the axial direction. Next, we calculate individual flux quantities and sum these 66 flux quantities and multiply by 123. This method results in a more accurate calculation of the total magnetic flux, instead of assuming all the wraps have the same magnetic flux and multiplying with the total 8118 turns.

Next, we find the induced voltage on the coil $V = \frac{d\emptyset_z}{dt} = \frac{d\emptyset_z}{dx}\frac{dx}{dt}$, where *x* is the vibration direction. The displacement of vibration at any time t is represented by $x = A \; sin \; 2\pi f t$, where *f* is the frequency and A is the amplitude. Using Mathematica, we first differentiate with respect to *x* and perform the integration. We finally find the rate of flux change $\frac{d\emptyset_z}{dx} = 36.4172 \times 10^6 \; Wb/m$ and the induced voltage,

$$V \; = 4\frac{\mu_0 \times m}{4\pi}(\; 36.4172 \; A \; 2\pi f). \tag{4.4}$$

After we theoretically calculate the induced voltage due to a magnetic moment, we test the sensitivity of our VSM by studying hysteresis curves of three distinct samples, i.e. a tiny nickel piece (99.99% pure), a perm-alloy thin film, and a Co/Pt multilayer magnetic samples. The following sections below explicate the theoretical calculations and experimental results obtained in our VSM experiment for each sample.

4.3.1 Nickel piece

In our first test, we use a nickel piece (99.99% pure) with a mass of 0.22 grams. Density and the saturation value of magnetization of Ni are given 8.90 g/cm^3 and 5.1×10^5 A/m, respectively [66]. The total magnetic moment is found by m= $M \times Volume$ = 12.75×10^{-3} Am^2. The experiment is repeated for the vibration frequencies of 17 Hz, 34 Hz, and 64.7 Hz and corresponding induced voltages are captured by both the lock-in amplifier and sound card. By using Eq. 4, we find the value of saturated induced voltages $2.38 \times 10^{-2}\ V$ (with an oscillation amplitude $A = 1.22mm$), $1.72 \times 10^{-2}\ V$ (with $A = 0.43\ mm$), and $1.92 \times 10^{-2}\ V$ (with $A = 0.26\ mm$), at 17 Hz, 34 Hz, and 64.7 Hz frequencies, respectively. These oscillation amplitudes are found from the displacements of the sample using a high speed camera.

In the experiment, the time constant and waveform acquisition time for lock-in amplifier and soundcard are maintained at 200 ms and 800 ms, respectively. We also varied the cut off frequency in the Butterworth filter for the optimum mixing of the signals from the sound card. Figures 4.5 a), b) and c) represent the measurements of induced voltages from the Ni piece as the magnetic field sweep from -0.2 T to 0.2 T at different frequencies, which are referred to as hysteresis loops. In each plot, blue and red curves represent the soundcard and lock-in amplifier, respectively. The saturation induced voltages measured by the lock-in amplifier are $2.25 \times 10^{-2}\ V$, $1.19\ \times 10^{-2}\ V$, and $2.85\ \times 10^{-2}\ V$ for the frequencies of 17 Hz, 34 Hz, and 64.7 Hz, respectively. Because the soundcard has complicated filtering and amplification, the measured values with a sound card are calibrated using the lock-in measurements. We note that our experimental results are in very good agreement with the theoretically estimated induced voltages. Moreover, the induced voltage responses measured with the soundcard are in perfect correspondence with the ones obtained with the lock-in amplifier, which illustrates the excellent performance of the soundcard for measuring modulated signals.

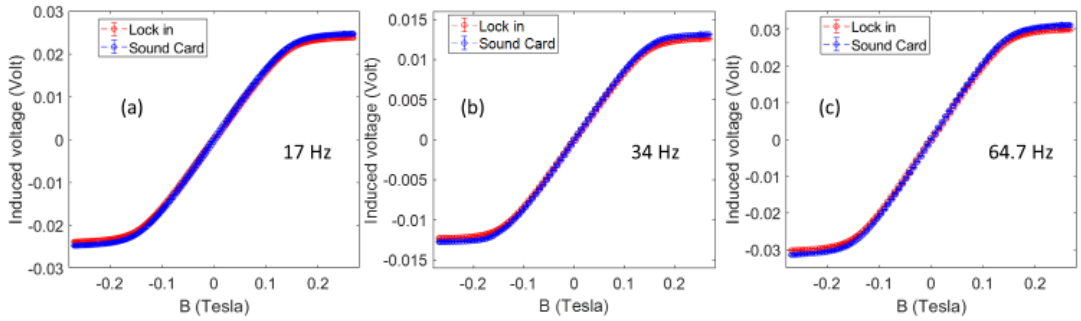

Figure 4.5. Induced voltages as a function of an applied magnetic field (B) at (a)17 Hz, (b) 34 Hz, (c) 64.7 Hz frequencies.

4.3.2 Perm-alloy thin film

As the Ni piece created a large induced signal and provided relatively easy measurements, we next perform a magnetometer on a more challenging perm-alloy thin film sample, which is deposited on a silicon substrate using the magnetron sputtering technique. The dimension of the sample is 6mm×7mm and the thickness of the perm-alloy is 50 nm, which gives a total volume of 21×10^{-13} m^3. The magnetization is measured along an easy axis, which is in-plane at this thickness of perm-alloy. Taking the saturation magnetization 800 emu/cm^3 of perm-alloy [88], we find the magnetic moment to be 1.68×10^{-6} Am^2. The calculated values of saturation induced voltages are $3.26 \times 10^{-6}\ V$ (with an oscillation amplitude $A = 2.04\ mm$), $8.29 \times 10^{-6}\ V$ (with $A = 3.17\ mm$), $1.51 \times 10^{-5}\ V$ (with $A = 2.90\ mm$), and $2.59 \times 10^{-6}\ V$ (with $A = 0.26\ mm$) for the frequencies of 10.4 Hz, 17 Hz, 34.4 Hz, and 64.7 Hz, respectively. The time constant and waveform acquisition time are fixed at 200 ms and 800 ms for the lock-in amplifier and the sound card, respectively.

The hysteresis curves of the film are presented in figure 4.6, and they have a rectangular shape with a small coercive field and an adequate in-plane magnetic anisotropy as seen in previous

perm-alloy thin films [88,89]. A linear background of the hysteresis curve is subtracted due to the diamagnetic nature of the silicon substrate [90]. In all frequencies, the measurements of the sound card have complete overlap with that of the lock-in amplifier. Furthermore, at lower frequencies, the sound card data are still smoother than that of the lock-in amplifier, even though the signal is reduced due to the filtering in the sound card, which can be taking account as a calibration factor. The values of saturation induced voltages are $2.82 \times 10^{-6}\,V$, $8.33 \times 10^{-6}\,V$, $1.47 \times 10^{-5}\,V$, and $8.18 \times 10^{-6}\ V$ at the frequencies of 10.4 Hz, 17 Hz, 34.4 Hz, and 64.7 Hz, respectively. For all the frequencies except 64.7 Hz, we have very good agreement with the calculated induced voltage. For 64.7 Hz, our measurement of vibration amplitude may have a large error.

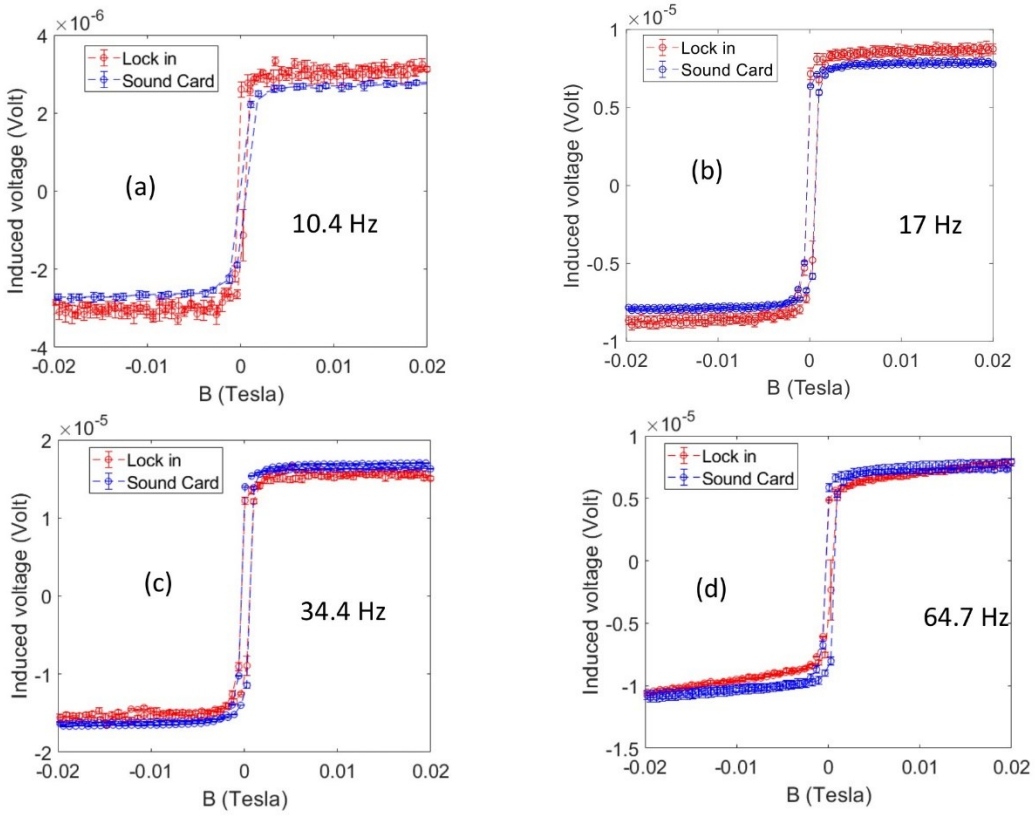

Figure 4.6. The hysteresis loops of a perm-alloy thin film with an easy plane anisotropy at (a) 10.4 Hz (b) 17 Hz, (c) 34.4 Hz and, (d) 64.7 Hz vibration frequencies.

4.3.3 Co/Pt multilayers with perpendicular magnetic anisotropy

As the last sample, we grew a magnetic multilayer with a perpendicularly aligned magnetic anisotropy. On a Si substrate, we deposited Ta(4nm)/[Co(0.4nm)/Pt(0.4nm)]$_{x3}$/Pt(3nm) multilayer using a sputtering technique. This Co/Pt multilayer has been reported to have a perpendicular magnetic anisotropy and there is great interest in such multilayer films for spintronics applications and topological spin textures [91–97]. The dimension of the sample is 6mm×8.5mm and the total thickness of the magnetic material is 1.2 nm. We use the saturation magnetization of Cobalt $1.4 \times 10^6\ A/m$ [66] [94] and find the expected magnetic moment to be $8.6 \times 10^{-8}\ Am^2$. The respective calculated induced voltages at the frequencies of 17.4 Hz and 34.7 Hz are $4.33 \times 10^{-7}\ V$ (with $A = 3.17\ mm$) and $3.30 \times 10^{-7}\ V$ (with A $= 1.2\ mm$). We increased the driving voltage on the Laud speaker for a larger displacement about 20%. From the perm-alloy hysteresis, we found these two frequency range give the highest signals, therefore, we measured only at these two frequencies for Co/Pt multilayer sample.

In the experiment, the sample is aligned perpendicular to the direction of the applied field, which makes the easy axis along the field direction. The time constant and acquisition time for the signal detection is set at 1 and 6 seconds, respectively, for the lock-in amplifier. Whereas, for the SC, the corresponding values are set at 1 and 2.8 seconds. The magnetizations observed in two distinct frequencies clearly illustrate a perpendicular magnetic anisotropy for Co/Pt multilayer. As plotted in figure 4.7, our hysteresis curves have a rectangular shape and agree with the previous measurements on similar multilayer samples [97]. We obtained saturation induced voltages of $4.14 \times 10^{-7}\ V$ and $3.28 \times 10^{-7}\ V$ for the frequencies of 17.4 Hz and 34.7 Hz, respectively. These voltages are in close agreement with those values obtained from the theoretical calculation of induced voltage. The proximity between the data sets of lock-in and sound-card shows the promise of a soundcard for such characterization. Especially, we note that perpendicular magnetic

anisotropy films are relatively challenging samples for VSM characterization due to being very thin.

To confirm the coercivity field and perpendicular magnetic anisotropy of Co/Pt multilayer, we performed an Anomalous Hall effect measurement of the film. As shown in figure 4.7 (c), we have a perfect agreement with the VSM measurements, which strengthens the reliability of our audio-based VSM experiment.

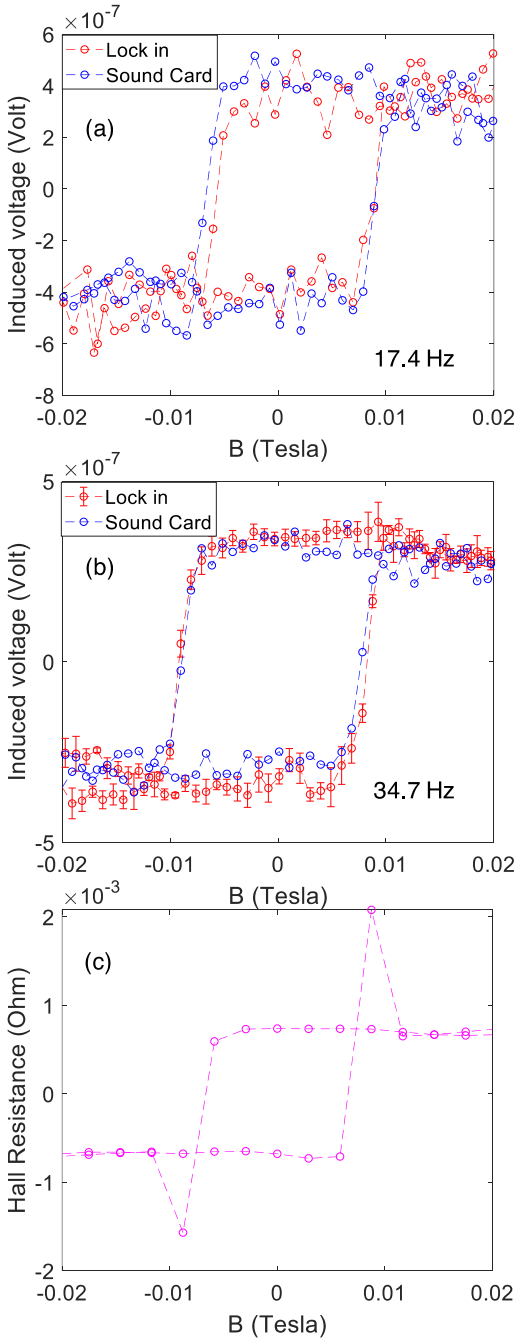

Figure 4.7. Induced voltages as a function of the applied field of the out-plane Co/Pt multilayers for lock-in amplifier (red) and soundcard (blue) at frequencies (a)17.4 Hz, (b)34.7 Hz. (c) Hall effect measurement of the same film.

4.4 Discussion and summary

In summary, we developed a low-cost but sensitive and versatile magnetometry instrument based on audio components, including a sound card, amplifier, and Laud speaker. We first tested the frequency responses of the LCR series circuit by using both the sound card and a commercial lock-in amplifier. This circuit test verified the frequency range of our sound card that can reliably measure a modulated signal. Next, we built a sensitive 4-coil VSM by utilizing the sound card, and the induced voltages were theoretically calculated for the coil geometry. We then measured the magnetization hysteresis curves of a Nickel piece, a 50-nm-thick Perm-alloy film, and a perpendicularly magnetized Co/Pt multilayer sample using the sound card and the lock-in amplifier. Two data sets obtained from two instruments were in perfect agreement. In addition, we confirmed the hysteresis curve of Co/Pt multilayer film with the Hall effect measurement. The noise of our sound-card based VSM is approximately 5.4×10^{-6} emu, which is obtained by vibrating the sample holder without any magnetic sample. The sensitivity and noise of VSM with a commercial LI amplifier were 2.02×10^{-6} emu and 3.8×10^{-5} emu at 34 .7 Hz, respectively. Although sound cards are not calibrated as an off-shelf scientific measurement unit, their high bit ADC and fast sampling rates can be exploited for measuring modulated signals, such as in VSM measurements, at a very low cost after calibrating with a lock-in amplifier or other means.

This chapter is published as a research article with light editing [98].

CHAPTER V

INTERFACE EFFECTS ON MAGNETIC ANISOTROPY AND DOMAIN WALL DEPINNING FIELDS IN PT/CO/ALO$_X$ ULTRATHIN FILMS

5.1 Introduction

Perpendicularly magnetized magnetic ultrathin films and their capability for data storage in memories and other recording media have been extensively studied for many years [99–101]. In earlier works, it has been established that perpendicular magnetic recording systems have much higher storage capacity and better thermal stability compared to systems based on conventional longitudinal recording technology [99,102]. Hence perpendicular magnetic anisotropic (PMA) films are widely applicable for next-generation low power, nonvolatile magnetic racetrack and shift memories [13,103,104].

In such memory devices, magnetic spin textures such as chiral domain walls (DW) and skyrmions are the key ingredients and their dynamics are crucial to storing the information in the form of bits. Study and manipulation of the depinning field that assists in moving such spin textures have received great attention. In DW-based racetrack memories, the defects in the ultrathin films hinder their mobility, and the depinning field surpasses the DW energy consumption that provides the motion. Previously, it was assumed that the skyrmion-based memories system is likely less affected by the pinning centers because of the skyrmion's unique topological properties.

However, the experimental results in ultrathin films performed by Yu et al. have shown the prominent effect of pinning centers even on the skyrmion motion as its size is much larger than the average distance between neighboring pinning centers [103,105]. These findings further emphasizes the importance of the depinning field on magnetic memory applications for DWs and skyrmions.

In magnetic thin film structures, the interfaces are critical for various magnetic parameters and interactions, including PMA [106,107], Dzyaloshinskii–Moriya interaction (DMI) [108,109], saturation magnetizations [110], exchange bias and coercivity fields [111–113]. In the past years, the dependence of annealing temperature and oxidation time on magnetic anisotropy in Pt/Co/AlO_x trilayers was experimentally observed [114,115]. Similarly, the comprehensive studies of current and field-induced DW dynamics [116–118], PMA, magneto-optical Kerr-effect and DMI [108,119–121] due to the transformation of the Co/AlO_x interface have been performed on Pt/Co/AlO_x material stacks. Recently, profound studies of electric field modulated DMI and spin-orbit torque (SOT) were done on the Pt/Co/AlO_x thin films strengthening the importance of ferromagnet (FM)/metal oxide (MO_x) boundary in low power electronics [122,123]. However, the impact of the AlO_x layer on the magnetic properties along with the DW dynamics and depinning fields is still not known. Known properties of the Co/AlO_x interface have already been utilized for the construction of energy-efficient spin-based memory and logic devices [124–126] pointing to the importance of understanding the influence of the AlO_x layer on the magnetic properties.

In this chapter, we present a novel method to optimize DW depinning fields, velocity, and other magnetic properties by controlling the aluminum oxide thickness in Pt/Co/AlO_x trilayers. Additionally, the coercivities of all samples were quantified and analyzed for the temperature range of 25 K to 300 K to study the oxygen-induced interface modification in these magnetic stacks. We found the variation in depinning fields and magnetic properties can be attributed to the oxidation of cobalt at the Co/AlO_x interface.

5.2 Experimental details

The Pt/Co/AlO_x (t nm) trilayers were deposited on a thermally oxidized silicon substrate by magnetron sputtering at room temperature with a base pressure of about 4×10^{-5} Pa. The sputtering rates of all the target materials were calibrated by using a Bruker Profilometer and found to be approximately $0.021 \pm 2.5\times10^{-4}$ nm/sec. The complete thin film stacks from the substrate side were Ta (10 nm)/Pt (4 nm)/Co (1.1 nm)/AlO_x (t nm)/Pt (4 nm) where, t =3, 3.6, 4.17, 4.58, 5, 5.4, 5.8, 6.2. Herein, heavy metals Ta (10 nm)/Pt (4 nm) were sputtered first as a buffer or seed layer to boost the PMA[127]. The top Pt layer acts as a capping layer to protect the film from oxidation. The aluminum metal sandwiched in between Co and Pt was oxidized for 17 seconds at the pressure of 2.93 Pa by using RF power at 40 watts before the deposition of top platinum. Multiple magnetic samples were grown by varying aluminum thicknesses (t_{Alo_x}) and the films were post-annealed at 460°C for 30 minutes under ultrahigh vacuum to improve crystallinity and thus promote PMA.

The magnetic characteristics were studied by hysteresis curves obtained from vibrating sample magnetometer (VSM) and anomalous Hall effect (AHE) systems at room temperature [98]. The dimensions of the sample pieces used in measurement were ranging from 4×4 mm^2 to 4×6 mm^2. In addition, DWs motion was studied by using a polar magneto-optical Kerr effect (P-MOKE) microscopy imaging system. For imaging purposes, samples were diced into small pieces sized around $5\ mm^2$ and the symmetric domain wall dynamics were investigated by applying out of plane (OOP) magnetic fields up to $40\ mT$. Next, the low-temperature AHE measurements were performed to study the effect of interfacial oxygen on magnetization. For the measurement, the samples were patterned in the form of Hall bar devices by using photolithography and plasma etch techniques. A Keithley 2450 source meter, monitored by LabView software, was used to supply the small current density on the order of $10^{11}\ A/m^2$ to measure the anomalous Hall

resistance. The layered structures of our samples were verified by using the transmission electron microscopy (TEM) imaging technique and a morphological study was carried out with the help of atomic force microscopy (AFM) images.

5.3 Results

5.3.1 Magnetic characterization

To find the PMA of the samples we first extract hysteresis curves taken from measuring hall resistance R_{Hall} and magnetization M as a function of the OOP magnetic field H_z at room temperature as displayed in figure 5.1 (a) & (b). This data shows very good PMA for the t_{AlO_x} range of 3 to 5.8 nm. However, the easy axis OOP anisotropy directions change into the easy plane for the thickness of 6.2 nm as displayed in figure 5.1 (a) observed in AHE measurement. Figure 5.1 (c) shows the inplane magnetoresistive behavior of a Pt (4 nm) /Co (1.1 nm) /AlO_x (4.58 nm) sample and the inset in figure 5.1 (c) is the Kerr image of the Hall bar device with the measurement scheme. From the hysteresis of figure 5.1 (c), we can easily recognize that R_{Hall} is maximum at zero in-plane field H_x and it begins to decline slowly on increasing the H_x, indicating the prominent magnetization of our sample along the OOP direction [128]. The coercive field H_c, anisotropy field and saturation magnetization M_s, extracted from hysteresis loops in figures 5.1 (b) and (c). The detailed method to find the magnetization in figure 5.1 (b) can be found in our previous work [98]. Similarly, interfacial PMA is given by the effective anisotropy energy density K_{eff} and it is extracted by using the relation $K_{eff} = \frac{1}{2}\mu_o H_{an} M_s$, where, H_{an} is the effective anisotropy field and is taken as the field corresponding to 90 % of the saturated anomalous Hall resistance value on AHE curves with an in-plane field [41,107]. The AlO_x thickness dependence of H_c, M_s and K_{eff} can be seen in Figure 1 (d). From figure 5.1 (d), it can be discerned that H_c rises remarkably from $0.68\ mT\ to\ 13\ mT$ while increasing t_{AlO_x} up to 5 nm thick AlO_x then it starts decreasing. In the same way, M_s is slightly descended for higher

t_{Alo_x} and K_{eff} is tuned lying within the range of 7 % of it's mean value, these small declination in M_s values may be due to the weak partial oxidation of cobalt at the interface.

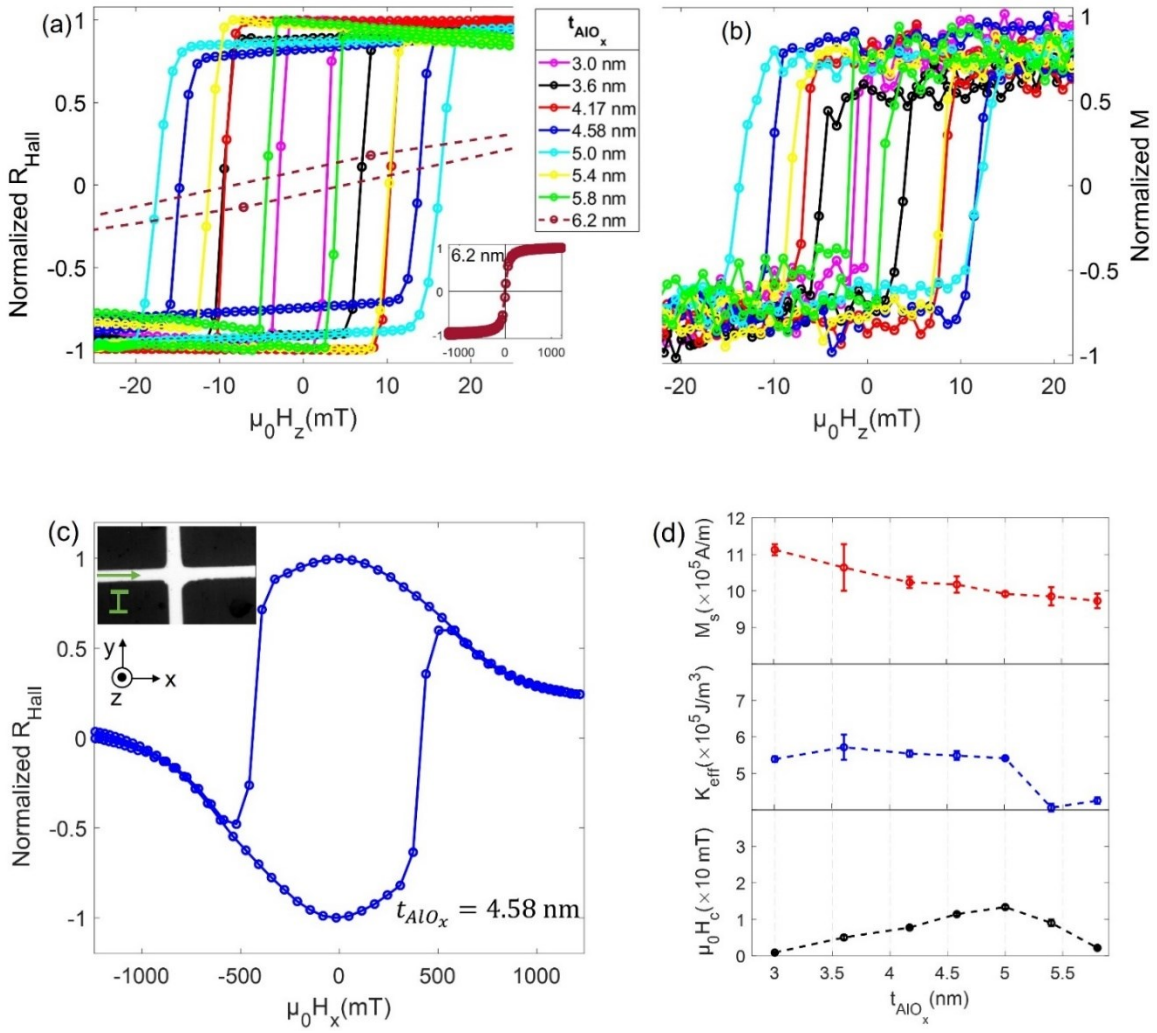

Figure 5.1. (a) Normalized hall resistance R_{Hall} as a function of OOP magnetic field (H_z).(b) Normalized magnetization M against the H_z. (c) R_{Hall} as a function of in-plane field H_x for Pt(4nm)/Co(1.1 nm)/AlO_x (4.58 nm) sample. (d) Variation of saturation magnetization, effective anisotropy and coercivity with the AlO_x thickness.

The inset on the bottom right of figure 5.1 (a) is the complete R_{Hall}-H_z loop for the Pt(4nm)/Co(1.1 nm)/AlO_x (6.2 nm) sample. The top left inset of figure (c) is the polar Kerr image

of the 27 μm channel width Hall bar device and the green arrow on it gives the direction of applied current during the measurement. Red, blue and black data points represent the saturation magnetization, effective anisotropy and coercivity with the AlO_x thickness in figure 5.1(c).

5.3.2 Domain wall velocity and depinning fields

For the quantification of DWs velocity and depinning fields on the magnetic samples, we studied the field-induced symmetric DW motion in the creep regime by using P-MOKE. This method is ideal for understanding the DW dynamics and is convenient without requiring any microfabrication. In our experiment, DWs motions were visualized and manipulated by 300 ms to 120 second H_z pulses of discrete amplitudes. The magnetic films were saturated by using a 1-second pulse of amplitude ± 40 mT H_z and DWs were nucleated by using opposite fields which are taken as reference images as seen in figure 5.2 (a). For every pulse, the DW displacements were taken as the subtraction of the reference image (figure 5.2 (a)) from the DW image after the pulse (Figure 5.2 (b)). The differential displacement of the magnetic bubble expansion is plotted versus different pulse durations of particular H_z amplitudes. Then, the gradients of the corresponding plots are taken as the DW velocities which are shown in figure 5.2 (d) as a function of t_{AlO_x}. We found that the film containing 5 nm AlO_x has the minimum velocity for all H_z ranging from - 8 mT to + 8 mT in 0.2-field point increments. However, the velocity of 5.8 nm AlO_x sample cannot be recorded in our experiment as the sample is comprised of weakly pinned magnetic DWs as shown in figure 5.2 (e).

By following the same procedure, the depinning fields were evaluated in our system, which is defined as the minimum applied fields at which DWs just start to expand [105] and the accuracy of our measurement system is on the order of 0.6 μm/s. This depinning field dependence on t_{AlO_x} is as shown in the figure 5.2 (e) and extremely small depinning field for the 3 nm sample could not be noted because it has extremely small coercivity at room temperature. It is found that the

strongest depinning field is for the 5 nm t_{AlO_x} sample and on increasing thickness it starts decreasing following the fashion of coercivity change in figure 5.1(d). Although this method of finding the depinning field is not very precise, as the DW motion in creep regime is also thermal energy dependent [129–131], it offers a very good approximation of its alteration trend [105].

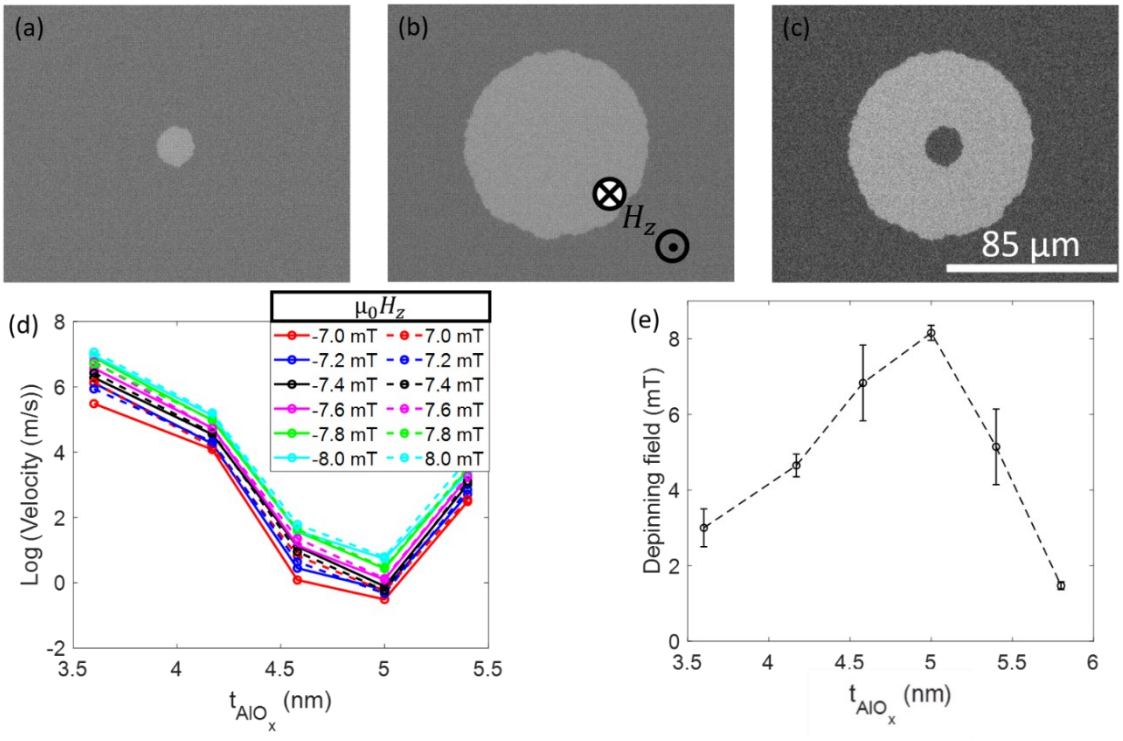

Figure 5.2. (a) Magnetic domain wall (DW) nucleated with a 1-sec pulse of OOP field H_z of -8.5 mT act as a reference image (b) DW driven with the 8-second pulse of -7.8 mT H_z, and (c) Differential image of DW corresponding to (a) and (b) of Pt (4 nm)/Co (1.1 nm)/AlO_x (5.8 nm) sample (d) DW velocity as a function of aluminum oxide thickness t_{AlO_x} for different OOP fields (e) Plot showing the dependence of the depinning field on t_{AlO_x} .

5.3.3 Material and morphological characterization

To observe the oxidation content at the interface, low-temperature magneto-transport measurements were carried out in our PMA samples. The magnetoresistive curves (figure 5.3 (a))

as a function of H_z show the hysteretic behavior at a low temperature of 35 K. We measured the coercivities for temperatures ranging from 25 K to 300 K for all the OOP anisotropic samples in figure 5.3 (b). In our low-temperature transport measurement system, the switching behavior of hysteresis loops could also be affected by the Joules heating effect due to the applied current. To minimize such effect, we applied the smallest possible current and coercivities are taken as the average of the switching fields for both up-down and down-up DWs.

At the lowest possible temperature in our system, we found that H_c increased with larger t_{AlO_x} until it reached 4.58 nm and then began dropping as shown in figure 5.3 (b). Refs.[115] and [132] contend that such a trend of transformation of H_c values is the signature of the formation of an antiferromagnetic CoO_x state at the Co/AlO_x interface due to the migration of oxygen along the grain boundaries. However, our 3.6 nm thick film behaved anomalously showing very weak coercivity at low temperature which may be due to the diffusion of oxygen away from cobalt.

All the material stacks on our thin films are displayed in the TEM image (figure 5.3 (c)) of Pt (4 nm)/Co (1.1 nm)/AlO_x (4.58 nm) trilayer. In this image, cobalt is barely distinguishable because of its very small thickness compared to other components. The RMS values of the roughness of our heterostructured surfaces were measured to be in the range of 0.5 to 0.85 nm from AFM measurements. The inset of figure 5.3 (d) shows a 4×4 μm^2 AFM image of the heterostructure with t_{AlO_x} = 4.58 nm and its roughness was found to be 0.77 ± 0.05 nm. The roughness of all the PMA samples is displayed in figure 5.3 (d). Although the roughness values of all measured films are very close, their values slightly declined for the films comprising higher and lower than 5 nm AlO_x thickness backing up the variation propensities of coercivity (figure 5.1 (d)) and depinning field (figure 5.2(e)). The lowest and highest roughnesses were recorded to be 0.49 ± 0.03 nm and 0.79 ± 0.03 for the sample of t_{AlO_x}= 3 nm and 5 nm respectively.

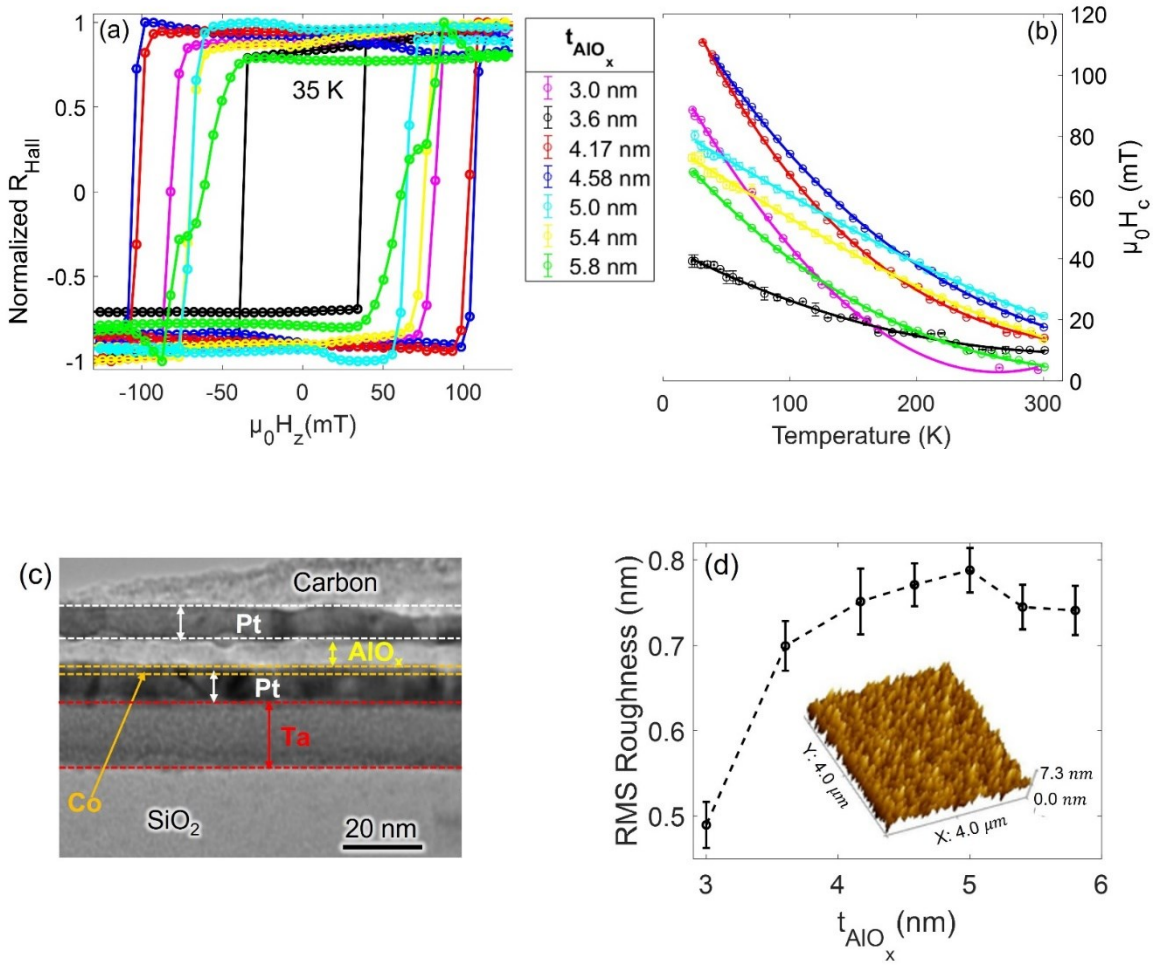

Figure 5.3. (a) Normalized anomalous Hall resistances versus OOP field Hz for different t_{AlO_x} measured at 35 K temperature (b) Temperature dependence of coercive fields for the sample of varying aluminum oxide thicknesses. (c) Transmission electron microscopy image of Pt (4 nm)/Co (1.1 nm)/AlOx (4.8 nm) sample. (d) The roughness of all PMA samples as a function of aluminum oxide thickness.

The inset of figure 5.3 (d) represents the 4×4 μm^2 atomic force microscopy image of Pt (4 nm)/Co (1.1 nm)/AlO_x (4.8 nm).

5.4 Discussion

By using the methods discussed above, we measured magnetic properties and depinning fields at room temperature and coercivities at the low-temperature range for various t_{AlO_x} of asymmetric Pt/Co/AlO_x trilayer systems; the respective results are provided in figures 5.1 (d), 5.2 (e), and 5.3 (b). The reason for the difference in magnetic parameters and non-monotonic behavior of depinning fields in this result can be twofold: interfacial effects and surface roughness of thin films. Regarding interfacial impact, this variation may be attributed to both the top Co/AlO_x and the bottom Pt/Co interfaces as claimed by Ref.[119]. At a high annealing temperature of 460°C, the formation of intermetallic CoPt alloy at the bottom interface reduces the pure metallic cobalt which might affect the magnetization values of the samples. However, our result (figure 5.3 (b)) supports that, these properties are predominantly determined by the modification of diffusion-caused oxygen content in the top Co/AlO_x interface where H_c values of all the samples are increasing on lowering temperature that arises due to the exchange coupling between ferromagnetic Co and antiferromagnetic CoO_x [18].

First, when the aluminum is oxidized after the Co deposition, some of the cobalt can be changed into cobalt oxide thinning the metallic cobalt which is responsible for the alteration of both MOKE and magnetic properties [133]. In addition to that, the enhancement of these quantities by increasing the t_{AlO_x} from 3.6 nm to 5.0 nm, may be due to the protection of cobalt from overdegradation by the thicker aluminum as the magnetic properties are determined by cobalt thickness [134]. On following this trend, abrupt reduction of the depinning field as well as the slight declination of other magnetic properties beyond the critical t_{AlO_x}= 5 nm might be due to the reduction of degree of oxidation at the interface [115]. Such adaptation of oxygen content at the interface is bolstered by low-temperature coercive field measurement results (Figure 5.3 (d)). On the other hand, magnetic properties including magnetization switching field and DW motion are highly dependent on the surface roughness of the ultrathin films [135–138]. This fact is bolstered by the aluminum oxide thickness-dependent RMS roughness of AFM measurement

(figure 5.3 (d)) which is consistent with the coercivity (figure 5.1 (d)) and depinning field (Figure 5.2 (e)) curves. On further increasing the thickness to 6.2 nm, the easy plane anisotropy direction is switched from perpendicular to in-plane (figure 5.3 (a)). This phenomenon occurred because the relatively thicker alumina does not allow enough oxygen to diffuse into the cobalt layer preventing the Co layer from being thin enough to easily magnetize it along the OOP direction as PMA is highly sensitive to ferromagnetic film thickness [139].

5.5 Conclusion

To summarize, we investigated AlO_x thickness dependence of saturation magnetization, effective anisotropy and coercivity of Pt/Co/AlO_x heterostructure by using vibration sample magnetometry and anomalous Hall effect measurement techniques. Although the change in saturation magnetization and anisotropy is very little, the strong dependence of coercivity with AlO_x thickness is observed and recorded maximum at 13 mT for 5 nm AlO_x. The domain wall depinning fields are quantified by studying field-driven DW dynamics, using polar MOKE. When the AlO_x thickness is 5 nm, the depinning field is maximum at around 8 mT and the DW velocity is minimum at 0.6 μm/s. This alteration is attributed due to the transformation of the Co/AlO_x interface and the degree of roughness of the films as supported by the results from low temperature (25 K-300 K) magnetoresistance and atomic force microscopy measurement techniques respectively. These results show the importance of FM layer oxidation to the depinning of chiral DWs in future spintronics devices.

This chapter is published as a research article [140]

CHAPTER VI

ENGINEERING PT/CO/ALO$_X$ HETEROSTRUCTURES TO ENHANCE THE DZYALOSHINSKII-MORIA INTERACTION

6.1 Introduction

The Dzyaloshinskii-Moria interaction (DMI)[59,141] is an antisymmetric exchange interaction between spins induced by broken inversion symmetry in magnetic materials either structurally or crystallographically. The DMI energy between any two neighboring spins $\boldsymbol{S_i}$ and $\boldsymbol{S_j}$ can be written as $H_{DMI} \propto (\boldsymbol{S_i} \times \boldsymbol{S_j})$, which causes non-collinear alignment of magnetic moments. The competition between DMI and Heisenberg interaction $\propto (\boldsymbol{S_i}.\boldsymbol{S_j})$ can leave the spins in a chiral state rather than a ferromagnetic state, which leads to the formation of exquisite spin textures such as chiral domain walls (DWs)[45], skyrmions [142], and other topological spin textures[143,144].

The topological properties of chiral spin textures have received considerable attention due to their possible applications in non-volatile spintronics devices [142,145–147] such as racetrack memories [13,147]. In addition, they can be driven at a very high speed with a low current using spin-orbit torques (SOT) and Zhang-Li spin-transfer torque [22,45,148–151]. In recent years, efforts have been made to study current-induced chiral DW motion [45], skyrmion dynamics [145,152,153] as well as to study the role of DMI in controlling the size of a skyrmion [154].

An important class of material systems to optimize the DMI is the heavy metal /ferromagnet /Oxide multilayer system with a perpendicular magnetic anisotropy (PMA)[128,155–157], where a strong spin-orbit interaction in the heavy metal layer and broken structural inversion symmetry of multilayer system modify the DMI. Moreover, the ferromagnetic layer's oxidation alters the PMA, which has been extensively studied previously[114,158,159]. However, the effect of oxidation of the ferromagnet on DMI is not thoroughly understood. The quantification of the DMI in these multilayer systems is critical for accelerating the realization of chiral spin textures-based spintronics applications. In this article, we control and quantify the DMI in Pt/Co/AlO_x trilayer system by varying the Al thickness, oxidation strength, annealing time, and substrate. After growing the multilayer films with a magnetron sputtering technique, we use asymmetric domain wall (DW) expansion using polar magneto-optical Kerr effect (MOKE) microscopy [41,160–162]. We fabricate micron-scale Hall-bar structures and determine magnetic anisotropy and the DMI effect on hysteresis curves. As a third method, we employ Brillouin light spectroscopy (BLS) techniques for the quantification of the DMI constant. Moreover, the enhancement of DMI is due to the different CoO_x content at the interface as evidenced by results from the X-ray photoelectron spectroscopy (XPS) and low-temperature anomalous Hall effect measurement technique. The presented findings are of high importance for understanding the role of ferromagnetic layer oxidation in magnetic stacks which have significant potential for future device applications in spintronics.

6.2 Experimental detail

The multilayers Ta (10)/Pt (4)/Co (1.2)/AlO_x (t)/Pt (6.7) were grown on thermally oxidized silicon and sapphire substrates, where the numbers in the bracket represent thickness in nm. The base pressure of the system was less than 10^{-6} Pa and the growth pressure were maintained at 267 mPa. In these multilayers, Ta is used to generate a smooth surface for the succeeding deposition, Pt is a heavy metal having high spin-orbit coupling, and Al was introduced to create

structural inversion symmetry breaking for the enhancement of DMI. The Al layer was oxidized with oxygen plasma for 15 seconds with the pressure maintained at 2.7 Pa and 44-Watt RF power. The top Pt layer acts as a capping layer to prevent further oxidation of the Al layer. We post-annealed the films at 350° C for varying time intervals in the growth chamber. Following the growth and overnight cooling, we characterize the unpatterned films using the MOKE microscope and vibrating sample magnetometry (VSM) for saturation magnetization and magnetic anisotropy values. Next, we use the ferromagnetic resonance technique to measure the damping parameter and magnetic inhomogeneity, the spectroscopic g-factor, and anisotropy. For the transport and hysteresis loop shift measurement, the samples were patterned into 27 μm Hall bar devices (figure 6.1 (a) inset) and the current density applied across the devices for the DMI measurement was $\sim 10^{10}\ A/m^2$. The interfacial DMI was quantified by the field-driven DW expansion method in the creep regime using polar MOKE microscopy, current-induced hysteresis loop shift method, and BLS measurement techniques. The layered structure of the stacks was ensured by JEOL JEM-2100 transmission electron microscopy (TEM) operated at 200 kV and different chemical environments of material in multilayers were investigated by using XPS and low-temperature anomalous Hall effect measurement techniques. For XPS measurements, the surface composition was measured for as-grown and sputtered films to study the Co oxidation at the Co/AlO_x interface. All samples were sputtered with Ar^+at 6.65×10^{-3} Pa. Sputter times were varied depending on the thickness of each sample.

6.3 Results and discussion

6.3.1 Magnetic characterization

The hysteresis curves were measured by sweeping the out of plane field (H_z) shown in figure 6.1(a), and their square shapes confirm the strong PMA nature of our samples. The saturation magnetizations (M_s) of the samples were derived from the magnetic hysteresis loops (presented in

the supplementary material figure 6.10(a)) measured by using VSM [98]. The anisotropy fields (H_k) were extracted from the magnetoresistance curve of the in-plane (IP) hysteresis loops (figure 6.10(b)) by applying a low DC current ~ 1 mA [41].The effective anisotropy field (K_{eff}) depends on M_s and H_k, and was calculated from the relation $K_{eff} = \frac{1}{2}\,\mu_0 M_s H_k$ [41,163,164]. The variation of areal magnetization ($M_s t$) and K_{eff} both lie within 25% of their average value for all the samples, as illustrated by figure 6.1 (b). This variation of the magnetic parameters with annealing time is an indication of a change in cobalt concentration due to the diffusion of oxygen at the Co/AlO_x interface and potentially intermixing of Co and Pt at the bottom Co/Pt interface at the high annealing temperature of 350 °C [25].

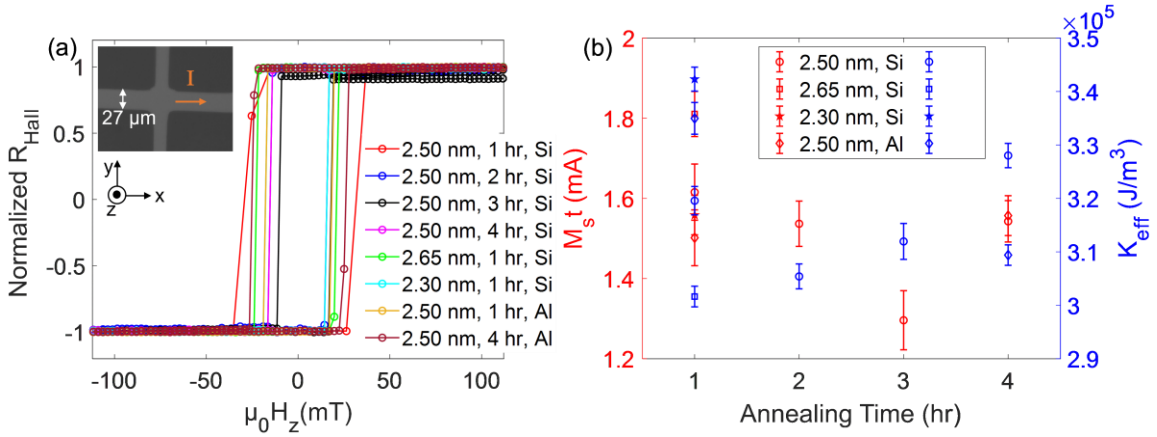

Figure 6.1. (a) Normalized hysteresis loops obtained from anomalous Hall effect measurements for the samples varying Al thickness (t_{Al}), annealing time, and substrate. (b) Areal magnetization (red) and effective anisotropy energy (blue) as a function of annealing time.

In the above figure 6.1, the first, second and third columns of the legend of (a) represent the aluminum thickness, annealing time and substrate (Si for SiO_2/Si and Al for Al_2O_3) respectively. The inset of the top left of (a) is the Kerr image of a patterned Hall bar device with a 27 μm channel width and an arrow (orange color) on it representing the applied current direction. The first and second columns of the legend of (b) represent the aluminum thickness and the substrate (Si for SiO_2/Si and Al for Al_2O_3).

Next, we utilized ferromagnetic resonance (FMR) spectroscopy to measure the damping parameter and magnetic inhomogeneity in the perpendicular geometry, the spectroscopic g-factor, and anisotropy. Our FMR spectrometer consists of a broadband (1-70 GHz) vector network analyzer to apply RF field via a coplanar waveguide (CPW) and measure the S12 parameter under a perpendicular magnetic field up to 2 Tesla. The field homogeneity over the sample volume is better than 0.1% and the field was measured with a Hall probe continuously. The samples are directly placed on the CPW upside-down after being coated with a thin polymethyl methacrylate (PMMA) to prevent shorting. The schematic of the sample placement is shown in figure 6.2(c) inset. Figure 6.2 shows examples of measured transmission parameter S12 as the magnetic field is swept through the resonances for the sample Pt (4)/Co (1.2)/AlO_x (2.5), which was grown on a SiO_2/Si substrate and annealed for 1 hour. The ferromagnetic resonance can be described by the complex susceptibility $\chi(H_{res})$ obtained from the Landau-Lifshitz equation [165,166]. For the OOP magnetic field geometry, $\chi(H_{res})$ is given by

$$\chi(H_{res}) = \frac{M_{eff}(H_{res}-M_{eff})}{(H_{res}-M_{eff})^2-H_{eff}^2-i\Delta H\,(H_{res}-M_{eff})}, \tag{6.1}$$

where H_{res} is the resonance field, ΔH is the linewidth, $H_{eff} = 2\pi f/(\gamma\mu_0)$, $M_{eff} = M_s - \frac{2K_{eff}}{\mu_0 M_s}$ is the effective magnetization, f is the microwave frequency, $\gamma = g\mu_B/\hbar$ is the gyromagnetic ratio, μ_B is Bohr magneton and $\hbar$ is the reduced Planck's constant. Figures 6.2 (a) and (b) show examples of the spectra at multiple frequencies. We simultaneously fit the real and imaginary parts of Eq. (6.1) to determine H_{res} and ΔH. The fitted curves are also shown in figures 6.2 (a) and (b). The resonance field and frequency are related to each other by the Kittel equation

$$f(H_{res}) = \frac{g\mu_0\mu_B}{2\pi\hbar}(H_{res} - M_{eff}). \tag{6.2}$$

By fitting Eq. (6.2) to the data in figure 6.2 (c), we find M_{eff}= -(0.413 ± 0.01) T and g = 2.144 ± 0.037. The wide error bars associated with the determination of the g-factor may be due to our extremely small magnetic film thickness, high damping, and large linewidth for all frequencies which results in a low signal-to-noise ratio.

In the framework of the Landau-Lifshitz equation, the linewidth depends linearly on the microwave frequency and the phenomenological damping parameter α by

$$\Delta H = \frac{4\pi\alpha}{\gamma\mu_0} f + \Delta H_0, \tag{6.3}$$

where ΔH_0 is the inhomogeneous broadening. By using Eq. (6.3), as shown in figure 6.13, we determined α=0.169 ± 0.015 and $\mu_0 \Delta H_0$= 0.003 ± 0.02 T. Because of the large damping and spin-pumping into the Pt layer the ΔH_0 determination was not precise.

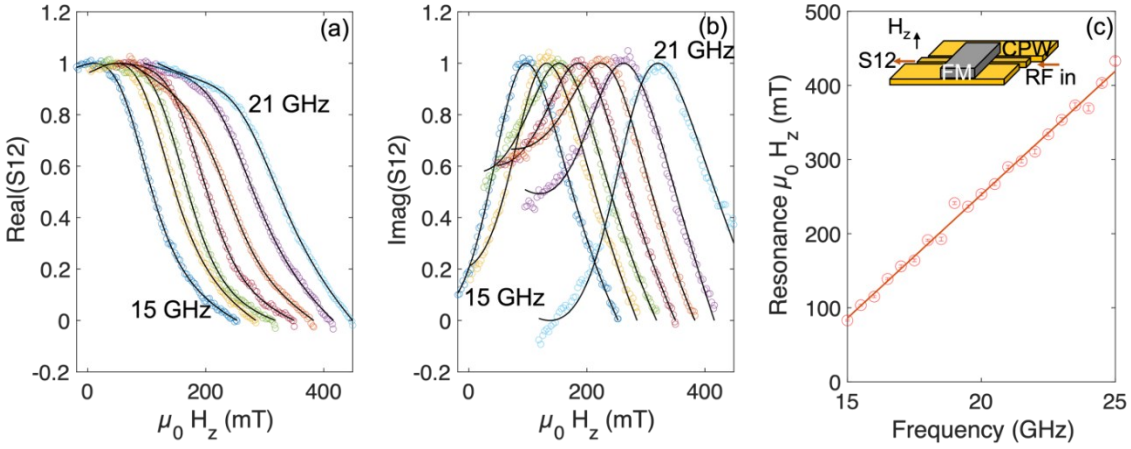

Figure 6.2. Ferromagnetic resonance spectrometry results for 1-hour annealed Pt (4)/Co (1.2)/AlO_x (2.5) film grown on SiO_2/Si substrate. (a) and (b) real and imaginary parts of the S12 parameter, respectively. (c) The resonance field vs microwave frequency and the linear fit.

6.3.2 DMI characterization

We used polar MOKE microscopy to adopt the method of asymmetric DW expansion in the presence of the in-plane field (H_x) for the quantification of DMI. The DW motion was studied in a creep regime where the velocities of DWs are slow and easy to capture by our MOKE microscopy following millisecond magnetic field pulses. The velocity in this regime depends exponentially on the H_z field [167], i.e., $\ln[v] \propto H_z^{-\frac{1}{4}}$ as shown in figure 6.12 (a) of the supplementary material for the sample Pt (4)/Co (1.2)/AlO_x (2.5) annealed for four different time intervals at 350 °C. For the study of DW dynamics in attendance of H_x, we saturated our sample by applying a relatively high field, $\mu_0 H_z = \pm 35$ mT. Then, the DWs were nucleated by the opposite H_z pulse which acts as the reference image for measuring the distance of the DWs expansion. During the experiment, the sample was at the center of the magnetic pole pieces of the electromagnet to eliminate other stray fields and was aligned horizontally to make sure that there was no H_z component of the in-plane magnetic field as it could influence the DW motion exponentially. Such alignment was tested by applying $\mu_0 H_x$ ~350 mT in the absence of H_z and found no expansion of DWs. The reference DWs were expanded in the creep regime with the H_z pulse of 0.3 s to 2 s duration under various H_x. The DW expansions are symmetric at $\mu_0 H_x = 0$ as seen in figures 6.3 (a) and (d). However, the right and left side DWs expansion are asymmetric under non-zero H_x as shown in figures 6.3 (b), (c), (e), and (f). Our explanation for this asymmetry is that the DWs in our magnetic thin films are Néel rather than Bloch type due to the broken symmetry in the normal direction of the film.

In addition, for these thin films which have strong PMA and DMI, the spins at the center of DWs are aligned in a specific direction by the chirality, and an effective magnetic field becomes important, referred to as the DMI field (H_{DMI}). This field, along with H_x , has a significant role in the determination of the DW's surface energy and their velocities of expansion [1]. When the DWs, expanded due to the H_z pulse, are further subjected to H_x their configuration will be broken and down-up & up-down DWs acquire different velocities along the direction of H_x as illustrated

by the right edge velocity $(v) - H_x$ plots in figures 6.4 (a)-(d). We note that down-up (figure 4 - red data points) and up-down (figure 4 - black data points) DWs have minimum velocities for the specific non-zero value of H_x , at which point H_x balances the effective DMI field H_{DMI} [161]. The extracted H_{DMI} fields are used to calculate DMI constant D from the relation; $H_{DMI} = \frac{D}{\mu_0 M_s}\sqrt{K_{eff}/A}$ [1,167], where A is the exchange stiffness constant and its value was assumed to be $16\ pJ/m$ [55]. The H_{DMI} (red data set) and D (blue data set) are plotted as a function of annealing time for the different set of samples as given in figure 6.5. Although there are a few drawbacks [168,169], we observed good agreement with the additional DMI measurements on most films.

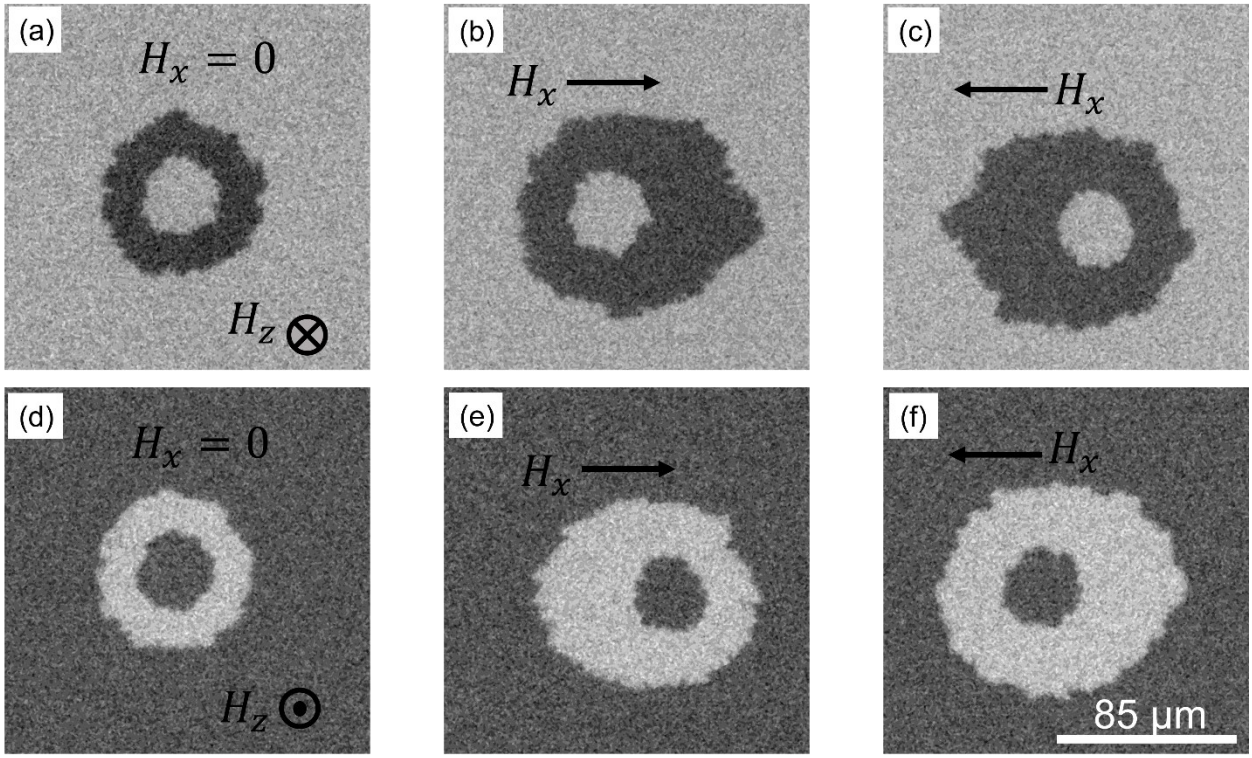

Figure 6.3. Magnetic domain walls expansion under 2-dimensional magnetic fields.

Figure 6.3 shows the expansion of domain walls driven by the out of plane magnetic field $\mu_0 H_z = \pm 9.5$ mT observed in polar magneto-optical Kerr effect microscopy for Pt (4)/Co (1.2)/AlO_x (2.5)

grown on SiO_2/Si substrate and annealed for 4 hours at various IP magnetic fields. (a),(d) at $\mu_0 H_x = 0$ with 1 s pulse (b) at $\mu_0 H_x = 85$ mT with 2 s pulse (c) at $\mu_0 H_x = -95$ mT with 600 ms pulse (e) at $\mu_0 H_x = 75$ mT with 2 s pulse (f) at $\mu_0 H_x = -70$ mT with 1 s pulse.

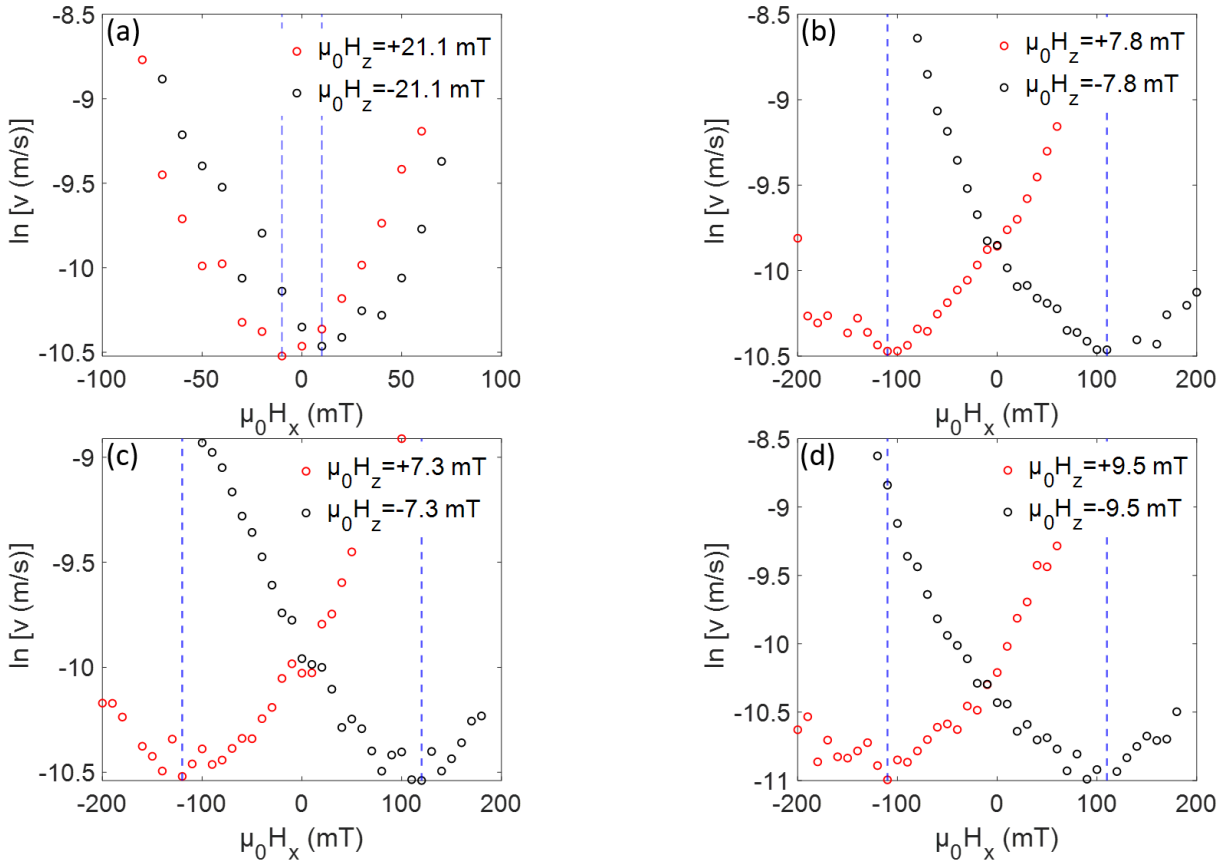

Figure 6.4. Right edge velocity of domain walls as a function of in-plane field (H_x) for Pt (4)/Co (1.2)/AlO_x (2.5) on a SiO_2/Si substrate with (a) 1-hour (b) 2-hours (c) 3-hours (d) 4-hours annealing.

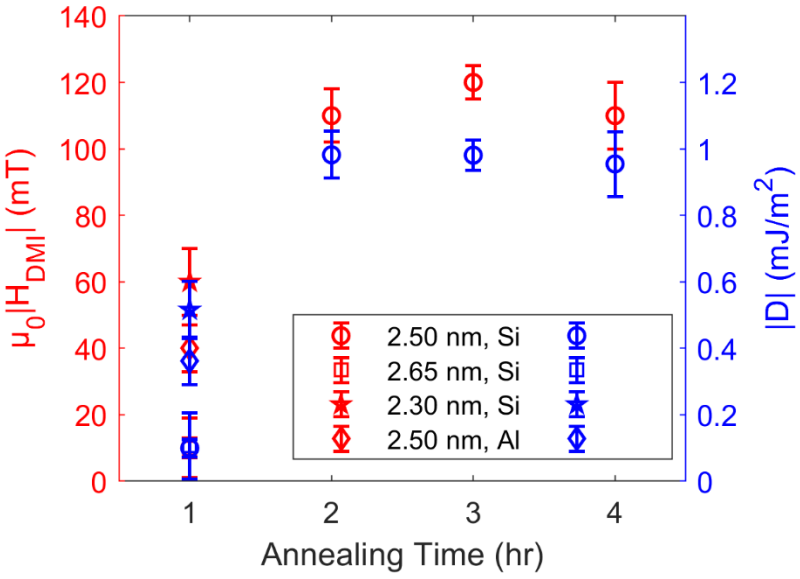

Figure 6.5. Dzyaloshinskii-Moria interaction field (red) and constant (blue) as a function of annealing time.

In figure 6.5, the circles, squares, stars and diamonds symbols represent Pt (4)/Co (1.2)/AlO_x (2.5), Pt (4)/Co (1.2)/AlO_x (2.65), Pt (4)/Co (1.2)/AlO_x (2.3), grown on SiO_2/Si substrate and Pt (4)/Co (1.2)/AlO_x (2.5) grown on Al_2O_3 substrate, respectively by using polar magneto-optical Kerr effect microscopy.

Secondly, we adopted a current-induced hysteresis loop shift method to quantify the DMI, which was developed by Pai et al. [17] and its measurement configuration is demonstrated in figure 6.6 (a). In this method, when an IP current (I) flows along the x-direction through the heavy metal (i.e. Pt), the electrons with opposite spins align at the top and bottom interface of the thin film, and a spin current is generated along the z-direction. This spin current gives rise to Slonczewski-like SOT, which is responsible for the generation of an effective field (H_z^{eff}) along the z-direction as explained by the relation[45,170]: $H_z^{eff} \propto \boldsymbol{m} \times (\boldsymbol{z} \times \boldsymbol{J_x})$ where J_x is the charge current density along the x-direction. This effective field is equal and opposite to the DMI caused by down-up and up-down Néel DWs because of their antiparallel orientation of magnetic moments.

However, in the presence of H_x, the moments of chiral DWs tend to align along the direction H_x that produces an opposite H_z^{eff} with an unequal magnitude. So there exists a net positive (or negative) H_z^{eff} field depending on the direction of H_x and the in-plane DC current. This net effective field is responsible for shifting of the hysteresis loop as seen in figure 6.6 (b) and the measured shift can be taken as H_z^{eff}. In this plot, black data points and red data points represent the anomalous Hall resistance measurement as a function of H_z field for positive (+15 mA) and negative (-15 mA) IP currents respectively with the bias field of 146 mT for Pt (4)/Co (1.2)/AlO_x (2.5) sample annealed for three hours. Moreover, H_z^{eff} depends linearly on the current density as verified by the plot of H_z^{eff} as a function of I in the presence of two equal and opposite IP biased fields given in figure 6.6 (c). While calculating loop shift, H_z^{eff}, we were aware that DWs switching field could change due to IP current as well as Joule's heating effect. The latter effect was eliminated by measuring the shift of the center of hysteresis which was achieved by taking the average of the absolute values of switching fields for down-up (H_{D-U}^{sw}) and up-down (H_{U-D}^{sw}) DWs[17,120]. Then, we measured the shift for several H_x and found it saturates as H_x increases, as the magnetizations of the DMI-induced Néel DWs aligned in the direction H_x. This specific value of H_x was taken as H_{DMI} as shown in the plot in figure 6.6 (d). We found $\mu_0 H_{DMI}$ = $(131 \pm 5) mT$ and $(123 \pm 5)\ mT$ for the Pt (4)/Co (1.2)/AlO_x (2.5) samples annealed for 3 and 4 hours, respectively. By using the same equation as used by the asymmetric DW expansion section, the D values were calculated to be $(1.13 \pm 0.04)\ mJ/m^2$ and $(1.06 \pm 0.03)\ mJ/m^2$ for the respective samples.

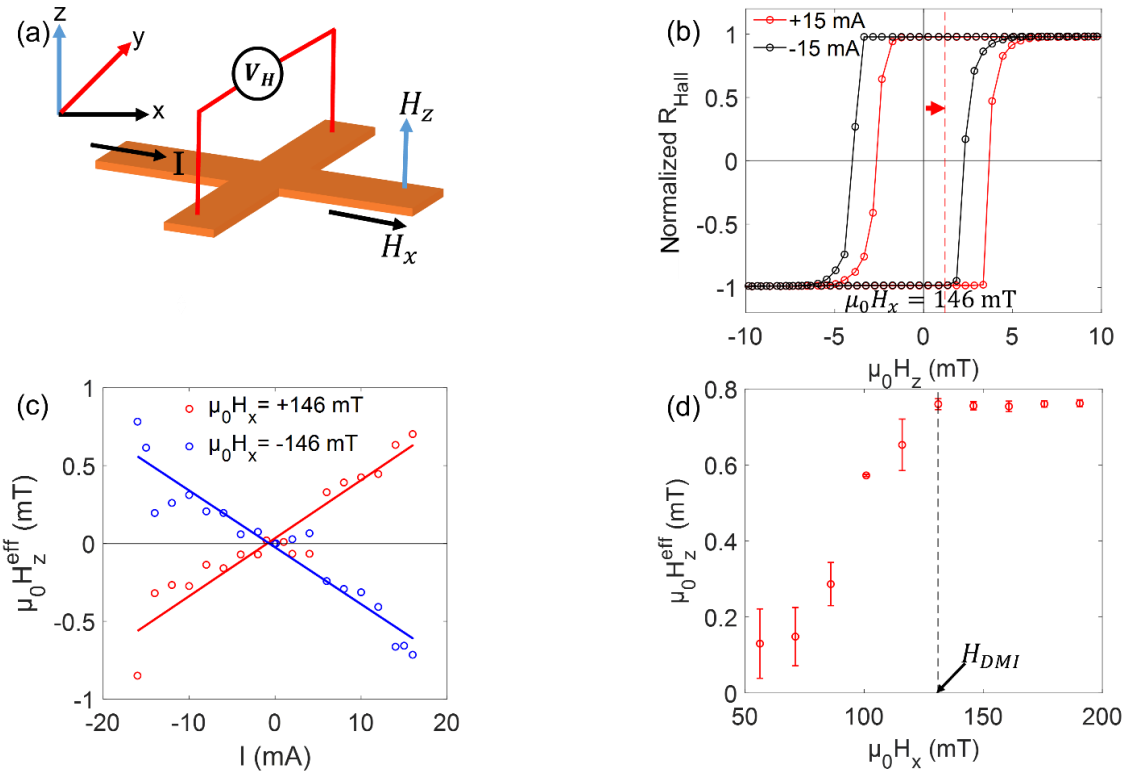

Figure 6.6. (a) Schematic for the hysteresis loop shift Dzyaloshinskii-Moria interaction measurement under the 2-dimensional magnetic fields (b) Normalized Hall resistance measurement (c) Effective H_z field as a function of in-plane direct current (d) Effective Hall field along z-direction due to spin Hall effect as a function of inplane field.

All the plots shown in figure 6.6 are for the sample Pt (4)/Co (1.2)/AlO_x (2.5) on SiO_2/Si substrate that was annealed for 3 hours.

Finally, the DMI of Pt (4)/Co (1.2)/AlO_x (2.5) stacks were studied using Brillouin light spectroscopy (BLS), where spin-wave (thermal magnons) frequencies are measured in ferromagnetic materials. In multilayers with broken inversion symmetry at the interfaces, the DMI modifies the spin-wave dispersion relation and dispersion curves become asymmetric, known as non-reciprocal spin-wave dispersion, as illustrated by figures 6.7 (a) and (b). The frequency shift Δf due to the DMI is given by [171]:

$\Delta f = \frac{g\,\mu_B\,D\,k_x}{\pi\,\hbar\,M_s}$ where g and k_x are an in-plane spectroscopic splitting factor (i.e., g-factor) and magnitude of spin waves vector along the x-direction respectively. The g values are determined by using FMR spectra as explicated in the material characterization section above. Detailed experimental techniques can be found in the reference [171]. The Δf of Pt/Co/AlO_x(2.5)/Pt stack for 1 hour and 4 hours annealed samples were measured to be $(5.7 \times 10^{-1} \pm 2 \times 10^{-2})$ GHz and $(4.9 \times 10^{-1} \pm 2 \times 10^{-2})$ GHz respectively. The corresponding DMI values calculated using the above equation are $(0.82 \pm 0.03)\ mJ/m^2$ and $(0.62 \pm 0.03)\ mJ/m^2$ respectively. We note that the sample annealed for four hours shows larger full width at half maximum (FWHM) compared to the one annealed for one hour. The discrepancy between the full width at half maximums of figures 6.7 (a) and (b) curves can be attributed to the differences in surface roughness, damping, or spin pumping which can alter during a longer annealing process.

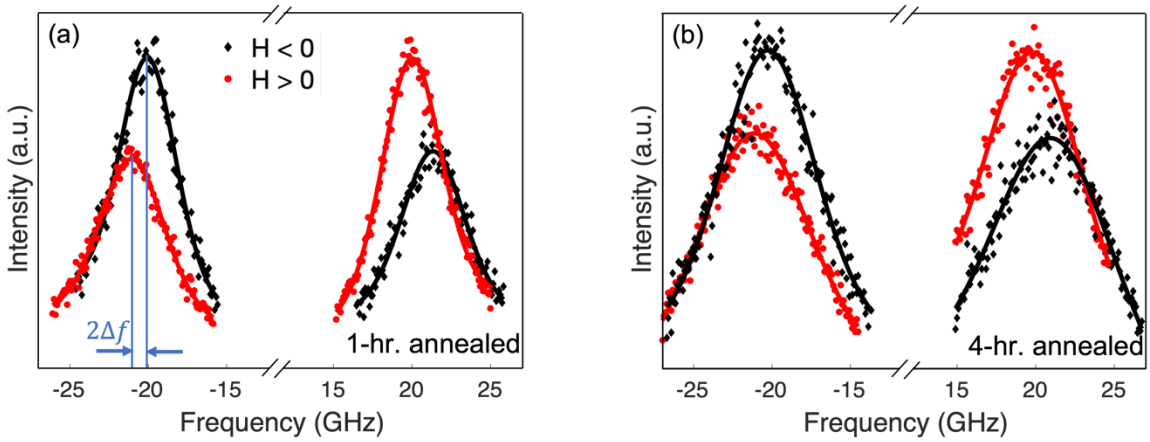

Figure 6.7. Spin wave spectra obtained from Brillouin light spectroscopy measurement technique for (a) 1-hour (b) 4-hour annealed Pt (4)/Co (1.2)/AlO_x(2.5) sample grown on SiO_2/Si substrate.

To summarize this section, the DMI constants (D) were accentuated up to ~1.13 mJ/m^2 for Pt (4)/Co (1.2)/AlO_x(2.5) as agreed by all three measurement techniques as displayed in figure 6.8 though there are tiny deviations in their quantitatively measured values. The minimum value of D was recorded as low as 0.1 mJ/m^2 from the study of field-driven DW dynamics. However, this

D value is weaker than that of the BLS measurement result for the same sample. It might be due to the different approaches for probing the film in BLS and p-MOKE microscopy measurement techniques [162,172,173]. Initially, that non-zero D is attributed to the structural inversion symmetry breaking when the AlO_x, which has very weak spin-orbit coupling (SOC) and no contribution to the DMI on its own, is introduced on the symmetric Pt/Co/Pt. In addition to that, several other interesting mechanisms are responsible for the variation of D due to the insertion of AlO_x. First, the Co layer might be partially oxidized as it is in direct contact with AlO_x modifying the Co (1.2)/AlO_x (t) interface which changes the interfacial DMI with the Pt layer[41,174]. Second, the annealing time can alter the epitaxial relationship between the layers and the bottom Pt layer. This might induce lattice strain at the interface, where the SOC is affected due to the lattice mismatch between the top Co and AlO_x layers [175]. Moreover, a longer thermal annealing duration might improve the ordering of atoms at the Pt/Co interface although there exist small chances for the formation of CoPt alloy deteriorating the interfacial quality. Such interfacial deformation gives rise to DMI since the DMI is susceptible to the atomic arrangement at the interfaces [176,177]. Therefore, the bottom Pt/Co interface may also be partially responsible for the alteration of interfacial DMI. Finally, a large interfacial electric field induced by the interfacial oxidation, originating from the transfer of charge, surpasses the very small SOC [119] of the atoms at the Co/AlO_x interface contributing to the large DMI [178]. In our case, the degree of oxidation of Co is changed as it was annealed for distinct time intervals leaving less cobalt in between Pt and AlO_x layers as confirmed by the XPS results that would be discussed in the material characterization section in detail. Thus, the enhancement in the DMI for the tri-layer system grown on the same substrate is due to the interface modification of the top Co/AlO_x interface. On the other hand, for our same stacks grown on two different substrates (i.e. SiO_2/Si and Al_2O_3), the DMI values differ by some magnitude that might be due to the different lattice mismatch between magnetic films and the substrates. Those lattice mismatches induce the

discrete lattice strains that alters the anisotropy and DMI as well [179–181].

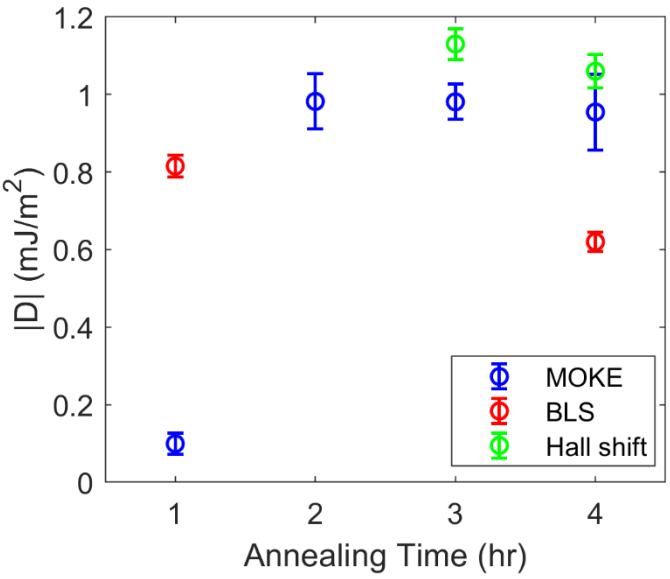

Figure 6.8. Dzyaloshinskii-Moria interaction constant measured as a function of annealing time.

In this figure blue data points, red data points green data points correspond to the MOKE microscopy, BLS, and Hall shift measurement techniques respectively for the sample Pt (4)/Co (1.2)/AlO_x (2.5) grown on SiO_2/Si substrate.

6.3.3 Material characterization

Following our magnetic characterization, we employed X-ray photoelectron spectroscopy (XPS) with Ar^+etching technique for the investigation of the chemical composition of our multilayer stack. The high-resolution spectra of Co 2p core-level state, from as-grown to 90 minutes etching time in every 15 minutes time interval, for 1 hour and 3 hours annealed Pt (4)/Co (1.2)/AlO_x (2.5) heterostructures are included in the supplementary materials figures 6.11 (a) and (b). All the as-grown samples do not show the signal of Co because they have a protective thick Pt layer on top of it, but once this layer has been removed by Ar^+sputtering the signal from Co starts to appear.

Particularly, a peak centered around binding energy of 778.1 eV is seen clearly. This indicates the presence of metallic cobalt underneath the Pt capping layer.

To study the oxidation state of the Co at the Co/AlO_x interface, we have analyzed the spectra (figure 6.9) from the 75 minutes sputtered samples for the same Pt (4)/Co (1.2)/AlO_x (2.5) stack. In the plots, the high-resolution XPS spectra of the Co 2p region, for samples annealed for 1 hour (figure 6.9 (a)) and 3 hours (figure. 6.9 (b)), have been deconvoluted using Gaussian fitting. Both spectra can be deconvoluted into four different sub-peaks: Metallic cobalt, Co^{2+}, Co^{3+}, and Co satellite. These peaks in both samples are centered at binding energies of 778.3 eV, 780.3 eV, 782.4 eV, and 785.0 eV, respectively. These results confirm the co-existence of Co and CoO_x at the interface [120,182]. However, the area under these peaks varies for each sample, which is an indication of different concentrations of Co states depending on the annealing time. The estimated ratios of metallic Co and the oxide of Co were found to be 1:0.89 and 1:1.35 with the annealing times 1 hour and 3 hours, respectively, which is evidence for the significant difference in oxygen content at the Co-Al interface of the discrete time-annealed sample. In addition, we performed the low-temperature anomalous Hall effect measurement technique as presented in figure 6.9 (c) and more detailed plots in figure 6.12 (b) of the supplementary material. We extracted the coercivities at the measured temperatures ranging from 15 K to 300 K. All of the four samples have relatively larger coercivities at low temperatures and H_c is highest for the 3 hours annealed sample confirming the strong oxidation states due to the oxygen migration at the interface [115]. However, on increasing the annealing time further (i.e. for the four-hour annealed sample) the coercivity value began to reduce which might be attributed to the diffusion of oxygen away from the cobalt layer [114,159]. In addition, a cross-sectional view of our multilayer magnetic sample using transmission electron microscopy is displayed in figure 6.9 (d). The individual layers in our samples are easily distinguished and show clear modification at the Co and Al interface due to the annealing-induced diffusion of oxygen.

Both XPS and low temperature anomalous Hall effect measurement results showed a very good agreement about the oxide concentration on the Co-Al interface and found that it was highest for the three-hour annealed sample. This physical characterization supports our claim about the impact of oxygen content on the interface for tuning the DMI as calculated and stated in the previous section for the Pt /Co/AlO_x tri-layers, based on different annealing time intervals and Al thicknesses grown on the silicon wafer.

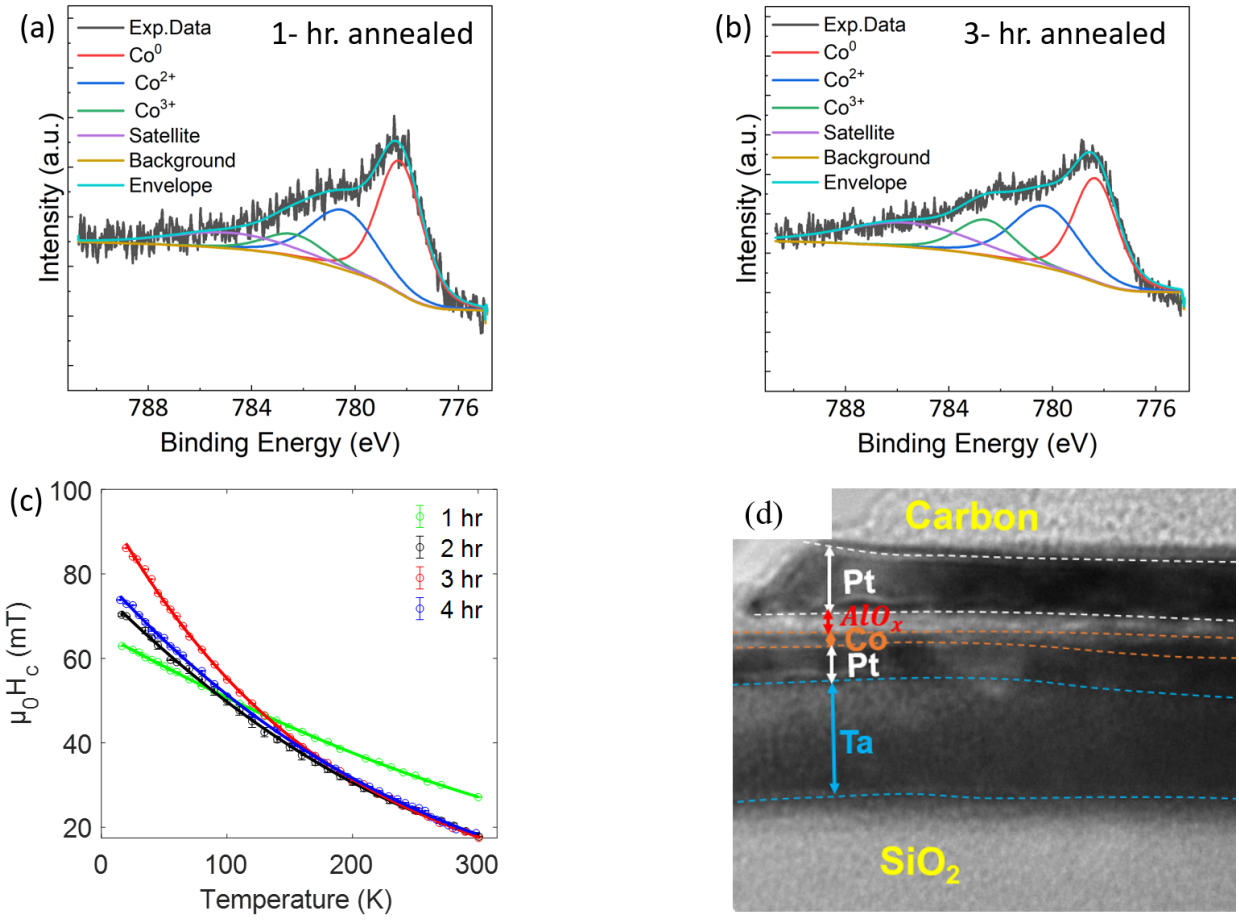

Figure 6.9. (a) and (b)The experimental and fitted X-ray photoelectron spectroscopy spectra of Co 2p state for annealed for 1 hour and 3 hours respectively. (c) Coercive fields Vs temperature. (d) Transmission electron microscopy images for the sample annealed for 1 hour.

Figure 6.9 corresponds to the sample Pt (4)/Co (1.2)/AlO_x (2.5) grown on SiO_2/Si substrate.

6.4 Conclusion

In summary, we have shown that variation of the oxygen level at the Co-AlO_x interface in a perpendicularly magnetized Pt (4)/Co (1.2)/AlO_x (t) trilayer structure can significantly affect the interfacial Dzyaloshinskii-Moria interaction. We measured the enhanced DMI constant from $(0.10 \pm 0.02)\ mJ/m^2$ to $(1.13 \pm 0.04)\ mJ/m^2$ using comprehensive characterization methods including MOKE microscopy, Brillouin light spectroscopy, and hysteresis loop shift measurement technique for samples with different annealing times, Al thickness, and base substrate. Interestingly, we found little deviation in the values obtained from each approach for the specific samples, with the trend of incremental changes in the DMI remaining the same. This points to the variation of oxygen content at the interface as illustrated by the results obtained from X-ray photoelectron microscopy, and low-temperature Hall effect measurement techniques. Our study is helpful for understanding the microscopic mechanism influencing the magnetic behavior of layered films when subjected to standard processing procedures. This knowledge can benefit the optimization of material combinations to enhance the DMI when designing ultrathin films to stabilize skyrmions for future use in low-power magnetic memories.

6.5 Supplementary materials

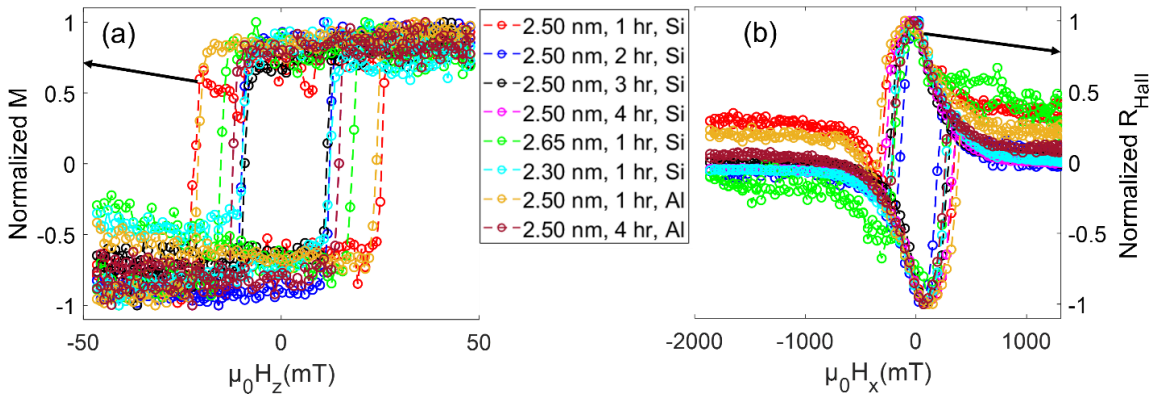

Figure 6.10. Hysteresis loops (a) Normalized magnetization (M) as a function of OOP magnetic field (b) Normalized Hall resistance as a function of in-plane magnetic field.

Both Figures (a) and (b) above share the same legend placed in the middle. The first, second and third columns of the legend represent the aluminum thickness, annealing time and substrate (Si for SiO_2/Si and Al for Al_2O_3) respectively.

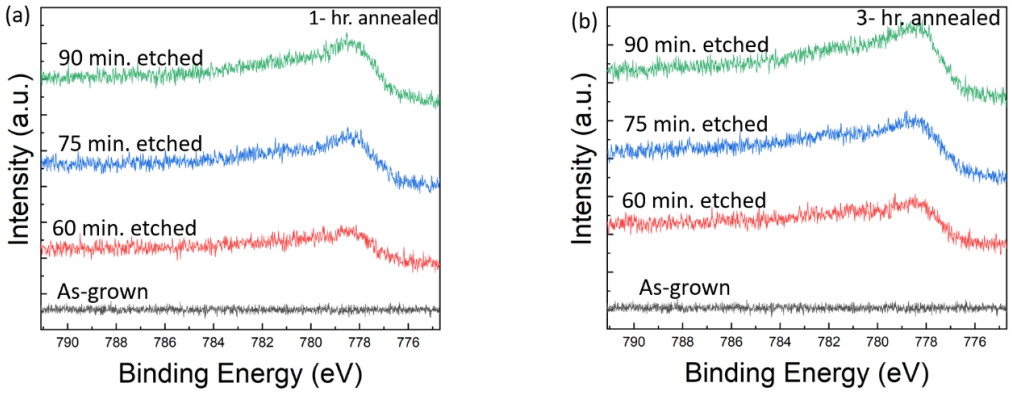

Figure 6.11. High-resolution XPS spectra representing Co-2p states of (a) 1-hour annealed and (b) 3-hours annealed Pt (4 nm)/Co (1.2 nm)/AlO_x (2.5 nm), grown on SiO_2/Si substrate.

During XPS, the samples were etched at different times. It was found that no cobalt peak appeared for the as-grown sample, however, it started to be discernible for the distinct time-sputtered samples.

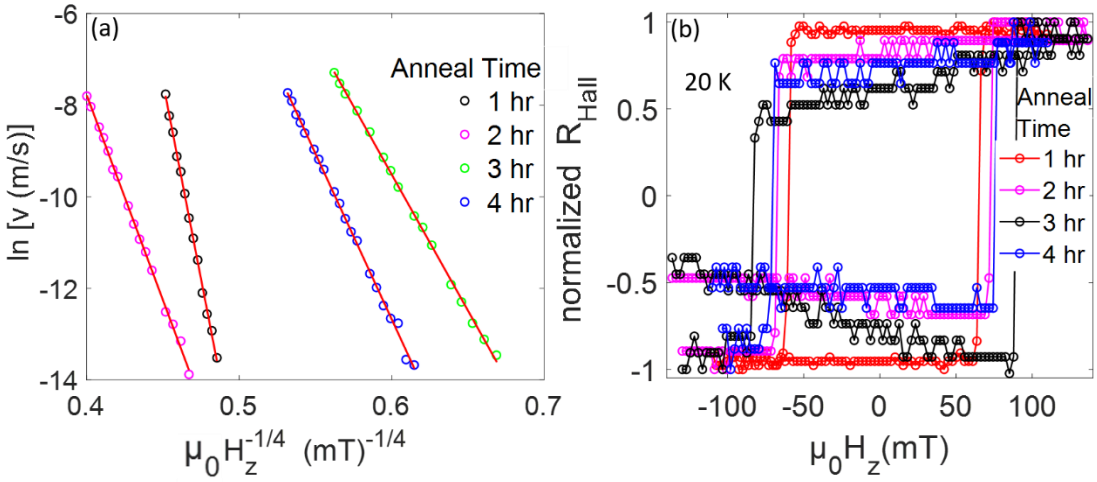

Figure 6.12. (a) The velocity of DWs versus OOP field fitting creep law (b) Normalized Hall resistance measured at 20 K for 4 different times annealed Pt (4 nm)/Co (1.2 nm)/AlO_x (2.5 nm) sample grown on SiO_2/Si substrate.

In figure 6.12 (a) each different colored circles represent the experimental points and the corresponding red-colored solid lines are the fitted ones.

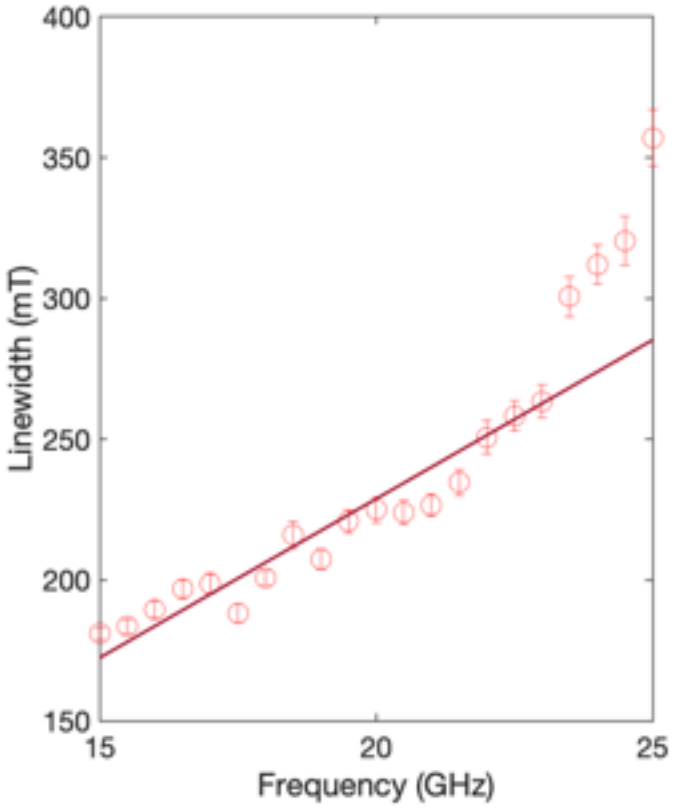

Figure 6.13. Linewidth plotted as a function of microwave frequency for the 1-hour annealed Pt (4 nm)/Co (1.2 nm)/AlO_x (2.5 nm) sample grown on SiO_2/Si substrate.

This figure displays the linear relation between microwave frequency and linewidth and follows the Landau-Lifshitz equation. Circles with error bars are the experimental data points and the solid line represents the fit for the 1-hour annealed Pt (4 nm)/Co (1.2 nm)/AlO_x (2.5 nm) sample, grown on SiO_2/Si substrate.

This chapter is published as a research article [183]

CHAPTER 7

SUMMARY AND OUTLOOK

7.1 Summary

In this thesis, a low-cost vibration sample magnetometry is built up using audio components for the magnetic measurements, and the dynamics of chiral domain walls are studied investigating the interface effects on depinning fields, Dzyaloshinskii-Moria interaction and other magnetic parameters in ultrathin Pt/Co/AlO_x heterostructures.

Primarily, the vibration sample magnetometer was developed to measure the magnetization of our magnetic samples. The working performance of VSM with two distinct data acquisition systems: a sound card and lock-in amplifier were studied. The experiment was conducted for three distinct samples: Nickel rod, Permalloy thin film and Co/Pt multilayers. It was observed the sound card-based VSM has better sensitivity (as high as ~ 2 micro-emu at 34.7 micro-emu) compared to that of VSM with a commercial lock-in amplifier. Those results are advantageous for the precise quantification of the magnetic moment of our magnetic samples.

In the second part, the impact of the aluminum thickness of Pt/Co/AlO_x heterostructure on the magnetic anisotropy, saturation magnetization, coercivities and depinning fields at room temperature were investigated. Also, the interfacial qualities and surface roughness of our thin films were studied by using magneto-transport measurement and atomic force microscopy. This study showed the significant alteration of magnetic characteristics with the oxidized aluminum thickness as explained in chapter 5 in detail. M_s values decrease for higher aluminum thickness

as explained in chapter 5 in detail. Ms value decrease for higher aluminum thickness due to the formation of CoO_x at the Co/AlO_x interface, however, the coercivity and depinning fields are maximum at 5 nm aluminum thickness and decrease above and below this critical thickness. The slight changes in magnetic anisotropy arise due to the PMA competition between top Pt/Co and bottom Co/AlO_x interfaces. The experimental results showed that the bottom interface (Co/AlO_x) was modified with different oxidized aluminum content which is responsible for the alteration of magnetic behaviors in our ultra-thin oxidized films. It was observed that the variation trend in surface roughness is also similar to the change in depinning and coercive fields. Hence, this study evidenced the strong influences of surfaces and interfaces on the magnetic and magneto-optical behaviors of the perpendicularly magnetized magnetic thin films.

Finally, the antisymmetric exchange interaction, i.e DMI, on various perpendicularly magnetized Pt/Co/AlOx trilayers was studied. The effects of post-annealing time, aluminum thickness and substrate nature were thoroughly investigated via electromagnetic, magneto-transport and magneto-optical characterization of our ultrathin films. The DMI study was performed based on three separate methods: asymmetric domain wall dynamics, current-induced hysteresis loop shift and Brillouin light spectroscopy. The DMI constant was raised from 0.1 mJ/m^2 to 1.13 mJ/m^2 when the annealing time duration for Pt (4 nm)/Co (1.2 nm)/AlO_x (2.5 nm) heterostructure increased from 1 hour to 4 hours. The enhancement of DMI in our experiment is attributed to the Co/AlO_x interface modification as evidenced by low-temperature anomalous Hall effect measurement and X-ray photoelectron spectroscopy measurement results. From the XPS experiment, the chemical states of thin film materials were investigated and hence CoO_x and CO contents at the interface were quantified. In addition, coercivity analysis via low-temperature magneto-transport measurement provided information about the exchange coupling of the antiferromagnetic CoO_x and ferromagnetic Co phases in different magnetic thin films which gave the implicit idea about the interfacial CoO_x. Both of these experiments agreed that the longer-time

annealed sample has a better interface due to the formation of homogeneous CoO_x content and is responsible for the enhancement of interfacial DMI.

To conclude, experimental work in this thesis develops a cost-effective VSM and explores the strong dependence of critical magnetic interactions on ferromagnet/metal oxide interface in heavy metal (HM)/ferromagnet (FM)/metal oxide (MO_x) heterostructure. More specifically, those results reflect the crucial influence of ferromagnetic layer oxidation at the Co/AlO_x interface of $Pt/Co/AlO_x$ trilayers. This work demonstrates that the devices with strongly improved DMI, depinning fields including other magnetic parameters can be achieved by the conscientious control of some external parameters such as post-annealing time, aluminum thickness and substrates. At the end, these experimental results uncovered the importance of the ferromagnet/metal oxide interface for the stabilization of chiral domain walls along with the field induced DW motion in presence of strong pinning centers in ultrathin magnetic heterostructures.

7.2 Outlook

The first part of our project involves the setting up of low-cost vibration sample magnetometry which can measure magnetization in only one direction. In addition to the unidirectional measurement, the advancement can be made on VSM suitable to measure magnetization in two dimensions which improves its effectiveness and precision as well. This requires additional effort in designing and building both hardware and software parts of the instruments that give rise to interesting future projects.

Home-built instruments may have increased utilizations because they are available at a fraction of the cost of a consumer-grade instrument. These instruments can be assembled using less expensive and easily available components which have the strong potential to revolutionize the industrial world. Companies, for example, may use cheaper design techniques and offer affordable options to those who have a limited budget. On the other hand, home-built instrument

involves the designation from the most basic level and they can be customized based on the customer's needs and interests which may not be possible in off-the-shelf instruments. These advantages of home-built instruments techniques make them accessible to a broad range of society as more people may be involved in research and experiments leading to important scientific exploration and discoveries. All these fruitful potential outcomes motivate the industrial communities to further study, design and develop these custom-made systems.

In Pt/Co/AlO_x heterostructure, DMI is enhanced for a longer post-annealing time. However, there are some open-ended questions coming into play. Does this scenario still hold true when replacing cobalt with another soft ferromagnetic alloy such as CoFeB? If it is the case, by introducing this alloy in between heavy metal and metal oxide, the exquisite skyrmion magnetic texture can be stabilized on those ultrathin films and their dynamics in reshuffle devices can be performed which are the crucial part of probabilistic computing architecture. Similarly, in our experiment, systematic interfacial modification is achieved due to the transformation of CoO_x from cobalt. Low-temperature coercivity was tuned due to the exchange interaction between them. Here, curiosity can be raised about whether there should be a match between ferromagnetic and antiferromagnetic material elements for such interaction and the enhancement of DMI. So, the DMI characterization with the interface modification by inserting another antiferromagnetic alloy such as Cr_2O_3, NiO and MnF_2 will be a major part of this project moving forward.

Similarly, our work uses the current induced Hall shift measurement approach to quantify the DMI. The same approach to that material system can be used for the quantification spin-orbit torque efficiency. The post-annealing effect on SOT efficiency on those materials has not been studied yet. Moreover, the measurement of second harmonic generation on those tunable magnetic anisotropic thin films is very important to characterize the strength of spin-orbit torque. Setting up those experiments along with the fabrication of material need many endeavors and a high level of dedication which leads to wonderful project to boost our work.

Our study about the influence of interfacial oxidation at the HM/MO_x interfaces on magnetic properties is useful to steer the current research toward more practical devices in consumer-level electronics. For example, understanding the Co/AlO_x interface in $Pt/Co/AlO_x$ heterostructures may help improve the storage capacity and performance of magnetic hard disc drives. Similarly, the comprehension of the dependence of interface modification on magnetic interactions within the $Pt/Co/AlO_x$ heterostructures will also be helpful to generate functional spin-based logic devices and memory which utilize electron's spin to encode and process information. The knowledge gained on oxidation effects on magnetization switching on those heterostructures will be obliged to create a feasible magnetic tunnel junction (MTJ), a basic component of MRAM technology, in semiconductor processing conditions. Hence, this experimental work would be a great asset to further current research to improve electronics devices and to create an efficacious memory system for the public welfare.

REFERENCES

[1] Lau D K 2018 Experimental Evaluation of the Interfacial Dzyaloshinskii-Moriya Interaction in Co/Ni Magnetic Multilayers *Doctoral dissertation* Carnegie Mellon University

[2] Julliere M 1975 Tunneling between ferromagnetic films *Phys. Lett. A* **54** 225-226

[3] Gr̈nberg P, Schreiber R, Pang Y, Brodsky M B and Sowers H 1986 Layered magnetic structures: Evidence for antiferromagnetic coupling of Fe layers across Cr interlayers *Phys. Rev. Lett.* **57** 2442-2445

[4] Binasch G, Grünberg P, Saurenbach F and Zinn W 1989 Enhanced magnetoresistance in layered magnetic structures with antiferromagnetic interlayer exchange *Phys. Rev. B* **39** 4828-4830

[5] Baibich M N, Broto J M, Fert A, Van Dau F N, Petroff F, Eitenne P, Creuzet G, Friederich A and Chazelas J 1988 Giant magnetoresistance of (001)Fe/(001)Cr magnetic superlattices *Phys. Rev. Lett.***61** 2472-2475

[6] Wolf S A, Awschalom D D, Buhrman R A, Daughton J M, Von Molnár S, Roukes M L, Chtchelkanova A Y and Treger D M 2001 Spintronics: A spin-based electronics vision for the future *Science* **294** 1488-1495

[7] Feng J 2019 Effects of oxidation on the spin-orbit torques and skyrmionic textures in ultrathin Pt/Co/AlOx heterostructures *Doctoral dissertation* ETH Zurich

[8] Žutić I, Fabian J and Sarma S Das 2004 Spintronics: Fundamentals and applications *Rev. Mod. Phys.* **76** 323-410

[9] Manchon A, Železný J, Miron I M, Jungwirth T, Sinova J, Thiaville A, Garello K and Gambardella P 2019 Current-induced spin-orbit torques in ferromagnetic and antiferromagnetic systems *Rev. Mod. Phys.***91** 035004

[10] Wang J, Meng H and Wang J P 2005 Programmable spintronics logic device based on a magnetic tunnel junction element *Journal of Applied Physics* **97** 10D509

[11] Cao A 2020 Interfacial effects of Pt / Co / X systems for advanced spintronic devices *Doctoral dissertation* Technische Universiteit Eindhoven

[12] Ikeda S, Miura K, Yamamoto H, Mizunuma K, Gan H D, Endo M, Kanai S, Hayakawa J, Matsukura F and Ohno H 2010 A perpendicular-anisotropy CoFeB-MgO magnetic tunnel junction *Nat. Mater.* **9** 721-724

[13] Parkin S S P, Hayashi M and Thomas L 2008 Magnetic domain-wall racetrack memory *Science* **320** 190-194

[14] Parkin S and Yang S H 2015 Memory on the racetrack *Nat. Nanotechnol.* **10** 195-198

[15] Rubio-Marcos F, Campo A Del, Marchet P and Fernández J F 2015 Ferroelectric domain wall motion induced by polarized light *Nat. Commun.* ***6*** 6594

[16] Schlickeiser F, Ritzmann U, Hinzke D and Nowak U 2014 Role of entropy in domain wall motion in thermal gradients *Phys. Rev. Lett.* ***113*** 097201

[17] Pai C F, Mann M, Tan A J and Beach G S D 2016 Determination of spin torque efficiencies in heterostructures with perpendicular magnetic anisotropy *Phys. Rev. B* **93** 1–7

[18] Schellekens A J, Van Den Brink A, Franken J H, Swagten H J M and Koopmans B 2012 Electric-field control of domain wall motion in perpendicularly magnetized materials *Nat. Commun.* **3** 847

[19] Tatara G and Kohno H 2004 Theory of Current-Driven Domain Wall Motion: Spin Transfer versus Momentum Transfer *Phys. Rev. Lett.***92** 086601

[20] Miron I M, Garello K, Gaudin G, Zermatten P J, Costache M V., Auffret S, Bandiera S, Rodmacq B, Schuhl A and Gambardella P 2011 Perpendicular switching of a single ferromagnetic layer induced by in-plane current injection *Nature* **476** 189-193

[21] Miron I M, Gaudin G, Auffret S, Rodmacq B, Schuhl A, Pizzini S, Vogel J and Gambardella P 2010 Current-driven spin torque induced by the Rashba effect in a ferromagnetic metal layer *Nat. Mater.* **9** 230–4

[22] Liu L, Pai C F, Li Y, Tseng H W, Ralph D C and Buhrman R A 2012 Spin-torque switching with the giant spin hall effect of tantalum *Science* **336** 555–8

[23] Kim J, Sinha J, Hayashi M, Yamanouchi M, Fukami S, Suzuki T, Mitani S and Ohno H 2013 Layer thickness dependence of the current-induced effective field vector in Ta|CoFeB|MgO *Nat. Mater.***12** 240-245

[24] OpenAI. (2023). Chat GPT [AI language model]. Retrieved March 1, 2023, from https://openai.com/ Type of help in the and motivation part: *Grammar*, *rearrange words of my sentences*

[25] Pellegren J P, Lau D and Sokalski V 2017 Dispersive Stiffness of Dzyaloshinskii Domain Walls *Phys. Rev. Lett.***119** 027203

[26] Stöhr J and Siegmann H C 2006 Magnetism *Solid-State Sciences* **5** 236

[27] Hanke J P, Freimuth F, Blügel S and Mokrousov Y 2018 Higher-dimensional wannier interpolation for the modern theory of the dzyaloshinskii–moriya interaction: Application to co-based trilayers *J. Phys. Soc. Japan* **87** 041010

[28] Keffer F 1962 Moria Interaction and Problem of Spin Arrangements in βMnS *Phys. review* **126** 896-900

[29] Hayashi M, Thomas L, Moriya R, Rettner C and Parkin S S P 2008 Current-controlled magnetic domain-wall nanowire shift register *Science* **320** 114599

[30] Soumyanarayanan A, Reyren N, Fert A and Panagopoulos C 2016 Emergent phenomena induced by spin-orbit coupling at surfaces and interfaces *Nature **539*** 509-517

[31] Kezsmarki I, Bordacs S, Milde P, Neuber E, Eng L M, White J S, Rønnow H M, Dewhurst C D, Mochizuki M, Yanai K, Nakamura H, Ehlers D, Tsurkan V and Loidl A 2015 Neel-type skyrmion lattice with confined orientation in the polar magnetic semiconductor GaV4S8 *Nat. Mater.* **14** 1116-1122

[32] Kim D H, Haruta M, Ko H W, Go G, Park H J, Nishimura T, Kim D Y, Okuno T, Hirata Y, Futakawa Y, Yoshikawa H, Ham W, Kim S, Kurata H, Tsukamoto A, Shiota Y, Moriyama T, Choe S B, Lee K J and Ono T 2019 Bulk Dzyaloshinskii–Moriya interaction in amorphous ferrimagnetic alloys *Nat. Mater.* **18** 685-690

[33] Boulle O, Vogel J, Yang H, Pizzini S, De Souza Chaves D, Locatelli A, Menteş T O, Sala A, Buda-Prejbeanu L D, Klein O, Belmeguenai M, Roussigné Y, Stashkevich A, Mourad Chérif S, Aballe L, Foerster M, Chshiev M, Auffret S, Miron I M and Gaudin G 2016 Room-temperature chiral magnetic skyrmions in ultrathin magnetic nanostructures *Nat. Nanotechnol.* **11** 449-454

[34] Legrand W, Maccariello D, Reyren N, Garcia K, Moutafis C, Moreau-Luchaire C, Collin

S, Bouzehouane K, Cros V and Fert A 2017 Room-Temperature Current-Induced Generation and Motion of sub-100 nm Skyrmions *Nano Lett.* **17** 2703-2712

[35] Emori S, Martinez E, Lee K J, Lee H W, Bauer U, Ahn S M, Agrawal P, Bono D C and Beach G S D 2014 Spin Hall torque magnetometry of Dzyaloshinskii domain walls *Phys. Rev. B - Condens. Matter Mater. Phys.* **90** 184427

[36] Yang H, Thiaville A, Rohart S, Fert A and Chshiev M 2015 Anatomy of Dzyaloshinskii-Moriya Interaction at Co/Pt Interfaces *Phys. Rev. Lett.* **115** 267210

[37] Baumgartner M, Garello K, Mendil J, Avci C O, Grimaldi E, Murer C, Feng J, Gabureac M, Stamm C, Acremann Y, Finizio S, Wintz S, Raabe J and Gambardella P 2017 Spatially and time-resolved magnetization dynamics driven by spin-orbit torques *Nat. Nanotechnol.* **12** 980-986

[38] Coey J M D 2010 Magnetism and magnetic materials *Cambridge University Press*

[39] Ryu K S, Yang S H, Thomas L and Parkin S S P 2014 Chiral spin torque arising from proximity-induced magnetization *Nat. Commun.***5** 3910

[40] Ryu K S, Thomas L, Yang S H and Parkin S 2013 Chiral spin torque at magnetic domain walls *Nat. Nanotechnol.* **8** 527–33

[41] Cao A, Zhang X, Koopmans B, Peng S, Zhang Y, Wang Z, Yan S, Yang H and Zhao W 2018 Tuning the Dzyaloshinskii-Moriya interaction in Pt/Co/MgO heterostructures through the MgO thickness *Nanoscale* **10** 12062–7

[42] Hayashi M, Thomas L, Rettner C, Moriya R and Parkin S S P 2008 Real time observation of the field driven periodic transformation of domain walls in Permalloy nanowires at the Larmor frequency and its first harmonic *Appl. Phys. Lett.* **10** 12510

[43] Blundell S and Thouless D 2003 Magnetism in Condensed Matter *Am. J. Phys.*94-95

[44] Chen G, Ma T, N'Diaye A T, Kwon H, Won C, Wu Y and Schmid A K 2013 Tailoring the chirality of magnetic domain walls by interface engineering *Nat. Commun.* **4** 2671

[45] Emori S, Bauer U, Ahn S M, Martinez E and Beach G S D 2013 Current-driven dynamics of chiral ferromagnetic domain walls *Nat. Mater.* **12** 611–6

[46] Avci C O, Rosenberg E, Baumgartner M, Beran L, Quindeau A, Gambardella P, Ross C A and Beach G S D 2017 Fast switching and signature of efficient domain wall motion driven by spin-orbit torques in a perpendicular anisotropy magnetic insulator/Pt bilayer *Appl. Phys. Lett.* **111** 072406

[47] Jiang W, Chen G, Liu K, Zang J, te Velthuis S G E and Hoffmann A 2017 Skyrmions in magnetic multilayers *Phys. Rep.* **704** 1-49

[48] Thiaville A, Rohart S, Jué É, Cros V and Fert A 2012 Dynamics of Dzyaloshinskii domain walls in ultrathin magnetic films *Epl* **100** 57002

[49] Rohart S and Thiaville A 2013 Skyrmion confinement in ultrathin film nanostructures in the presence of Dzyaloshinskii-Moriya interaction *Phys. Rev. B - Condens. Matter Mater. Phys.* **18** 184422

[50] Moriya T 1960 Anisotropic superexchange interaction and weak ferromagnetism *Phys. Rev.* **120** 91–8

[51] Benitez M J, Hrabec A, Mihai A P, Moore T A, Burnell G, McGrouther D, Marrows CH, McVitie S 2015 Magnetic microscopy and topological stability of homochiral Néel domain walls in a Pt/Co/AlO x trilayer *Nature Communications* **6** 8957

[52] Tarasenko S V., Stankiewicz A, Tarasenko V V. and Ferré J 1998 Bloch wall dynamics in

ultrathin ferromagnetic films *J. Magn. Magn. Mater.* **189** 19-24

[53] Schryer N L and Walker L R 1974 The motion of 180° domain walls in uniform dc magnetic fields *J. Appl. Phys.* **12** 5406-5421

[54] Baibich M N, Broto J M, Fert A, Nguyen F, Dau V, Petroff F, Eitenne P, Creuzet G, Friederich A and Chazelas J 1988 Giant Magnetoresistance of (001)Fel(001) Cr Magnetic Snperlattices *Phys. Rev. Lett.* **61** 2472

[55] Metaxas P J, Jamet J P, Mougin A, Cormier M, Ferré J, Baltz V, Rodmacq B, Dieny B and Stamps R L 2007 Creep and flow regimes of magnetic domain-wall motion in ultrathin Pt/Co/Pt films with perpendicular anisotropy *Phys. Rev. Lett.* **99** 1–4

[56] Kuepferling M, Casiraghi A, Soares G, Durin G, Garcia-Sanchez F, Chen L, Back C H, Marrows C H, Tacchi S and Carlotti G 2020 Measuring interfacial dzyaloshinskii-moriya interaction in ultra thin films *arXiv preprint arXiv* **2009** 11830

[57] Chauve P, Giamarchi T and Le Doussal P 2000 Creep and depinning in disordered media. *Physical Review B **62*** 6241

[58] Kabanov Y P, Iunin Y L, Nikitenko V I, Shapiro A J, Shull R D, Zhu L Y and Chien C L 2010 In-plane field effects on the dynamics of domain walls in ultrathin co films with perpendicular anisotropy *IEEE Trans. Magn.* **46** 2220–3

[59] Dzyaloshinsky I 1958 A Thermodynamic Theory of "Weak" Ferromagnetism of Antiferromagnetics *J. Phys. Chem. Solids Pergamon Press* **4** 241–55

[60] Hirsch J E 1999 Spin Hall Effect *Phys. Rev. Lett.* **83 1**834-1837

[61] Dyakonov M I and Perel V I 1971 Current-induced spin orientation of electrons in semiconductors *Phys. Lett. A* **35** 459-460

[62] Pai C F, Liu L, Li Y, Tseng H W, Ralph D C and Buhrman R A 2012 Spin transfer torque devices utilizing the giant spin Hall effect of tungsten *Appl. Phys. Lett.* **12** 122404

[63] Liu L, Lee O J, Gudmundsen T J, Ralph D C and Buhrman R A 2012 Current-induced switching of perpendicularly magnetized magnetic layers using spin torque from the spin hall effect *Phys. Rev. Lett.* **109** 096602

[64] Miron I M, Moore T, Szambolics H, Buda-Prejbeanu L D, Auffret S, Rodmacq B, Pizzini S, Vogel J, Bonfim M, Schuhl A and Gaudin G 2011 Fast current-induced domain-wall motion controlled by the Rashba effect *Nat. Mater.* **10** 419-423

[65] Hoffmann A 2013 Spin hall effects in metals *IEEE Trans. Magn.* **49** 5172-5193

[66] Getzlaff M 2008 *Fundamentals of magnetism* (New York, NY, USA: Springer)

[67] Foner S 1996 The vibrating sample magnetometer: Experiences of a volunteer (invited) *J. Appl. Phys.* **79** 4740

[68] Richter H J 1993 An analysis of magnetization processes in metal evaporated tape *IEEE Trans. Magn.* **29** 21–33

[69] Joven E, del Moral A and Arnaudas J I 1990 Magnetometer for anisotropy measurement using perpendicular magnetization *J. Magn. Magn. Mater.* **83** 548–50

[70] Matsubara N and Sai F 1991 Measurement of magnetization on an obliquely deposited film by using 3-dimensional vector VSM *IEEE Trans. Magn.* **27** 4748–50

[71] Richter H J and Hibst H 1991 Vectorial magnetization of metal evaporated tapes *J. Appl. Phys.* **70** 5512-5516

[72] Fagaly R L 2006 Superconducting quantum interference device instruments and applications *Rev. Sci. Instrum.* **77** 101101

[73] Legl S, Pfleiderer C, Krämer K, Legl S 2010 Vibrating coil magnetometer for milli-Kelvin temperatures **81** 043911

[74] Shah S A H 2013 Vibrating Sample Magnetometery : Analysis and Construction *Thesis* Syed Babar Ali School of Science and Engineering ,LUMS

[75] Callister D W, Rethwisch G D 2016 Magnetic characterization of ferromagnetic samples by Vibrating Sample *Material Science and Engineering Vibrating* 2-16

[76] John T, Pietschmann D, Becker V and Wagner C 2016 Deconvolution of time series in the laboratory *Am. J. Phys.* **84** 752-763

[77] Gopman D B, Bedau D, Kent A D 2012 A digitally configurable measurement platform using audio cards for high-resolution electronic transport studies *Rev. Sci. Instrum.* **83** 054701

[78] Sinlapanuntakul J, Kijamnajsuk P, Jetjamnong C and Chotikaprakhan S 2017 Digital lock-in amplifier based on soundcard interface for physics laboratory *Journal of Physics: Conference Series* **901** 012065

[79] Mathews J and Walker R L 1971 Mathematical Methods of Physics *New York, NY: Addison-Wesley*

[80] Mallinson J 1966 Magnetometer coils and reciprocity *J. Appl. Phys.* **37** 2514–5

[81] Bernards J 1993 Design of a detection coil system for a biaxial vibrating sample magnetometer and some applications *Rev. Sci. Instrum.* **64** 1918–30

[82] Foner S 1959 Versatile and sensitive vibrating-sample magnetometer *Rev. Sci. Instrum.* **30** 548-557

[83] Zieba A and Foner S 1982 Detection coil, sensitivity function, and sample geometry

effects for vibrating sample magnetometers *Rev. Sci. Instrum.* **53** 1344–54

[84] El-Alaily T M, Saafan S A, Kamel M M, Meaz T M and Assar S T 2015 Construction and calibration of a low cost and fully automated vibrating sample magnetometer *J. Magn. Magn. Mater.* **386** 25-30

[85] Hosseini N, Khiabani S, Sarreshtedari F and Fardmanesh M 2012 Optimized design and implementation of low-cost, sensitive and versatile vibrating sample magnetometer *ICEE 2012 - 20th Iran. Conf. Electr. Eng.* 202-205

[86] Burgei W, Pechan M J and Jaeger H 2003 A simple vibrating sample magnetometer for use in a materials physics course *Am. J. Phys.* **71** 825–8

[87] Gerber J A, Burmester W L, Sellmyer D J, Gerber J A, Burmester W L and Sellmyer D J 2013 Simple vibrating sample magnetometer Simple vibrating sample magnetometer *Rev. Sci. Instrum.* **691** 1–4

[88] Jordán D 2018 Detection of magnetic moment in thin films with a home-made vibrating sample magnetometer **456** 56-61

[89] Mauri D, Scholl D, Siegmann H C and Kay E 1989 Magnetism in very thin films of permalloy measured by spin polarized cascade electrons *Appl. Phys. A Solids Surfaces* **49** 439–47

[90] Lin K Q, Wang L Sen, Wang Z W, Wen R T, Chen Y and Peng D L 2013 Gas-phase synthesis and magnetism of HfO2nanoclusters *Eur. Phys. J. D* **67** 1-5

[91] Jiang W, Upadhyaya P, Zhang W, Yu G, Jungfleisch M B, Fradin F Y, Pearson J E, Tserkovnyak Y, Wang K L, Heinonen O, Te Velthuis S G E and Hoffmann A 2015 Blowing magnetic skyrmion bubbles *Science* **349** 283–6

[92] Emori S, Bauer U, Ahn S M, Martinez E and Beach G S D 2013 Current-driven dynamics of chiral ferromagnetic domain walls *Nat. Mater.* **12** 611–6

[93] Fert A, Reyren N and Cros V 2017 Advances in the Physics of Magnetic Skyrmions and Perspective for Technology *Nat. Mater.* **2** 17031

[94] Bautin V A, Seferyan A G, Nesmeyanov M S and Usov N A 2017 Magnetic properties of polycrystalline cobalt nanoparticles *AIP Adv.* **7** 045103

[95] Shan R, Gao T R, Zhou S M, Wu X S, Fang Y K and Han B S 2006 Co/Pt multilayers with large coercivity and small grains *J. Appl. Phys.* **99** 063907

[96] Zhang B, Krishnan K M, Lee C H and Farrow R F C 1993 Magnetic anisotropy and lattice strain in Co/Pt multilayers *J. Appl. Phys.* **73** 6198–200

[97] Park J H, Park C, Jeong T, Moneck M T, Nufer N T and Zhu J G 2008 CoPt multilayer based magnetic tunnel junctions using perpendicular magnetic anisotropy *J. Appl. Phys.* **103** 5–8

[98] Sankhi B R and Turgut E 2020 A low-cost vibrating sample magnetometry based on audio components *J. Magn. Magn. Mater.* **502** 166560

[99] Tudu B and Tiwari A 2017 Recent Developments in Perpendicular Magnetic Anisotropy Thin Films for Data Storage Applications *Vacuum* **146** 329–41

[100] Speetzen N, Stadler B J H, Yuan E, Victora R H, Qi X, Judy J H, Supper N and Pohkil T 2005 Co/Pd multilayers for perpendicular magnetic recording media *Journal of Magnetism and Magnetic Materials* **287** 181–7

[101] Honda N, Ariake J, Ouchi K, Iwasaki S I, Honda N, Ariake J, Ouchi K and Iwasaki S 1998 Low noise Co-Cr-Nb perpendicular recording media with high squareness *IEEE*

Trans. Magn. **34** 1651–3

[102] Iwasaki S ichi 2009 Perpendicular magnetic recording - Its development and realization *Proc. Japan Acad. Ser. B Phys. Biol. Sci.* **85** 37–54

[103] Yu G, Upadhyaya P, Shao Q, Wu H, Yin G, Li X, He C, Jiang W, Han X, Amiri P K and Wang K L 2017 Room-temperature skyrmion shift device for memory application *Nano Lett.* **17** 261−268

[104] Thomas L, Yang S H, Ryu K S, Hughes B, Rettner C, Wang D S, Tsai C H, Shen K H and Parkin S S P 2011 Racetrack memory: A high-performance, low-cost, non-volatile memory based on magnetic domain walls *Tech. Dig. - Int. Electron Devices Meet. IEDM* 535–8

[105] Huang Y, Li X, Wang L, Yu G, Wang K L and Zhao W 2018 Interface control of domain wall depinning field *AIP Adv.* **8** 056314

[106] Peng S, Wang M, Yang H, Zeng L, Nan J, Zhou J, Zhang Y, Hallal A, Chshiev M, Wang K L, Zhang Q and Zhao W 2015 Origin of interfacial perpendicular magnetic anisotropy in MgO/CoFe/metallic capping layer structures *Sci. Rep.* **5** 18173

[107] Johnson M T, Bloemen P J H, Den Broeder F J A and De Vries J J 1996 Magnetic anisotropy in metallic multilayers *Reports Prog. Phys.* **59** 1409

[108] Belmeguenai M, Adam J P, Roussigné Y, Eimer S, Devolder T, Kim J Von, Cherif S M, Stashkevich A and Thiaville A 2015 Interfacial Dzyaloshinskii-Moriya interaction in perpendicularly magnetized Pt/Co/AlOx ultrathin films measured by Brillouin light spectroscopy *Phys. Rev. B - Condens. Matter Mater. Phys.* **91** 1–4

[109] Ma X, Yu G, Razavi S A, Sasaki S S, Li X, Hao K, Tolbert S H, Wang K L and Li X

2017 Dzyaloshinskii-Moriya Interaction across an Antiferromagnet-Ferromagnet Interface *Phys. Rev. Lett.* **119** 027202

[110] Lu H M, Zheng W T and Jiang Q 2007 Saturation magnetization of ferromagnetic and ferrimagnetic nanocrystals at room temperature *J. Phys. D. Appl. Phys.* **40** 320–5

[111] Dimitrov D and Zhang S 1998 Effect of exchange interactions at antiferromagnetic/ferromagnetic interfaces on exchange bias and coercivity *Phys. Rev. B - Condens. Matter Mater. Phys.* **58** 12090

[112] Sabet S, Moradabadi A, Gorji S, Fawey M H, Hildebrandt E, Radulov I, Wang D, Zhang H, Kübel C and Alff L 2019 Correlation of Interface Structure with Magnetic Exchange in a Hard/Soft Magnetic Model Nanostructure *Phys. Rev. Appl.* **11** 054078

[113] Wang K, Wu M C, Lepadatu S, Claydon J S, Marrows C H and Bending S J 2011 Optimization of Co/Pt multilayers for applications of current-driven domain wall propagation *J. Appl. Phys.* **110** 083913

[114] Rodmacq B, Manchon A, Ducruet C, Auffret S and Dieny B 2009 Influence of thermal annealing on the perpendicular magnetic anisotropy of Pt/Co/AlOx trilayers *Phys. Rev. B - Condens. Matter Mater. Phys.* **79** 1–8

[115] Garad H, Fettar F, Gay F, Joly Y, Auffret S, Rodmacq B, Dieny B and Ortega L 2017 Temperature Variation of Magnetic Anisotropy in Pt /Co /AlOx Trilayers *Phys. Rev. Appl.* **7** 034023

[116] Moore T A, Miron I M, Gaudin G, Serret G, Auffret S, Rodmacq B, Schuhl A, Pizzini S, Vogel J and Bonfim M 2008 High domain wall velocities induced by current in ultrathin Pt/Co/AlOx wires with perpendicular magnetic anisotropy *Appl. Phys. Lett.* **93** 262504

[117] Jué E, Thiaville A, Pizzini S, Miltat J, Sampaio J, Buda-Prejbeanu L D, Rohart S, Vogel J, Bonfim M, Boulle O, Auffret S, Miron I M and Gaudin G 2016 Domain wall dynamics in ultrathin Pt/Co/AlOx microstrips under large combined magnetic fields *Phys. Rev. B* **93** 014403

[118] Ha Pham T, Vogel J, Sampaio J, Vaňatka M, Rojas-Sánchez J C, Bonfim M, Chaves D S, Choueikani F, Ohresser P, Otero E, Thiaville A and Pizzini S 2016 Very large domain wall velocities in Pt/Co/GdOx and Pt/Co/Gd trilayers with Dzyaloshinskii-Moriya interaction *Epl* **113** 67001

[119] Kim N H, Cho J, Jung J, Han D S, Yin Y, Kim J S, Swagten H J M, Lee K, Jung M H and You C Y 2017 Role of top and bottom interfaces of a Pt/Co/AlOx system in Dzyaloshinskii-Moriya interaction, interface perpendicular magnetic anisotropy, and magneto-optical Kerr effect *AIP Adv.* **7** 035213

[120] Li D, Ma R, Cui B, Yun J, Quan Z, Zuo Y, Xi L and Xu X 2020 Effect of the oxide layer on the interfacial Dyzaloshinskii-Moriya interaction in perpendicularly magnetized Pt/Co/SmOx and Pt/Co/AlOx heterostructures *Appl. Surf. Sci.* **513** 145768

[121] Sankhi B R, Echeverria E, Nembach HT, Shaw J M, Mandal S, Annaorazov M, Sachan R, Mcllroy, D N, Meyers D and Turgut E 2022 Engineering of Heterostructure Pt/Co/AlOx for the enhancement of Dyzaloshinskii-Moria interaction. *arXiv preprint arXiv:2205.15940*

[122] Kang M G, Choi J G, Jeong J, Park J Y, Park H J, Kim T, Lee T, Kim K J, Kim K W, Oh J H, Viet D D, Jeong J R, Yuk J M, Park J, Lee K J and Park B G 2021 Electric-field control of field-free spin-orbit torque switching via laterally modulated Rashba effect in Pt/Co/AlOx structures *Nat. Commun.* **12** 7111

[123] Schott M, Ranno L, Béa H, Baraduc C, Auffret S and Bernand-Mantel A 2021 Electric field control of interfacial Dzyaloshinskii-Moriya interaction in Pt/Co/AlOx thin films *J. Magn. Magn. Mater.**520** 167122*

[124] Yang M, Luo J, Ji Y, Zheng H-Z, Wang K, Deng Y, Wu Z, Cai K, Edmonds K W, Li Y, Sheng Y, Wang S and Cui Y 2019 Spin Logic Devices via Electric Field Controlled Magnetization Reversal by Spin-Orbit Torque *IEEE Electron Device Lett.* **40** 1554–7

[125] Moodera J S, Kinder L R, Wong T M and Meservey R 1995 Large magnetoresistance at room temperature in ferromagnetic thin film tunnel junctions *Phys. Rev. Lett.* **74** 3273–6

[126] Liu R S, Michalak L, Canali C M, Samuelson L and Pettersson H 2008 Tunneling anisotropic magnetoresistance in Co/AlOx/Au tunnel junctions *Nano Lett.* **8** 848–852

[127] Sun Y, Ba Y, Chen A, He W, Wang W, Zheng X, Zou L, Zhang Y, Yang Q, Yan L, Feng C, Zhang Q, Cai J, Wu W, Liu M, Gu L, Cheng Z, Nan C W, Qiu Z, Wu Y, Li J and Zhao Y 2017 Electric-Field Modulation of Interface Magnetic Anisotropy and Spin Reorientation Transition in (Co/Pt)3/PMN-PT Heterostructure *ACS Appl. Mater. Interfaces* **9** 10855–64

[128] Chen Y, Zhang Q, Jia J, Zheng Y, Wang Y, Fan X and Cao J 2018 Tuning Slonczewski-like torque and Dzyaloshinskii-Moriya interaction by inserting a Pt spacer layer in Ta/CoFeB/MgO structures *Appl. Phys. Lett.* **112** 232402

[129] Jeudy V, Mougin A, Bustingorry S, Savero Torres W, Gorchon J, Kolton A B, Lemaître A and Jamet J P 2016 Universal Pinning Energy Barrier for Driven Domain Walls in Thin Ferromagnetic Films *Phys. Rev. Lett.* **117** 057201

[130] Caballero N B, Fernández Aguirre I, Albornoz L J, Kolton A B, Rojas-Sánchez J C, Collin S, George J M, Diaz Pardo R, Jeudy V, Bustingorry S and Curiale J 2017 Excess

velocity of magnetic domain walls close to the depinning field *Phys. Rev. B* **96** 224422

[131] Diaz Pardo R, Savero Torres W, Kolton A B, Bustingorry S and Jeudy V 2017 Universal depinning transition of domain walls in ultrathin ferromagnets *Phys. Rev. B* **95** 184434

[132] Garad H, Ortega L, Ramos A Y, Joly Y, Fettar F, Auffret S, Rodmacq B, Diény B, Proux O and Erko A I 2013 Competition between CoOx and CoPt phases in Pt/Co/AlO x semi tunnel junctions *J. Appl. Phys.* **114** 053508

[133] Silva E F, Corrêa M A, Della Pace R D, Plá Cid C C, Kern P R, Carara M, Chesman C, Alves Santos O, Rodríguez-Suárez R L, Azevedo A, Rezende S M and Bohn F 2017 Thickness dependence of the magnetic anisotropy and dynamic magnetic response of ferromagnetic NiFe films *J. Phys. D. Appl. Phys.* **50** 1–13

[134] Jafri Y, Sharma G, Gupta A, Gupta M and Reddy V R 2021 Thickness dependent magnetic properties of ferromagnetic films (Fe, Co) interfaced with Ta *Thin Solid Films* **719** 138490

[135] Jiang Q, Yang H N and Wang G C 1997 Effect of interface roughness on hysteresis loops of ultrathin Co films from 2 to 30 ML on Cu(001) surfaces *Surf. Sci.* **373** 181–94

[136] Zhao Y P, Gamache R M, Wang G C, Lu T M, Palasantzas G and De Hosson J T M 2001 Effect of surface roughness on magnetic domain wall thickness, domain size, and coercivity *J. Appl. Phys.* **89** 1325–30

[137] Martinez E 2012 The stochastic nature of the domain wall motion along high perpendicular anisotropy strips with surface roughness *J. Phys. Condens. Matter* **24** 1–14

[138] Shaw J M, Nembach H T and Silva T J 2010 Roughness induced magnetic inhomogeneity in Co/Ni multilayers: Ferromagnetic resonance and switching properties in

nanostructures *J. Appl. Phys.* **108** 093922

[139] Lourembam J, Ghosh A, Zeng M, Wong S K, Yap Q J and Ter Lim S 2018 Thickness-Dependent Perpendicular Magnetic Anisotropy and Gilbert Damping in Hf/Co20Fe60 B20/Mg O Heterostructures *Phys. Rev. Appl.* **10** 044057

[140] Sankhi B R, Lamichhane U, Mandal S, Sachan R, Turgut E and Meyers D 2022 Interface Effects on Magnetic Anisotropy and Domain Wall Depinning Fields in Pt/Co/AlOx Films *Magnetochemistry* **8** 154

[141] Moriya T 1960 New mechanism of anisotropic superexchange interaction *Phys. Rev. Lett.* **4** 228–30

[142] Sampaio J, Cros V, Rohart S, Thiaville A and Fert A 2013 Nucleation, stability and current-induced motion of isolated magnetic skyrmions in nanostructures *Nat. Nanotechnol.* **8** 839–44

[143] Siracusano G, Tomasello R, Giordano A, Puliafito V, Azzerboni B, Ozatay O, Carpentieri M and Finocchio G 2016 Magnetic Radial Vortex Stabilization and Efficient Manipulation Driven by the Dzyaloshinskii-Moriya Interaction and Spin-Transfer Torque *Phys. Rev. Lett.* **117** 087204

[144] Bogdanov A N and Rößler U B 2016 Chiral symmetry breaking in magnetic thin films and multilayers *Phys. Rev. Lett.* **87** 37203-1-37203–4

[145] Iwasaki J, Mochizuki M and Nagaosa N 2013 Current-induced skyrmion dynamics in constricted geometries *Nat. Nanotechnol.* **8** 742–7

[146] Juge R, Je S G, Chaves D D S, Buda-Prejbeanu L D, Peña-Garcia J, Nath J, Miron I M, Rana K G, Aballe L, Foerster M, Genuzio F, Menteş T O, Locatelli A, Maccherozzi F,

Dhesi S S, Belmeguenai M, Roussigné Y, Auffret S, Pizzini S, Gaudin G, Vogel J and Boulle O 2019 Current-Driven Skyrmion Dynamics and Drive-Dependent Skyrmion Hall Effect in an Ultrathin Film *Phys. Rev. Appl.* **12** 1–9

[147] Fert A, Cros V and Sampaio J 2013 Skyrmions on the track *Nat. Nanotechnol.* **8** 152–6

[148] Wu Y, Meng K, Miao J, Xu X and Jiang Y 2019 Enhanced spin-orbit torque in Pt/Co/Pt multilayers with inserting Ru layers *J. Magn. Magn. Mater.* **472** 14–9

[149] Claudio-Gonzalez D, Thiaville A and Miltat J 2012 Domain wall dynamics under nonlocal spin-transfer torque *Phys. Rev. Lett.* **108** 227208

[150] Zhang S and Li Z 2004 Roles of nonequilibrium conduction electrons on the magnetization dynamics of ferromagnets *Phys. Rev. Lett.* **93** 127204

[151] Li D, Cui B, Yun J, Chen M, Guo X, Wu K, Zhang X, Wang Y, Mao J, Zuo Y, Wang J and Xi L 2018 Current-Induced Domain Wall Motion and Tilting in Perpendicularly Magnetized Racetracks *Nanoscale Res. Lett.* **13** 238

[152] Martinez J C, Lew W S, Gan W L and Jalil M B A 2018 Theory of current-induced skyrmion dynamics close to a boundary *J. Magn. Magn. Mater.* **465** 685–91

[153] Jiang W, Zhang X, Yu G, Zhang W, Wang X, Benjamin Jungfleisch M, Pearson J E, Cheng X, Heinonen O, Wang K L, Zhou Y, Hoffmann A and Te Velthuis S G E 2017 Direct observation of the skyrmion Hall effect *Nat. Phys.* **13** 162–9

[154] Romming N, Kubetzka A, Hanneken C, Von Bergmann K and Wiesendanger R 2015 Field-dependent size and shape of single magnetic Skyrmions *Phys. Rev. Lett.* **114** 177203

[155] Torrejon J, Kim J, Sinha J, Mitani S, Hayashi M, Yamanouchi M and Ohno H 2014 Interface control of the magnetic chirality in CoFeB/MgO heterostructures with heavy-

metal underlayers *Nat. Commun.* **5** 4–11

[156] Arora M, Shaw J M and Nembach H T 2020 Variation of sign and magnitude of the Dzyaloshinskii-Moriya interaction of a ferromagnet with an oxide interface *Phys. Rev. B* **101** 054421

[157] Nembach H T, Jué E, Evarts E R and Shaw J M 2020 Correlation between Dzyaloshinskii-Moriya interaction and orbital angular momentum at an oxide-ferromagnet interface *Phys. Rev. B* **101** 020409

[158] Gweon H K and Lim S H 2018 Relative strength of perpendicular magnetic anisotropy at bottom and top interfaces in Pt/Co/MgO trilayers *Jpn. J. Appl. Phys.* **57** 030301

[159] Manchon A, Pizzini S, Vogel J, Uhlíř V, Lombard L, Ducruet C, Auffret S, Rodmacq B, Dieny B, Hochstrasser M and Panaccione G 2008 X-ray analysis of oxygen-induced perpendicular magnetic anisotropy in Pt / Co / AlOx trilayers *J. Magn. Magn. Mater.* **320** 1889

[160] Hrabec A, Porter N A, Wells A, Benitez M J, Burnell G, McVitie S, McGrouther D, Moore T A and Marrows C H 2014 Measuring and tailoring the Dzyaloshinskii-Moriya interaction in perpendicularly magnetized thin films *Phys. Rev. B - Condens. Matter Mater. Phys.* **90** 1–5

[161] Cao A, Chen R, Wang X, Zhang X, Lu S, Yan S, Koopmans B and Zhao W 2020 Enhanced interfacial Dzyaloshinskii - Moriya interactions in annealed Pt/Co/MgO structures *Nanotechnology* **31** 155705

[162] Soucaille R, Belmeguenai M, Torrejon J, Kim J V., Devolder T, Roussigné Y, Chérif S M, Stashkevich A A, Hayashi M and Adam J P 2016 Probing the Dzyaloshinskii-Moriya interaction in CoFeB ultrathin films using domain wall creep and Brillouin light

spectroscopy *Phys. Rev. B* **94** 1–8

[163] Carcia P F 1988 Perpendicular magnetic anisotropy in Pd/Co and Pt/Co thin-film layered structures. *Journal of applied physics* ***63*** 5066-5073

[164] Yakushiji K, Kubota H, Fukushima A and Yuasa S 2016 Perpendicular magnetic tunnel junction with enhanced anisotropy obtained by utilizing an Ir/Co interface *Appl. Phys. Express* **9** 013003

[165] Shaw J M, Nembach H T and Silva T J 2013 Measurement of orbital asymmetry and strain in Co90Fe 10/Ni multilayers and alloys: Origins of perpendicular anisotropy *Phys. Rev. B - Condens. Matter Mater. Phys.* **87** 054416

[166] Shaw J M, Nembach H T, Silva T J and Boone C T 2013 Precise determination of the spectroscopic g-factor by use of broadband ferromagnetic resonance spectroscopy *J. Appl. Phys.* **114** 243906

[167] Je S G, Kim D H, Yoo S C, Min B C, Lee K J and Choe S B 2013 Asymmetric magnetic domain-wall motion by the Dzyaloshinskii-Moriya interaction *Phys. Rev. B - Condens. Matter Mater. Phys.* **88** 1–5

[168] Vaňatka M, Rojas-Sánchez J C, Vogel J, Bonfim M, Belmeguenai M, Roussigné Y, Stashkevich A, Thiaville A and Pizzini S 2015 Velocity asymmetry of Dzyaloshinskii domain walls in the creep and flow regimes *J. Phys. Condens. Matter* **27** 326002

[169] Thiaville A, Rohart S, Jué É, Cros V and Fert A 2012 Dynamics of Dzyaloshinskii domain walls in ultrathin magnetic films *Epl* **100** 57002

[170] Khadka D, Karayev S and Huang S X 2018 Dzyaloshinskii-Moriya interaction in Pt/Co/Ir and Pt/Co/Ru multilayer films *J. Appl. Phys.* **123** 123905

[171] Nembach H T, Shaw J M, Weiler M, Jué E and Silva T J 2015 Linear relation between Heisenberg exchange and interfacial Dzyaloshinskii-Moriya interaction in metal films *Nat. Phys.* **11** 825–9

[172] Shahbazi K, Kim J Von, Nembach H T, Shaw J M, Bischof A, Rossell M D, Jeudy V, Moore T A and Marrows C H 2019 Domain-wall motion and interfacial Dzyaloshinskii-Moriya interactions in Pt/Co/Ir(tIr)/Ta multilayers *Phys. Rev. B* **99** 094409

[173] Zeissler K, Mruczkiewicz M, Finizio S, Raabe J, Shepley P M, Sadovnikov A V., Nikitov S A, Fallon K, McFadzean S, McVitie S, Moore T A, Burnell G and Marrows C H 2017 Pinning and hysteresis in the field dependent diameter evolution of skyrmions in Pt/Co/Ir superlattice stacks *Sci. Rep.* **7** 15125

[174] Lo Conte R, Karnad G V., Martinez E, Lee K, Kim N H, Han D S, Kim J S, Prenzel S, Schulz T, You C Y, Swagten H J M and Kläui M 2017 Ferromagnetic layer thickness dependence of the Dzyaloshinskii-Moriya interaction and spin-orbit torques in Pt\Co\AlOx *AIP Adv.* **7** 065317

[175] Ong P V., Kioussis N, Amiri P K, Wang K L and Carman G P 2015 Strain control magnetocrystalline anisotropy of Ta/FeCo/MgO heterostructures *J. Appl. Phys.* **117** 17B518-1

[176] Lavrijsen R, Hartmann D M F, Van Den Brink A, Yin Y, Barcones B, Duine R A, Verheijen M A, Swagten H J M and Koopmans B 2015 Asymmetric magnetic bubble expansion under in-plane field in Pt/Co/Pt: Effect of interface engineering *Phys. Rev. B - Condens. Matter Mater. Phys.* **91** 104414

[177] Cao A, Chen R, Wang X, Zhang X, Lu S, Yan S, Koopmans B and Zhao W 2020 Enhanced interfacial Dzyaloshinskii - Moriya interactions in annealed Pt/Co/MgO

structures *Nanotechnology* **31** 155705

[178] Belabbes A, Bihlmayer G, Blügel S and Manchon A 2016 Oxygen-enabled control of Dzyaloshinskii-Moriya Interaction in ultra-thin magnetic films *Sci. Rep.* **6** 24634

[179] Pan C J, Gao T H, Itogawa N, Harumoto T, Zhang Z J, Nakamura Y and Shi J 2019 Large lattice mismatch induced perpendicular magnetic anisotropy and perpendicular exchange bias in CoPt/FeMn bilayer films *Sci. China Technol. Sci.* **62** 2009–13

[180] Deger C 2020 Strain-enhanced Dzyaloshinskii–Moriya interaction at Co/Pt interfaces *Sci. Rep.* **10** 12314

[181] Gusev N S, Sadovnikov A V., Nikitov S A, Sapozhnikov M V. and Udalov O G 2020 Manipulation of the Dzyaloshinskii-Moriya Interaction in Co/Pt Multilayers with Strain *Phys. Rev. Lett.* **124** 157202

[182] Biesinger M C, Payne B P, Grosvenor A P, Lau L W M, Gerson A R and Smart R S C 2011 Resolving surface chemical states in XPS analysis of first row transition metals, oxides and hydroxides: Cr, Mn, Fe, Co and Ni *Appl. Surf. Sci.* **257** 2717

[183] Sankhi B R, Echeverria E M, Mandal S and Annaorazov M Engineering Pt / Co / AlO x heterostructures to enhance the Dzyaloshinskii – Moriya interaction **35** 145802

VITA

BABU RAM SANKHI

Candidate for the Degree of

Doctor of Philosophy

Thesis: INTERFACIAL EFFECTS ON THE CHIRAL DOMAIN WALLS IN ULTRATHIN Pt/CO/AlO_X HETEROSTRUCTURES FOR THE FUTURISTIC SPINTRONICS DEVICES

Major Field: Physics

Biographical:

Education:

Completed the requirements for the Doctor of Philosophy in Physics at Oklahoma State University, Stillwater, Oklahoma in May 2023.

Completed the requirements for the Master of Science in Physics at Oklahoma State University Stillwater, OK in 2022.

Completed the requirements for the Master of Science in Physics at Tribhuvan University, Kathmandu, Nepal in 2011.

Completed the requirements for the Bachelor of Science in Physics at Tribhuvan University, Kathmandu, Nepal in 2007.

Experience: Graduate Teaching and Research Assistant: Oklahoma State University, 2018-2023
Graduate Teaching Assistant, The University of Tulsa, Aug 2017- May 2018

Professional Memberships: American Physical Society (APS), Institute of Electrical and Electronics Engineers (IEEE), IEEE Magnetics Society